AN ABSTRACT OF THE THESIS OF

Satoshi Kimura for the degree of Doctor of Philosophy in Oceanography presented on May 26, 2010.

Title: Turbulence in Sheared, Salt-fingering Favorable Environment

Abstract approved: _____

William D. Smyth

Instability and turbulence in sheared, salt-fingering favorable stratification are studied using three-dimensional direct numerical simulations (DNS). Salt-fingering favorable stratification is gravitationally stable, because the unstable vertical gradient of salinity is stabilized by temperature (warm, salty over cool, fresh water-masses). Salt-fingering instability can occur at the interface of these different water-masses. Salt-fingering instability generates cells of rising and sinking fluid because of the difference in diffusivity of heat and salt. In the presence of a vertically varying horizontal current (shear), salt-fingering instability is supplanted by salt-sheet instability. Salt-sheet instability generates alternating planar regions of rising and sinking fluid, aligned parallel to the direction of the sheared current.

As the salt sheet reaches the finite amplitude, secondary instability appears at the edges of salt sheets and introduces quasi-periodic dependence along the direction of the sheared current. The secondary instability disrupts the growth of salt sheets and brings the flow into the turbulent regime. Secondary instability can be treated approximately as linear normal mode of the finite-amplitude salt sheets. The secondary instability is shown to be an oscillatory instability, driven primarily by buoyancy.

In the turbulent regime, it is shown that thermal and saline buoyancy gradients

become more isotropic than the velocity gradients in the dissipation-range scale. In the velocity field, the geometry of the primary instability is embedded in the dissipation-range scale geometry even in the turbulent regime; therefore, the flow geometry from primary instability biases the estimation of the turbulent kinetic energy dissipation rate. Estimation of the turbulent kinetic energy dissipation rate by assuming isotropy, a common method in the interpretations of observations, can underestimate its true value by a factor of 2 to 3.

Of primary interest of the oceanographic community is the turbulent transport of momentum, heat, and salt associated with salt-sheet instability, which can modify water-masses and lower the potential energy of the ocean. The effective diffusivites of momentum, heat, and salt are used to describe the turbulent state. The effective diffusivity of momentum is an order of magnitude smaller than that of salt; turbulence associated with salt-sheet instability is therefore relatively inefficient in transferring momentum. These effective diffusivities are compared to observational estimates.

Turbulence in Sheared, Salt-fingering Favorable Environment

by

Satoshi Kimura

A THESIS

submitted to

Oregon State University

in partial fulfillment of
the requirements for the
degree of

Doctor of Philosophy

Presented May 26, 2010
Commencement June 2010

Doctor of Philosophy thesis of Satoshi Kimura presented on May 26, 2010

APPROVED:

Major Professor, representing Oceanography

Dean of the College of Oceanic and Atmospheric Sciences

Dean of the Graduate School

I understand that my thesis will become part of the permanent collection of Oregon State University libraries. My signature below authorizes release of my thesis to any reader upon request.

Satoshi Kimura, Author

ACKNOWLEDGEMENTS

I would like to thank my advisor Bill Smyth for introducing me to a magic of linear stability analysis. Bill has guided me to acquire useful tool and challenged me to develop and communicate my ideas. Most importantly, Bill has taught me to be careful and precise with my research. Special thanks also goes to my committee members Jim Moum, Eric Skyllingstad, Ricardo Matano, and Bill Bogley. I appreciate all the energy and time, which they invested to the completion of my thesis.

I would like to thank my officemates and classmates for their supports. Graduate school just wouldn't have been the same without Levi Kilcher, Sam Kelly, Jeffrey Early, and Emily Shroyer. I would also like to thank to my girl friend, Dafne Eerkes-Medrano, and LaHacienda residents, Levi Kilcher, Logan Mitchell, and Cate Dolan, for providing me a comfortable living environment. Finally, the completion of this thesis would have never been possible without supports from my parents, Ken Kimura and Midori Kimura, and my brother, Masashi Kimura.

TABLE OF CONTENTS

TABLE OF CONTENTS (Continued)

LIST OF FIGURES

LIST OF FIGURES (Continued)

LIST OF TABLES

TURBULENCE IN SHEARED, SALT-FINGERING FAVORABLE ENVIRONMENT

1. INTRODUCTION

Stratification in the ocean is determined by two components, temperature and salinity. Gravitationally stable stratification (light over dense) can be maintained even though one of the components is unstably distributed. In the case of unstably distributed salt, salt fingering instability can grow. The faster diffusion of heat relative to salt disrupts the gravitationally stable stratification by creating buoyancy anomalies. The cool, fresh anomalies get warmer while retaining their salinity, and therefore become lighter than the surrounding fluid (and vice versa for the warm, salty anomalies). These buoyancy anomalies generate vertical motions, the well known salt-fingering instability. One effect of these motions is an up-gradient transport of mass by vertically mixing heat and salt in dramatic contrast to the effect of mechanically-driven mixing. The importance of salt-fingering instability in the ocean was first raised in the defining paper, when Stern (1960) wrote "*future studies of this model relative to the amplitude of the motion and the subsequent transition to turbulence ... will determine whether the proposed mechanism is significant in the vertical mixing of the sea.*"

In much of subtropical gyre, evaporation at the sea surface exceeds precipitation, setting up the finger-favorable salinity and temperature gradient (Schmitt, 1994b, 2003). Salt-fingering favorable stratification is frequently found in thermohaline staircases (Lambert and Sturges, 1977; Schmitt, 1994a; Tait and Howe, 1968). Thermohaline staircases are stacked sequences of layers of different water-masses, separated by transition layers.

Transition layers are usually a few meters thick with sharp gradients of temperature and salinity. Thermohaline staircases can be either maintained by a horizontal pressure gradient generated by intrusions (Merryfield, 1999) or an up gradient transport of mass by salt-fingering (Radko, 2003; Schmitt, 2003).

The occurrences of salt-fingering in the ocean are confirmed by shadowgraph images in a transition layer of a thermohaline staircase in Mediterranean outflow (Williams, 1974). Seawater's index of refraction is a function of both temperature and salinity. The index of refraction of the warm, salty water is higher than the cool, fresh water, allowing salt-fingering to be photographed. Williams (1974) showed vertically aligned bands of organized salt fingers. In contrast, shadowgraph images taken in the thermohaline staircase east of Barbados showed tilted laminae (Kunze et al., 1987). Kunze et al. (1987) argued that tilted laminae was either (1) fingers tilted by shear or (2) instabilities on shear-aligned sheets.

Salt-fingering can also occur in the absence of thermohaline staircase (St. Laurent and Schmitt, 1999). Shadowgraph images of the North Atlantic Tracer Release Experiment (NATRE), performed in an area moderately favorable to salt fingers, showed tilted laminae similar to Kunze et al. (1987) (St. Laurent and Schmitt, 1999). The absence of thermohaline staricases in NATRE site is likely due to the presence of sufficiently strong turbulence, disrupting the formation of permanent staircases (St. Laurent and Schmitt, 1999); therefore, it is anticipated that salt-fingering instability is subjected to a vertically varying horizontal current.

Turbulent transport of heat and salt by salt-fingering instability can influence large-scale circulations. Gargett and Holloway (1992) showed that thermocline circulation was sensitive to the ratio of saline (K_S) to thermal (K_T) effective diffusivities in an idealized ocean circulation model of a Northern Hemisphere basin, forced by zonal mean climatology. Their K_S and K_T were different but spatially uniform. With a usual choice of $K_S/K_T = 1$,

a conventional meridional cell, driven by high-lattitude sinking, spreading equatorward, and upwelling at intermediate levels, occupied most of the basin. When $K_S/K_T = 0.5$, the magnitude of cells increased by 50%. However, when $K_S/K_T = 2$, the magnitude of cells have weakened by 25%, and the abyssal circulation was reversed in direction.

Zhang et al. (1999) parameterized the mixing by salt-fingering more realistically; they assigned K_S and K_T based on the local intensity of salt-fingering instability. Meridional circulation was 22% smaller than the case of spatially uniform K_S and K_T. Merryfield et al. (1999) employed a similar parameterization to Zhang et al. (1999) to more realistic geometry and forcing. Merryfield et al. (1999) found that the regional circulation is significantly influenced by salt-fingering; however, a large scale circulation is slightly modified.

Direct numerical simulations can improve our understanding of salt-fingering in the non-linear regime. Piacsek and Toomre (1980) was the first to describe the evolution of two-dimensional salt fingers. Following Piacsek and Toomre (1980), evolution of two-dimensional salt fingers in unbounded domain have been investigated by many authors (e.g. Merryfield and Grinder, 2000; Shen, 1989, 1995; Stern et al., 2001; Yoshida and Nagashima, 2003). Merryfield and Grinder (2000) found that their thermal and saline effective diffusivities agreed well with observations from NATRE site (St. Laurent and Schmitt, 1999), but larger than those from C-SALT site (Fleury and Lueck, 1991). This supported the speculation that the salt-fingering in C-SALT site is weak, perhaps due to high levels of vertically varying horizontal current (Kunze, 1994).

In the presence of vertically varying horizontal current, salt-fingering instability is supplanted by salt-sheet instability. Salt-sheet instability takes a shape of alternating planar regions of rising and sinking fluid, aligned parallel to the background current (Linden, 1974) in dramatic contrast to salt-fingering instability, which can take various planforms, such as sheets, squares, and rectangles (Proctor and Holyer, 1986; Schmitt, 1994b; Stern

et al., 2001). Linden's (1974) linear stability analysis showed that salt sheet was the fastest growing normal mode in the presence of the background current, and he confirmed this result by laboratory experiments. While theories for the initial growth of salt-fingering and salt-sheet instabilities are well established (Kunze, 2003; Linden, 1974; Smyth and Kimura, 2007; Stern, 1960), the non-linear regime of three-dimensional salt-sheet and salt-fingering instabilities in bounded domain are not well understood. This thesis addresses the physics that leads salt sheets to turbulence and the resulting turbulence, using three-dimensional (3D) direct numerical simulation (DNS) in bounded domain.

Chapter 2 describes the transition to turbulence in a single transitional layer, separating homogeneous layers above and below, in the presence of a sheared horizontal current. The single transitional layer is modeled as a double-diffusive shear layer of hyperbolic tangent form. Resolving the spatial scales associated with the slowly diffusing scalar, salinity, is a computational grand challenge. This computation employs the realistic value of saline diffusivity in 3D DNS for the first time. As salt sheet instability reaches finite amplitude, secondary instability arrests the growth of salt sheets. The text of Chapter 2 is a reprint with minor modifications of "Direct numerical simulation of salt sheets and turbulence in a double-diffusive shear layer", *Geophys. Res. Lett.*, **34**, L21610 (2007). The dissertation author was a lead author on this manuscript. W.D. Smyth directed and supervised the research.

In Chapter 3, nonseperable, linear, normal mode analysis is used to identify the physics of secondary instability. The secondary instability of salt-fingering was first proposed by Stern as collective instability (Stern, 1969). The collective instability is an oscillatory instability, which is an amplification of internal waves on scales much larger than the fingers. In a later study, Holyer (1984) found a small (finger-scale) non-oscillatory secondary instability that grows faster than the collective instability. Both instabilities contribute to disrupt the growth of salt-fingering. These studies have neglected the effect

of sheared horizontal currents and assumed a vertically unbounded fluid domain with uniform stratification. Here, we employ DNS and secondary stability analysis to study the secondary instability in the presence of vertically varying horizontal current on a localized fingering layer. The text of Chapter 3 is a minor modification of "Secondary instability of salt sheets", submitted to *Journal of Marine Research*. The dissertation author was a lead author on this manuscript. W.D. Smyth directed and supervised the research.

Chapter 4 extends Chapter 1 to a range of initial states. Anisotropy and its effect on estimating turbulence statistics are discussed. Kolmogorov (1941) proposed the idea that small-scale statistics in fully developed turbulence are universal. According to this hypothesis, the dissipation-range geometry becomes independent of direction, i.e., the geometry of the energy-containing scale is unimportant in the dissipation-range scale. This hypothesis, combined with observations by a horizontal and vertical profiler (Lueck, 1987), has been used to justify the estimation of dissipation rates in salt-fingering favorable ocean using approximation based on isotropy. These dissipation rates, combined with the Osborn and Cox (1972) diffusivity model, can be used to estimate the effective diffusivities of heat, salt, and momentum.

Here, we test the isotropy assumption of sheared, double-diffusive turbulence and compare effective diffusivities from the Osborn and Cox (1972) diffusivity model to direct calculations of effective diffusivities. The text of Chapter 4 will be submitted to *Journal of Physical Oceanography*. The dissertation author was a lead author on this manuscript. W.D. Smyth directed and supervised the research, and E. Kunze is the third author. The conclusions are summarized in Chapter 5.

2. DIRECT NUMERICAL SIMULATION OF SALT SHEETS AND TURBULENCE IN A DOUBLE-DIFFUSIVE SHEAR LAYER

2.1. Abstract

We describe three-dimensional direct numerical simulations (DNS) of double-diffusively stratified flow interacting with inflectional shear. The extreme difference in diffusivity (and thus minimum length scale) between heat, salt and momentum in seawater is replicated for the first time in a three-dimensional simulation. The primary instability generates salt sheets, which are oriented parallel to the direction of the sheared background flow. Subsequently, two distinct mechanisms of secondary instability combine to lead the flow to a turbulent state. In this state, the effective saline diffusivity is smaller than that calculated by previous investigators for the unsheared case. The Schmidt number is much smaller than unity, indicating that salt sheets are less effective at transporting momentum than is often assumed.

2.2. Introduction

Stratification in the ocean is determined by two components, temperature and salinity. Gravitationally stable stratification (i.e. light over heavy) can be maintained even though one of the components is unstably distributed. If salt is unstably distributed, salt fingers may grow (e.g. Kunze, 2003). In a large portion of the subtropical ocean, evaporation exceeds precipitation at the same time heating exceeds cooling. Consequently, warm salty water is produced on the surface that stays above cooler, fresher water (Schmitt, 2003).

In a quiescent environment, double-diffusive instability creates a rich variety of salt finger planforms (Schmitt, 1994b). In the presence of a sheared, horizontal ambient

current, the preferred mode takes the form of vertical sheets aligned parallel to the flow (Linden, 1974). These structures are now called salt sheets. In the ocean, salt fingering instability may organize the water column into a thermohaline staircase (Radko, 2003; Schmitt, 2003). In this case, ubiquitous background shear tends to be focused at depths where double-diffusive instability is strong (Gregg and Sanford, 1987). It is therefore anticipated that the resulting instability will have the form of salt sheets.

Here, we use three-dimensional (3D) direct numerical simulation (DNS) to investigate the transition to turbulence in a bounded fluid with non-uniform vertical gradients of salinity, temperature and horizontal current. Resolving the spatial scales associated with the slowly diffusing scalar, salinity, is a computational grand challenge. Our computation employs the realistic value of saline diffusivity in 3D DNS for the first time.

Section 2 discusses the DNS model and initial conditions. Section 3 discusses the sequence of instabilities that leads to turbulence. The turbulent state is described in section 4, and conclusions are summarized in section 5.

2.3. Methodology

We assume that the total buoyancy b is the sum of thermal and saline buoyancy components (b_T and b_S, resp.), each of which is governed by an advection-diffusion equation:

$$b = b_T + b_S; \quad \frac{Db_T}{Dt} = \kappa_T \nabla^2 b_T; \quad \frac{Db_S}{Dt} = \kappa_S \nabla^2 b_S. \tag{2.1}$$

$D/Dt = \partial/\partial t + \vec{u} \cdot \vec{\nabla}$ is the material derivative. The velocity field $\vec{u}(x, y, z, t) = \{u, v, w\}$ is measured in a nonrotating, Cartesian coordinate system $\{u, v, w\}$. We neglect inertial effects of density variations in accordance with the incompressible Boussinesq approximation:

$$\frac{D\vec{u}}{Dt} = -\nabla\pi + b\hat{k} + \nu\nabla^2\vec{u}; \quad \nabla \cdot \vec{u} = 0. \tag{2.2}$$

The variable π represents the pressure scaled by the characteristic density ρ_0, and $\hat{k}$ is the vertical unit vector. The total buoyancy is defined as $b = -g(\rho - \rho_0)/\rho_0$, where g is the acceleration due to gravity. Kinematic viscosity and thermal and saline diffusivities are denoted by ν, κ_T and κ_S, respectively.

Boundary conditions are periodic in the horizontal, with periodicity intervals L_x and L_y in the streamwise (x) and spanwise (y) directions, respectively. Upper and lower boundaries, located at $z = 0$ and $z = L_z$, are impermeable ($w = 0$), stress-free ($\partial u/\partial z = \partial v/\partial z = 0$) and insulating with respect to both heat and salt ($\partial b_T/\partial z = \partial b_S/\partial z = 0$).

For the experiments reported here, initial profiles were chosen to represent a stratified shear layer:

$$\frac{u}{\Delta u} = \frac{b_T}{\Delta B_T} = \frac{b_S}{\Delta B_S} = \tanh\left(\frac{z - \frac{Lz}{2}}{h}\right) \tag{2.3}$$

Here, Δu is the half-change of background velocity across a transition layer of half-depth h. ΔB_T and ΔB_S are the half-changes in thermal and saline buoyancy, respectively. The half-change in total buoyancy is then $\Delta B = \Delta B_T + \Delta B_S$.

The primary instability was seeded by adding an initial disturbance proportional to the fastest growing mode of linear theory (Smyth and Kimura, 2007), with amplitude chosen so that the maximum vertical parcel displacement was $0.02h_0$. To seed secondary instabilities the initial perturbation was supplemented with a random velocity field with maximum amplitude $0.01\Delta u$.

Relevant parameter values for the three cases discussed here are given in table 1 along with observed values. The differences in molecular diffusivity between heat, salt and momentum are described by the Prandtl number $Pr = \nu/\kappa_T$ and the diffusivity ratio $\tau = \kappa_S/\kappa_T$. In salt water, these ratios are far from unity, a circumstance that poses extreme challenges for numerical simulation as it leads to a wide range of spatial scales that must be resolved. The Prandtl number was set to 7, a typical value for water at oceanic temperatures. Given that the smallest scale of a scalar field is roughly proportional to the

square root of its diffusivity, temperature is expected to vary on scales smaller than those of velocity by a factor $\sqrt{7} = 2.6$. The diffusivity ratio τ for salt water is about 0.01, so that salinity fluctuates on scales as small as a factor of ten below the smallest temperature scale. In previous DNS of salt water, this extreme difference in scales has required that τ be artificially increased (e.g. Gargett et al., 2003; Smyth et al., 2005; Stern et al., 2001). Thanks to advances in computer power, it is now possible to use the realistic value. Here we compare three simulations using $\tau = 0.01$ and higher values.

The density ratio $R_\rho = -\Delta B_T / \Delta B_S$ was set to 1.6. The bulk (minimum) Richardson number $Ri = \Delta B h / \Delta u^2$ was given the value 2. These choices ensure that double diffusive modes grow and are not overwhelmed by inflectional shear instabilities (Smyth and Kimura, 2007).

A Reynolds number relevant for the initial growth of salt sheets in a sheared environment is constructed using the wavelength λ_{fg} of the fastest-growing salt sheet mode and the maximum background shear $S = \Delta u / h$: $Re_\lambda = \lambda_{fg}^2 S / \nu$. The wavelength is the same as that for salt fingers: $\lambda_{fg} = 2\pi(\nu\kappa_T h / \Delta B)^{1/4}$ (e.g. Smyth and Kimura, 2007). Our value is the same as the observed value: λ_{fg}=0.046m. This gives $Re_\lambda = 11$, which is at the high end of the observed range (table 1).

The spanwise periodicity interval L_y was chosen so as to accommodate two wavelengths of the fastest-growing primary instability. The appropriate value for L_x is not well known a priori, as it is determined by the streamwise wavelengths of the secondary instabilities whose presence is reported here for the first time. For the $\tau = 0.01$ and $\tau = 0.04$ cases, we set L_x to 8m, which in retrospect is probably larger than necessary. For the $\tau = 0.16$ cases, we used the smaller value L_x=1m. Further research is needed to constrain this length scale more precisely.

The numerical code used to solve (2.1) - (2.2) is described in Winters et al. (2004) with modifications as discussed by Smyth et al. (2005). The slowly diffusing scalar, salinity,

	DNS1	DNS2	DNS3	Ocean
Pr	7	7	7	7
τ	0.01	0.04	0.16	0.01
R_ρ	1.6	1.6	1.6	1.70 $\pm$ 0.15
Ri	2	2	2	3 $\pm$ 2
λ_{fg}[m]	0.046	0.046	0.046	0.046$\pm$ 0.006
Re_λ	11	11	11	8 $\pm$ 3
L_x[m]	8	8	1	
L_y[m]	0.09	0.09	0.09	
L_z[m]	1.9	1.9	1.9	
N_x	6144	3072	384	
N_y	144	144	40	
N_z	3072	1536	768	

TABLE 2.1: Typical values of non-dimensional parameters in the ocean and in our DNS runs. Diffusivities are standard values for salt water at 20 ^{o}C. Observed values of R_ρ, Ri, λ_{fg} and Re_λ are taken from Gregg and Sanford (1987) as summarized in their figure 3. Nine sheared, double-diffusive interfaces were observed. The range quoted is the mean plus or minus one standard deviation.

is resolved on a fine grid with spacing equal to one half the spacing used to resolve the other fields. A fit to the results of Stern et al. (2001) for 2D salt fingers suggests a fine grid spacing $\Delta = 0.15\lambda_{fg}\tau^{1/2}$ in the y and z directions. We have found that this choice gives adequate resolution of the salinity field. Because gradients are much gentler in the x direction, the corresponding grid increment is doubled. The remaining fields are computed on the coarse grid, but even so are extremely well-resolved.

2.4. The transition to turbulence

Figure 2.1 shows the salinity field at selected times during DNS1. Figure 2.1a shows the primary "salt sheet" instability. Rising sheets of cool, fresh water (shown in red and yellow) alternate with sinking sheets of warm, salty water (blue and purple). The computational domain accommodates two wavelengths of the instability.

When the salt sheets reach sufficiently large amplitude (figure 2.1b), they exhibit two distinct secondary instabilities, which we will refer to as the "sheet" and "tip" instabilities. The sheet instability appears as a vertically-quasiperiodic buckling motion whose amplitude is largest at the center of the transition layer. The vertical wavelength is $\approx 1.8\lambda_{fg}$, consistent with that computed by Stern and Simeonov (2005) for unsheared two-dimensional salt fingers. Buckling regions show a slight tilt in the x-direction. The tip instability is focused at the tips of the salt sheets and shows rapid, quasiperiodic fluctuations in the x direction. Both instabilities are strongly modified as they reach large amplitude (figure 2.1c). The sheet instability breaks down into turbulent motions that show the influences of both double-diffusive convection and the mean shear. The tip instability launches convective plumes into the upper and lower homogenous regions, where the influence of the mean shear is much weaker. The result is a complex, chaotic flow that we refer to as "double-diffusive turbulence". A statistical description of double diffusive

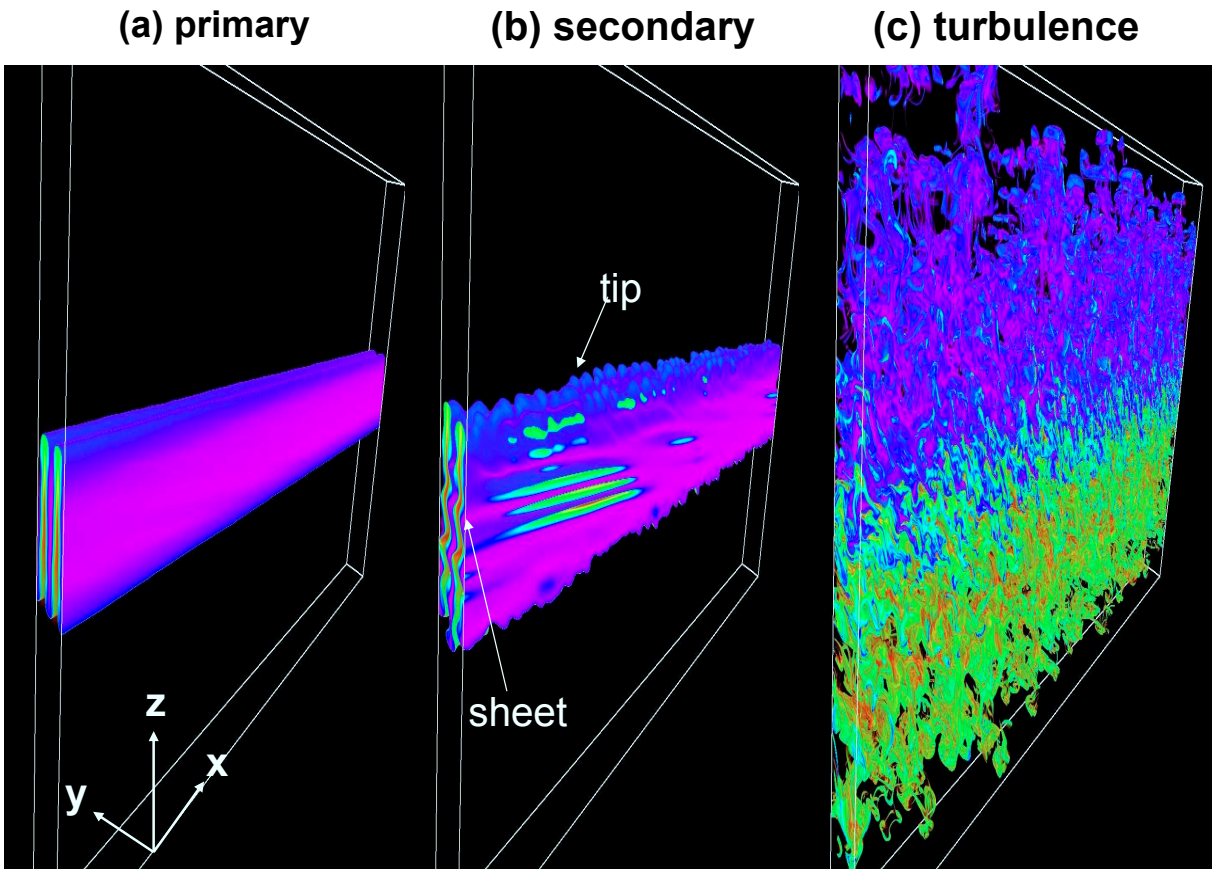

FIGURE 2.1: Evolution of the salinity field for DNS1. (a) $t = 2944s.$; (b) $t = 3362s.$; (c) $t = 5109s.$; Homogeneous regions above and below the transition layer are rendered transparent. Within the transition layer, the highest salinities are shown in purple and blue; the lowest in red and yellow. Only half of the streamwise (x) domain extent is shown. Labels on (b) indicate two distinct mechanisms of secondary instability as discussed in the text.

turbulence is given in section 4.

An alternative view of the transition process is gained via the instantaneous exponential growth rate for the velocity perturbation $\vec{u}'(x,y,z,t) = \vec{u}(x,y,z,t) - \overline{\vec{u}}(z,t)$, where the overbar indicates the horizontal average. Exponential growth rates for the velocity perturbation components are defined as

$$\sigma_u = \frac{1}{2}\frac{d}{dt}\ln < \overline{u'^2} >; \quad \sigma_v = \frac{1}{2}\frac{d}{dt}\ln < \overline{v'^2} >; \quad \sigma_w = \frac{1}{2}\frac{d}{dt}\ln < \overline{w'^2} > . \tag{2.4}$$

Angle brackets denote an average over the vertical domain $0 \leq z \leq L_z$.

Evolution of the growth rates for each of the three cases is shown in figure 3.2. In each case, the initial perturbations adjust quickly to a state in which all three components of the perturbation kinetic energy grow at a common, nearly steady rate indicative of an exponentially-growing normal mode instability, i.e. salt sheets. The manifestation of this instability in the particular case of vertically localized stratification and shear is described in Smyth and Kimura (2007). The growth rate evident in figure 3.2 corresponds well with that calculated via linear stability analysis (indicated by thin, solid lines).

After a period of slowly declining growth, each case exhibits a rapid increase in spanwise kinetic energy (thick, solid curves in figure 3.2), followed by a similar period of increasing streamwise fluctuations (dash-dotted curves in figure 3.2). Close inspection shows that these growth periods coincide with the emergence of the sheet and tip instabilities, respectively. In each simulation, the growth rates associated with the two secondary instabilities subside, and the flow evolves to a state where the growth rates fluctuate around zero.

The dependence of the transition process upon the diffusivity ratio τ may be assessed via comparison of figures 3.2a-c. The maximum growth rate of the primary instability is nearly independent of τ when salt-fingering is possible, as is expected from the results of linear stability analysis (e.g. Smyth and Kimura, 2007). In contrast, the secondary instabilities show a clear dependence on τ: the sequence of events is unchanged, but

the time scale and instability strength varies. When τ is increased to 0.16, secondary instabilities appear much later, and the maximum growth rates of both instabilities are significantly reduced. At $\tau = 0.04$, the evolution is much closer to the $\tau = 0.01$ case, with only a slight delay and weakening of the secondary instabilities.

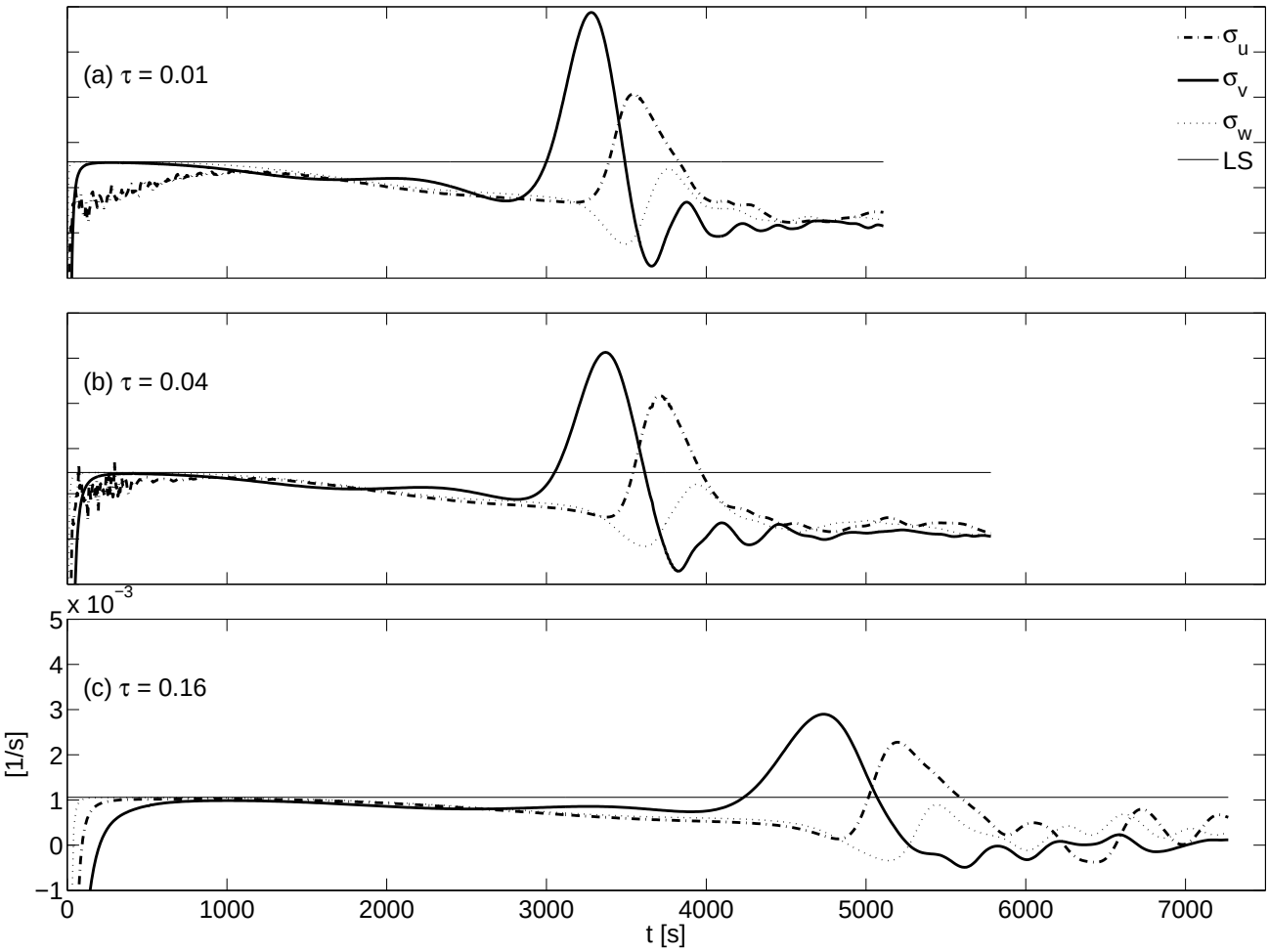

FIGURE 2.2: Growth rates as defined in equation (3.8). The LS line indicates the growth rate calculated from linear stability analysis. (a) DNS1; (b) DNS2 ; (c) DNS3.

2.5. Double-diffusive turbulence

The secondary instabilities discussed above cause the flow to evolve to a complex state, in which chaotic motions are driven by the combination of double-diffusive convection and ambient shear, and which we refer to here as double-diffusive turbulence (figure 2.1c). In this section, properties of double-diffusive turbulence are described in terms of various combinations of vertical fluxes and associated diffusivities.

The central region is expected to correspond best to the previous experiments of Stern et al. (2001), which focused on vertically-homogenous salt fingers. Effective diffusivities for saline buoyancy and momentum in that region are defined via standard flux-gradient parameterizations:

$$K_S = -\overline{w'b'_S} \Big/ \frac{\partial \overline{B_S}}{\partial z}, \quad K_U = -\overline{u'w'} \Big/ \frac{\partial \overline{U}}{\partial z}. \tag{2.5}$$

The fluxes are computed at the midplane $z = L_z/2$. The gradients are defined by fitting the saline buoyancy profile to a hyperbolic tangent profile like (4.4), but with adjustable thickness.[1] This choice captures the slow diffusion of the transition layer but is insensitive to more rapid fluctuations due to the growth of salt sheets.

The effective saline diffusivity for unsheared 3D salt fingers for $\tau = 0.01$ was estimated by Stern et al. (2001). They calculated the ratio of 2D to 3D fluxes using numerically accessible values of τ, then multiplied that ratio onto the directly computed fluxes for 2D fingers with $\tau = 0.01$. The resulting estimate of the effective saline diffusivity is $2.4 \times 10^{-5} m^2/s$, as shown by the triangle on figure 2.3a. Also shown is the smaller value computed by Stern et. al. for $\tau = 0.17$.

In our DNS experiments, K_S starts off small, then grows exponentially with the growth of the primary instability. After reaching a maximum at the onset of secondary

[1] More specifically, we fit $\overline{b_S}$ to a function $f = a \tanh[(z - Lz/2)/b]$ by minimizing the weighted error $E = \langle (\overline{b_S} - f)^2 (z - L_z/2)^2 \rangle$. The weighting emphasizes the outer regions of the profile. The central gradient is then equal to a/b.

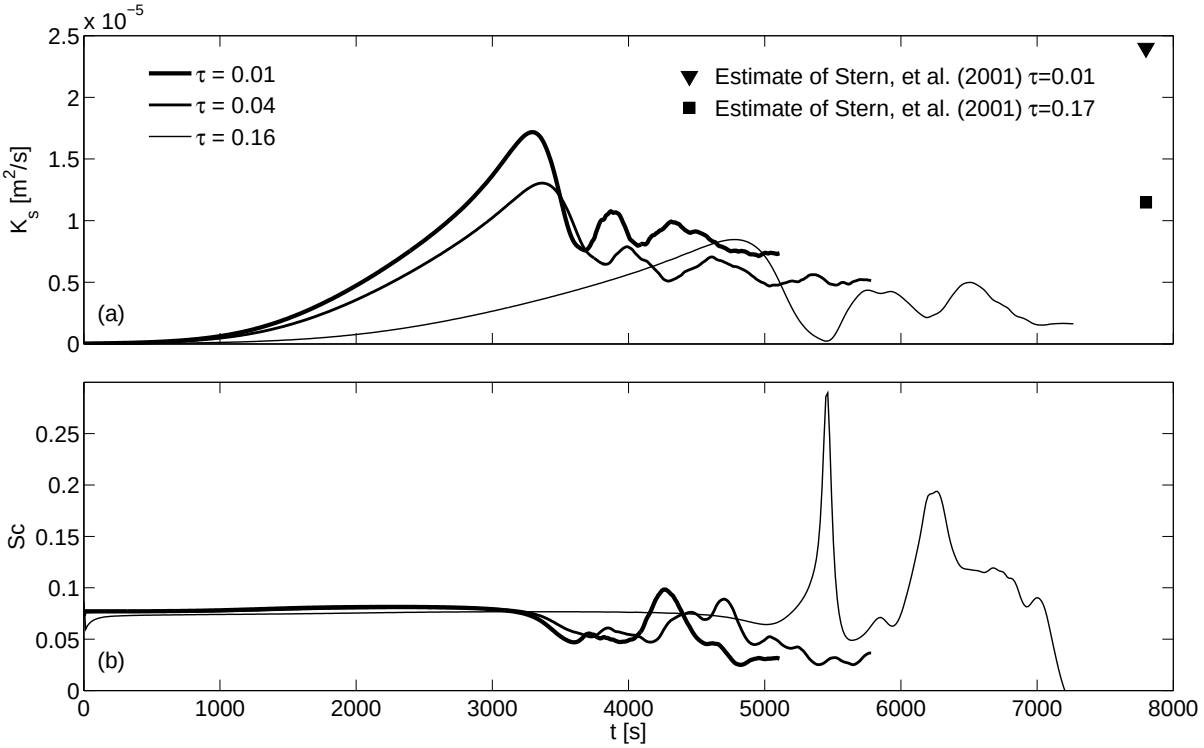

FIGURE 2.3: (a) Effective saline diffusivity. (b) Schmidt number. Thick, medium and thin curves correspond to cases DNS1, DNS2 and DNS3, respectively.

instability, K_S drops rapidly, then settles in to a state of slow decay modulated by faster fluctuations. In this late stage, K_S seems to be largely independent of τ.

The result is not consistent with the result of Stern et al. (2001), who found significant dependence on τ as shown by the symbols on figure 2.3a. Our values of K_S are generally smaller than those of Stern et. al., a difference that may be attributable to the effects of the mean shear. The difference may also be due to the difference in boundary conditions and initial profiles of thermal and saline buoyancy components. Stern et al used periodic boundary conditions in the vertical coordinate where we used rigid boundaries for vertical velocity and flux-free boundries for other variables. Our thermal and saline buoyancy component profiles had localized vertical gradients where Stern et al used uniform vertical gradients. The decay of K_S may be due to the increasing thickness of the transition layer in our experiments.

The Schmidt number, $Sc = K_U/K_S$, plays an important role in governing the thickness of thermohaline interleaving layers (D.Mueller et al., 2007; Toole and Georgi, 1981; Walsh and Ruddick, 1995). The Schmidt number is often chosen to be greater than one in order to obtain interleaving layers of realistic thickness. Ruddick (1985) and Ruddick et al. (1989) suggested that transfer of momentum by salt fingers is negligible relative to transport of heat and salt, since salt fingers rapidly lose their momentum deficits via lateral diffusion.

Smyth and Kimura (2007) demonstrate that Sc is order one or less in the linear regime. Our results confirm that Sc is less than order one in the non-linear regime (figure 2.3b). In fact, Sc drops from the linear value ~ 0.08 to values that are generally even smaller with the onset of nonlinearity. In the later stages of flow evolution, Sc fluctuates considerably, but remains $\ll 1$.

2.6. Conclusions

We have investigated DNS of salt sheets in double-diffusive stratified layer and computed turbulence statistics in the non-linear regime. Our main findings are follows.

- Primary instability generates salt sheets in accordance with Linden (1974) and Smyth and Kimura (2007). Secondary instability is via two distinct mechanisms. The sheet mode introduces motion in the spanwise direction. Subsequently, fluctuating motion in the streamwise direction is amplified via the tip mode.

- Increasing τ above the realistic value 0.01 decreases the peak values of spanwise and streamwise kinetic energy growth rates and causes secondary instabilities to evolve on a slower time scale.

- K_S increases exponentially until the onset of secondary instability and decays rapidly afterwards. After the decay period, the flow attains a molecular diffusivity-independent state in which K_S is significantly lower than the value estimated for the unsheared cases (Stern et al., 2001).

- The transfer of momentum is much less efficient in sheared salt fingers than is often assumed, i.e. the Schmidt number is less than order one in the non-linear regime. This suggests that the increase in the layer thickness of thermohaline intrusions is not purely due to momentum transfer by double diffusive instabilities.

In the future, we will perform explicit stability analyses to examine the mechanisms of the sheet and tip instabilities. Further DNS experiments will quantify the effects of Richardson number and R_ρ on transition phenomena and turbulence statistics. Mean shear may be affected by variety of "external" forces. In some cases, shear is maintained by an external forcing such as wind. The mean flow may also change direction periodically due to tides and other internal waves. The experiments presented here do not involve any

external forcing. Future studies may include the effects of external forcing by adding an appropriate forcing term to (2.2).

ACKNOWLEDGMENTS

We gratefully acknowledge useful discussions with J. Simeonov, T. Radko, B. Ruddick and W. Merryfield. This work was supported by the National Science Foundation under Grant No. 0453140. Computer time was provided via a Breakthrough Science (BTS) allocation at the National Center for Atmospheric Research. Color graphics were produced by VAPOR (www.vapor.ucar.edu). We are grateful for the help of Alan Norton in generating flow visualizations.

3. SECONDARY INSTABILITY OF SALT SHEETS

3.1. Abstract

In the presence of a vertically varying horizontal current, the salt finger instability is supplanted by the salt sheet instability. Previous direct numerical simulation (DNS) experiments on salt sheets revealed that flow become turbulent via secondary instabilities. Here, we investigate the physics of these modes using linear normal mode stability analysis. The sheet mode denotes undulation of growing salt sheets at the center of fingering regions. The tip mode appears at the edge of the salt sheets and has wavelength a few times that of the primary instability.

3.2. Introduction

Salt fingering instability can occur when gravitationally stable stratification is maintained by heat, while salt is unstably distributed. Buoyancy anomalies are created because the diffusion of heat between adjacent fingers is more rapid than the diffusion of salt; therefore, warm salty anomalies are cooled and become heavier than the adjacent fluid and vice versa for cool fresh anomalies (e.g. Kunze, 2003). Salt fingering instability can contribute to mix heat from the sea surface into the ocean interior, where evaporation and surface heating maintain the requisite salinity and temperature gradients (Schmitt, 2003). In the ocean, salt fingering instability may organize the water column into a thermohaline staircase (Radko, 2003; Schmitt, 2003).

Salt fingering can take various planforms, such as sheets, squares, and rectangles (Proctor and Holyer, 1986; Schmitt, 1994b; Stern et al., 2001). A weakly nonlinear theory of salt fingers shows that sheet (or roll) type planforms is preferred over squares and other

planforms in small-aspect-ratio thermohaline convection Proctor and Holyer (1986). In the presence of shear, salt fingering takes the form of vertical sheets aligned parallel to the flow, the "salt sheet" instability (Linden, 1974; Smyth and Kimura, 2007). Our focus here is the secondary instabilities that lead salt sheets toward the turbulent state (Kimura and Smyth, 2007).

The secondary instability of salt fingers was first proposed by Stern as collective instability (Stern, 1969). The collective instability is an oscillatory instability which is an amplification of internal waves on scales much larger than the fingers. The effects of perturbations of all wavelengths were studied in two dimensions by Holyer (1984). Holyer found a small (finger-scale) non-oscillatory secondary instability that grows faster than the collective instability in unbounded salt fingers. Holyer assumed that the basic finger state with zero growth rate permits an arbitrary value of the vertical velocity. Holyer's (1984) calculation requires a priori knowledge of the vertical velocity induced by salt fingers. Stern and Simeonov (2005) assumed instead that the vertical velocity of the finger grows exponentially in time and found "super exponential" growth of perturbations varying sinusoidally in vertical direction. Both Holyer's non-oscillatory and Stern and Simeonovs' super exponential modes contribute to disrupt the growth of salt fingers by introducing quasi-dependence on z.

The previous studies cited above have neglected the effect of sheared horizontal currents. These studies have also assumed a vertically unbounded fluid domain with uniform stratification. Here, we will employ direct numerical simulations (DNS) and secondary stability analysis to study the transition to turbulence in the presence of vertically varying horizontal current on a localized fingering layer. We will focus on the secondary instability of salt sheets that introduces quasi-periodic dependence on x, which appears at the tips of salt sheets.

Section 2 reviews the DNS model and initial conditions. Section 3 describes the se-

quence of secondary instabilities that leads to turbulence in DNS experiments. Secondary stability analysis is described in section 4. DNS and secondary stability analysis results are compared in section 5. Instability mechanisms are investigated via perturbation kinetic energy budget in section 6. Finally, conclusions are summarized in section 7.

3.3. Methodology

The Boussinesq equations are cast in a nonrotating Cartesian coordinate system $\{x, y, z\}$. Buoyancy is assumed to be a linear function of temperature and salinity. The resulting field equations describe the time evolution of the instantaneous velocity field $\vec{u}(x, y, z, t) = \{u, v, w\}$, the thermal component of buoyancy, b_T and the saline components of buoyancy, b_S as

$$\frac{D\vec{u}}{Dt} = -\nabla\pi + b\hat{k} + \nu\nabla^2\vec{u}, \tag{3.1}$$

$$\nabla \cdot \vec{u} = 0, \tag{3.2}$$

$$\frac{Db_T}{Dt} = \kappa_T\nabla^2 b_T, \tag{3.3}$$

$$\frac{Db_S}{Dt} = \kappa_S\nabla^2 b_S, \tag{3.4}$$

$$b = b_T + b_S. \tag{3.5}$$

The variable π represents the pressure scaled by the uniform characteristic density ρ_0. The buoyancy force is parallel to the vertical unit vector, $\hat{k}$. Buoyancy is defined as $b = -g(\rho - \rho_0)/\rho_0$, where g is the acceleration due to gravity in accordance with Boussinesq approximation. The kinematic viscosity of sea water is represented as ν. The variables, κ_T and κ_S are the molecular diffusivities of heat and salt, respectively.

The initial profiles of background velocity and stratification represent a stratified

double-diffusive shear layer:

$$\frac{u}{\Delta u} = \frac{b_T}{\Delta B_T} = \frac{b_S}{\Delta B_S} = \tanh\left(\frac{z}{h}\right). \tag{3.6}$$

Here, Δu is the half-change of background velocity across a transition layer of half-depth h. ΔB_T and ΔB_S are the half-changes in thermal and saline buoyancy, respectively. The half-change in total buoyancy is then $\Delta B = \Delta B_T + \Delta B_S$. Boundary conditions are periodic in the horizontal with periodicity intervals L_x and L_y in the streamwise (x) and spanwise (y) directions, respectively. Upper and lower boundaries, located at $z = -L_z/2$ and $z = L_z/2$, are impermeable ($w = 0$) and flux-free ($\partial u/\partial z = \partial v/\partial z = \partial b_T/\partial z = \partial b_S/\partial z = 0$). L_z is the domain height.

Computational resource needs are sensitive to the choice of the diffusivity ratio, $\tau = \kappa_S/\kappa_T$. In real ocean, the molecular diffusion of salt is two orders of magnitude slower than that of heat, $\tau = 0.01$. Historically, larger values of τ have been used in order to ease resource requirements (e.g. Gargett et al., 2003; Smyth et al., 2005; Stern et al., 2001). Only recently has DNS with $\tau = 0.01$ become possible (Kimura and Smyth, 2007). Secondary stability analysis is even more memory-intensive than DNS. When $\tau = 0.01$, salt sheets develop gradients too sharp to be resolved in secondary stability analysis with the available memory. Accordingly we will choose $\tau = 0.16$ for this experiment.

The numerical code used to solve (3.1) - (3.5) is described in Winters et al., (2004) with modifications as discussed by Smyth et al., (2005) and Smyth and Kimura (2007). Salinity is resolved on a fine grid with spacing equal to one half the spacing used to resolve the other fields. The resulting array dimensions for the fine grid are $(nz, ny, nx) = (768, 20, 576)$.

The density ratio $R_\rho = -\Delta B_T/\Delta B_S$ and bulk (minimum) Richardson number $Ri = \Delta B h/\Delta u^2$ were set to 1.6 and 2.0 respectively. These values were taken from observations of a thermohaline staircase off Barbados (Gregg and Sanford, 1987). The spanwise periodicity interval L_y was chosen so as to accommodate one wavelength of

the fastest-growing primary instability (Smyth and Kimura, 2007). The possibility of subharmonic secondary instabilities spanning two or more salt sheets can be included via Floquet analysis. The appropriate value for L_x is not well known a priori. Sensitivity tests showed no significant dependence of secondary instability characteristics on L_x. We used L_x=1.5m, L_y=0.04m and L_z=1.9m. L_z is larger than the layer half-thickness, $h = 0.31m$, by a factor of 6, so upper and lower boundaries are expected to have little influence on the flow evolution.

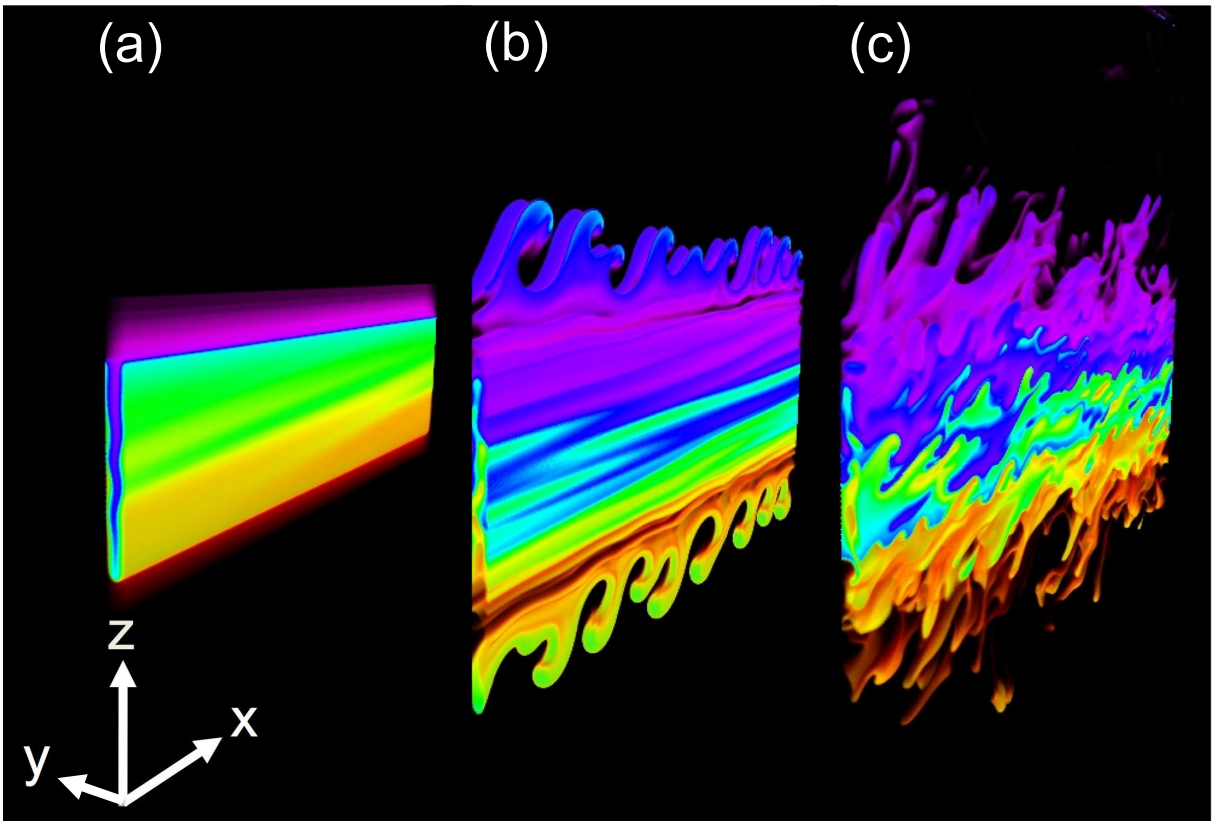

FIGURE 3.1: The saline buoyancy is colorcoded. Values range from $-0.21\Delta B_S$(blue) to $+0.21\Delta B_S$(red), with values outside that range rendered transparent. (a): Snapshot at $4132s$ shows the primary instability at finite amplitude. (b): Snapshot at $5923s$ shows the elevator mode (buckling of the salt sheets). (c): Snapshot at $7991s$ shows the tip mode (ripples with short wavelength at the top and bottom of the salt sheets).

Figure 3.1 shows three snapshots of the evolving saline buoyancy field. In figure 3.1a, a planar region of rising and sinking motions generates the spanwise gradient in

salinity at the center; this is the primary instability (salt sheet) instability. Undulations of salt-sheets at the mid depth are equivalent to Holyer's (1984) non-oscillatory and Stern and Simeonovs' (2005) super-exponential modes, found in unbounded salt fingers. At the edges of salt sheets, rising and sinking motions compresses the fluid, generating the vertical gradient of salinity. At this stage, x dependence is relatively weaker than the dependence on y and z. The basic background states can be well described as a function of y and z. Secondary circulation introduces quasiperiodic dependence on x (figure 3.1b). The x-dependence has the strongest signals at the top and bottom edges of the salt sheets; therefore, we identify this motion as the tip mode. The x-dependence resembles the shear-tilted salt fingers observed by Kunze et al. (1987), using optical microstructure from a free-fall shadowgraph profiler in the water column east of Barbados. This secondary circulation brings the flow into turbulent regime shown in figure 3.1c).

Secondary instability growth is now analyzed using an instantaneous exponential growth rate for the velocity fluctuations. The velocity fluctuations are

$$\vec{u}'(x,y,z,t) = \vec{u}(x,y,z,t) - < \vec{u}(x,y,z,t) >_x \tag{3.7}$$

where the angle bracket indicates the average over streamwise direction. Exponential growth rates for the velocity perturbation components are defined as

$$\sigma_u = \frac{1}{2}\frac{d}{dt}\ln < u'^2 >_{yz}; \quad \sigma_v = \frac{1}{2}\frac{d}{dt}\ln < v'^2 >_{yz}; \quad \sigma_w = \frac{1}{2}\frac{d}{dt}\ln < w'^2 >_{yz} . \tag{3.8}$$

Angle brackets and subscript denote an average over the spanwise and vertical domain.

Evolution of the growth rates is shown in figure 3.2. After a short adjustment period, σ_v and σ_w increase linearly between $t \approx 2500$ and $t \approx 3500$ and followed by the increase in σ_u. Linear increase in growth rates with increasing time suggest a superexpoential mode, which is found in the secondary stability analysis of salt-fingers by Stern (2003). All three components of growth rates form local peaks at $t \approx 4200$. After a period of rapid decaying growth rates, we observe a peak of the streamwise growth (red curve in

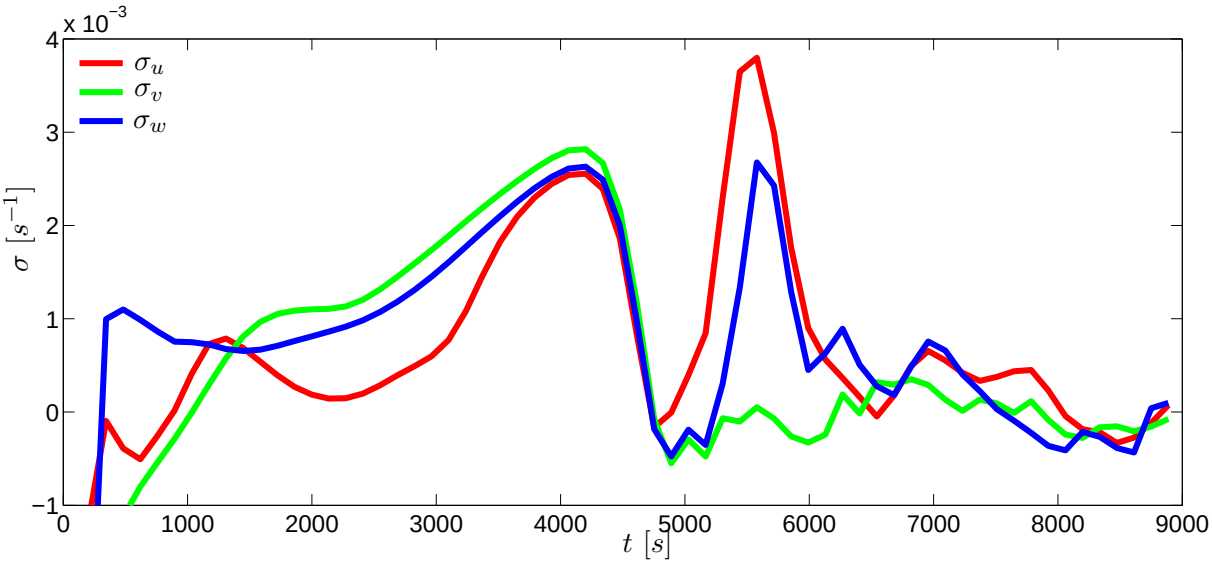

FIGURE 3.2: Evolution of growth rates as defined in equation (3.8) from DNS.

figure 3.2, at $t \approx 5700s$) and smaller peak of the vertical growth rate (blue curve in figure 3.2, at $t \approx 5700s$). These peaks indicate the presence of secondary instabilities.

Stern and Simeonovs' (2005) secondary stability analysis of salt-fingers considered the effect of the evolving mean flow and found superexponential growth. In this study, the presence of the mean streamwise velocity makes it difficult to account for the time evolution of the mean flow in the stability analysis. Instead for the purpose of the secondary stability analysis, we assume that the background flow does not change with respect to time, i.e. we make the frozen flow approximation.

3.4. Secondary stability analysis

We hypothesize that variability caused by the growth of the salt sheets to finite amplitude drives the secondary instability. We therefore define a background flow that includes the salt sheets by applying an average over streamwise (x) direction to the DNS fields. The velocity, buoyancy and pressure terms are then separated into two parts, the

background state (upper case) and a perturbation (lower case with primes),

$$\vec{u} = U(y,z)\hat{i} + V(y,z)\hat{j} + W(y,z)\hat{k} + \epsilon\vec{u'}(x,y,z,t); \tag{3.9}$$

$$b_T = B_T(y,z) + \epsilon b'_T(x,y,z,t); \tag{3.10}$$

$$b_S = B_S(y,z) + \epsilon b'_S(x,y,z,t); \tag{3.11}$$

$$\pi = \Pi(y,z) + \epsilon\pi'(x,y,z,t). \tag{3.12}$$

Our objective is to investigate the growth of the perturbations. The mean buoyancy, $B(y,z)$ is defined as $B(y,z) = B_T(y,z) + B_S(y,z)$. We substitute (3.9) - (3.12) into (3.1) - (3.5) and collect the $O(\epsilon)$ terms:

$$\frac{\partial u'}{\partial t} + \left[U\frac{\partial}{\partial x} + V\frac{\partial}{\partial y} + W\frac{\partial}{\partial z}\right]u' + \left[v'\frac{\partial}{\partial y} + w'\frac{\partial}{\partial z}\right]U = -\frac{\partial \pi'}{\partial x} + \nu\nabla^2 u', \tag{3.13}$$

$$\frac{\partial v'}{\partial t} + \left[U\frac{\partial}{\partial x} + V\frac{\partial}{\partial y} + W\frac{\partial}{\partial z}\right]v' + \left[v'\frac{\partial}{\partial y} + w'\frac{\partial}{\partial z}\right]V = -\frac{\partial \pi'}{\partial y} + \nu\nabla^2 v', \tag{3.14}$$

$$\frac{\partial w'}{\partial t} + \left[U\frac{\partial}{\partial x} + V\frac{\partial}{\partial y} + W\frac{\partial}{\partial z}\right]w' + \left[v'\frac{\partial}{\partial y} + w'\frac{\partial}{\partial z}\right]W = -\frac{\partial \pi'}{\partial z} + b'_T + b'_S + \nu\nabla^2 w', \tag{3.15}$$

$$\frac{\partial u'}{\partial x} + \frac{\partial v'}{\partial y} + \frac{\partial w'}{\partial z} = 0, \tag{3.16}$$

$$\frac{\partial b'_T}{\partial t} + \left[U\frac{\partial}{\partial x} + V\frac{\partial}{\partial y} + W\frac{\partial}{\partial z}\right]b'_T + \left[v'\frac{\partial}{\partial y} + w'\frac{\partial}{\partial z}\right]B_T = \kappa_T\nabla^2 b'_T, \tag{3.17}$$

$$\frac{\partial b'_S}{\partial t} + \left[U\frac{\partial}{\partial x} + V\frac{\partial}{\partial y} + W\frac{\partial}{\partial z}\right]b'_S + \left[v'\frac{\partial}{\partial y} + w'\frac{\partial}{\partial z}\right]B_S = \kappa_S\nabla^2 b'_S. \tag{3.18}$$

A diagnostic equation for the pressure,

$$\nabla^2\pi' = -2\frac{\partial v'}{\partial x}\frac{\partial U}{\partial y} - 2\frac{\partial w'}{\partial x}\frac{\partial U}{\partial z} - 2\frac{\partial v'}{\partial y}\frac{\partial V}{\partial y} - 2\frac{\partial v'}{\partial z}\frac{\partial W}{\partial y} - 2\frac{\partial w'}{\partial y}\frac{\partial V}{\partial z} - 2\frac{\partial w'}{\partial z}\frac{\partial W}{\partial z} + \frac{\partial b'_T}{\partial z} + \frac{\partial b'_S}{\partial z}, \tag{3.19}$$

is obtained by applying $\nabla\cdot$ to (3.13) - (3.15) and using (3.16). Note that (3.13) decouples from the other equations, so that the sytem to be solved is (3.14), (3.15), (3.17), (3.18) and (3.19).

The perturbations are assumed to have the same spanwise periodicity as the salt sheets, and take the normal mode form:

$$u'(x,y,z,t) = e^{\sigma t+ikx}\sum_{n=-(N-1)/2}^{(N-1)/2}\sum_{m=0}^{M}\hat{u}_{n,m}\cos\left(\frac{m\pi}{L_z}z\right)e^{i\left(\frac{2n\pi}{L_y}+\mu\frac{2\pi}{L_y}\right)y}; \tag{3.20}$$

$$v'(x,y,z,t) = e^{\sigma t+ikx}\sum_{n=-(N-1)/2}^{(N-1)/2}\sum_{m=0}^{M}\hat{v}_{n,m}\cos\left(\frac{m\pi}{L_z}z\right)e^{i\left(\frac{2n\pi}{L_y}+\mu\frac{2\pi}{L_y}\right)y}; \tag{3.21}$$

$$w'(x,y,z,t) = e^{\sigma t+ikx}\sum_{n=-(N-1)/2}^{(N-1)/2}\sum_{m=1}^{M}\hat{w}_{n,m}\sin\left(\frac{m\pi}{L_z}z\right)e^{i\left(\frac{2n\pi}{L_y}+\mu\frac{2\pi}{L_y}\right)y}; \tag{3.22}$$

$$b'_T(x,y,z,t) = e^{\sigma t+ikx}\sum_{n=-(N-1)/2}^{(N-1)/2}\sum_{m=1}^{M}\hat{b_T}_{n,m}\sin\left(\frac{m\pi}{L_z}z\right)e^{i\left(\frac{2n\pi}{L_y}+\mu\frac{2\pi}{L_y}\right)y}; \tag{3.23}$$

$$b'_S(x,y,z,t) = e^{\sigma t+ikx}\sum_{n=-(N-1)/2}^{(N-1)/2}\sum_{m=1}^{M}\hat{b_S}_{n,m}\sin\left(\frac{m\pi}{L_z}z\right)e^{i\left(\frac{2n\pi}{L_y}+\mu\frac{2\pi}{L_y}\right)y}; \tag{3.24}$$

$$\pi'(x,y,z,t) = e^{\sigma t+ikx}\sum_{n=-(N-1)/2}^{(N-1)/2}\sum_{m=0}^{M}\hat{\pi}_{n,m}\cos\left(\frac{m\pi}{L_z}z\right)e^{i\left(\frac{2n\pi}{L_y}+\mu\frac{2\pi}{L_y}\right)y}. \tag{3.25}$$

where k is the real streamwise wavenumber and $\sigma = \sigma_r + i\sigma_i$ is the complex exponential growth rate of the perturbation. The variable, $e^{\mu\frac{2\pi y}{L_y}}$ is a Floquet factor, which accounts for subharmonic modes. A matrix eigenvalue problem is obtained by combining the equations (3.14), (3.15), (3.17),(3.18) and (3.19) with (3.20) - (3.25):

$$\sigma\hat{x} = A\hat{x}, \tag{3.26}$$

where σ is the eigenvalue, A is the stability matrix and $\hat{x}$ is the concatenation of the

disturbances, $\hat{v}_{n,m}$, $\hat{w}_{n,m}$, $\hat{b_T}_{n,m}$ and $\hat{b_S}_{n,m}$. The parameters M and N determine vertical and spanwise resolution levels, respectively.

The background flow, U, V, W, B_T and B_S was taken from a snapshot of DNS at 4132s. Use of the oceanic value for τ increases the rank of the stability matrix to $10^5 - 10^6$, which is far beyond our available computational power. For the present case $\tau = 0.16$, the calculation of multiple modes was done with $(M, N) = (384, 10)$. For the subharmonic modes, we have varied $\mu = 0, \frac{1}{2}, \frac{1}{3}$, and $\frac{1}{4}$.

In figure 3.3, we identify two distinct modes; the tip mode and sheet mode. The tip mode is a subharmonic mode occurs at $\mu = 1/2$, which has the maximum growth rate of $\sigma_r = 3.2 \times 10^{-3} s^{-1}$ at $k = 62 m^{-1}$. The tip mode is strongly oscillatory mode with $\sigma_i = 46 \times 10^{-3} s^{-1}$, which is an order of magnitude larger than the real part. The phase speed of the tip mode is, $-\sigma_i/k = -7.4 \times 10^{-4} m s^{-1}$, which is half of Δu. The sheet mode has maximum growth rate at $k = 0$, where $\sigma_r = 8 \times 10^{-4} s^{-1}$. The sheet mode is nearly stationary (see figure 3.3b). The sheet mode is analogous to Holyer's (1984) stationary mode, while the tip mode introduces quasi-periodic dependence on x. In sheared, bounded salt fingers, the tip mode is the fastest growing mode, which is oscillatory (see 3.3a). The undulation of salt-fingering can be resolved in two dimensions (Shen, 1995; Stern and Simeonov, 2005), whereas the tip mode is inherently three dimensional. The growth rate of the tip mode is nearly three times larger than that of the sheet mode. We expect that the tip mode signal will dominate over the sheet mode. In the next section, we will compare the tip mode with the DNS.

3.5. Comparison of the tip mode and DNS

We next compare the spatial structures of the eigenmodes with perturbations seen in the DNS. We found that the fastest growing mode had $\mu = \frac{1}{2}$. This indicates that

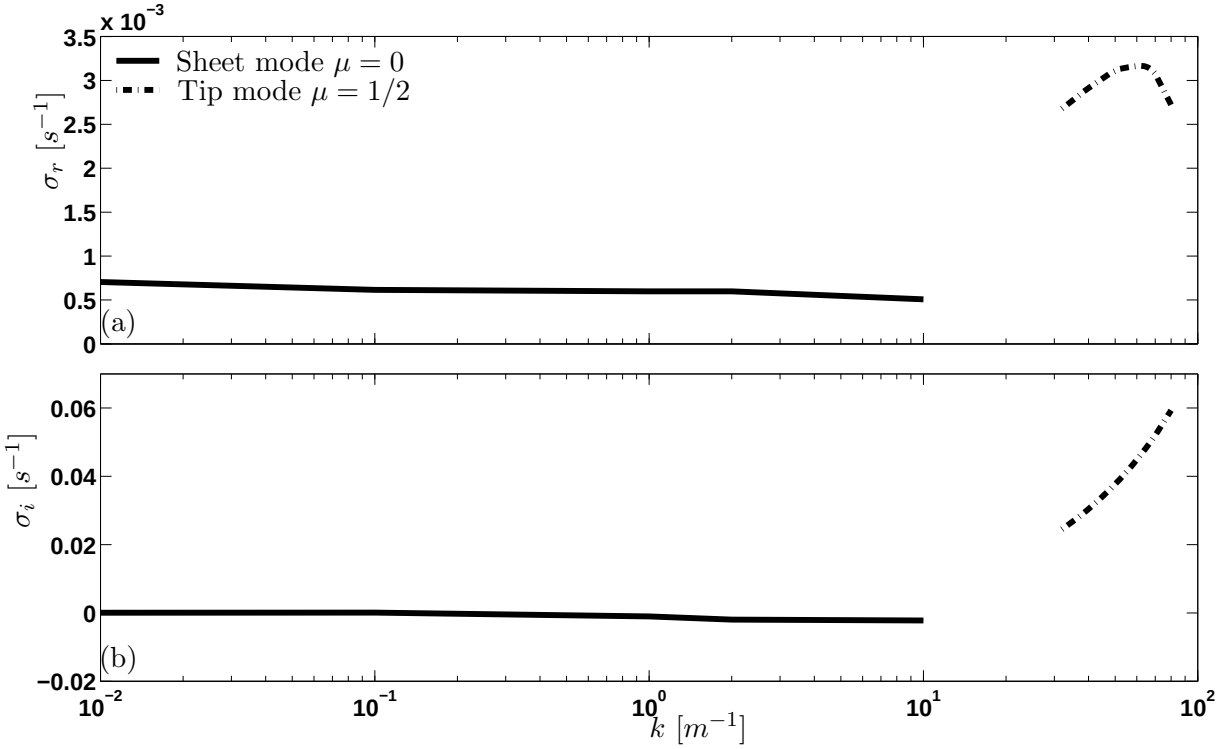

FIGURE 3.3: Real parts of growth rates (a) and imaginary part of growth rates (b) versus streamwise wavenumber for the sheet and tip modes at $t = 4132s$.

the spanwise domain size needs to be at least doubled to accommodate the spanwise disturbance that is caused by salt sheets. Figure 3.4 shows a case where $L_y = 4\lambda_{fg}$. The spanwise wavelength of ripples at the top edges of salt sheets corresponds to double the wavelength of single salt sheet. In contrast, the undulation near the center of the layer introduce no new spanwise dependence. The growth rate of the tip mode is three times larger than that of sheet mode. We expect the tip mode signals will dominate the subsequent flow. We will compare the tip mode and DNS.

Streamwise dependence introduced by the tip mode is verified by the DNS data at the times of peak streamwise and vertical growth seen in figure 3.2: $5923s$. The secondary stability analysis shows maximum growth rate at $k = 62m^{-1}$, so the predicted wavelength is $2\pi/k = 0.1m$. This wavelength corresponds with the ripples at the top and bottom of the salt sheets at $5923s$ to within a few tens of percent (see figure 3.5). The eigenfunction (not shown, though see figures 3.7b,c,d, and 3.8c in the following section) has energy concentrated near the tips of the salt sheets, as expected. We conclude that the spatial structure of the modes at $k = 62m^{-1}$ correspond very well with the tip modes seen in the DNS, given the limitations of spatial resolution and the frozen flow approximation.

3.6. Mechanisms of instability

As an initial hypothesis, one might imagine that the tip mode is responsible for two events:

1. introduction of quasi-periodic dependence on x,

2. undulation of salt sheets in y direction.

These two events can be thought as a combination of shear and buoyancy driven instabilities.

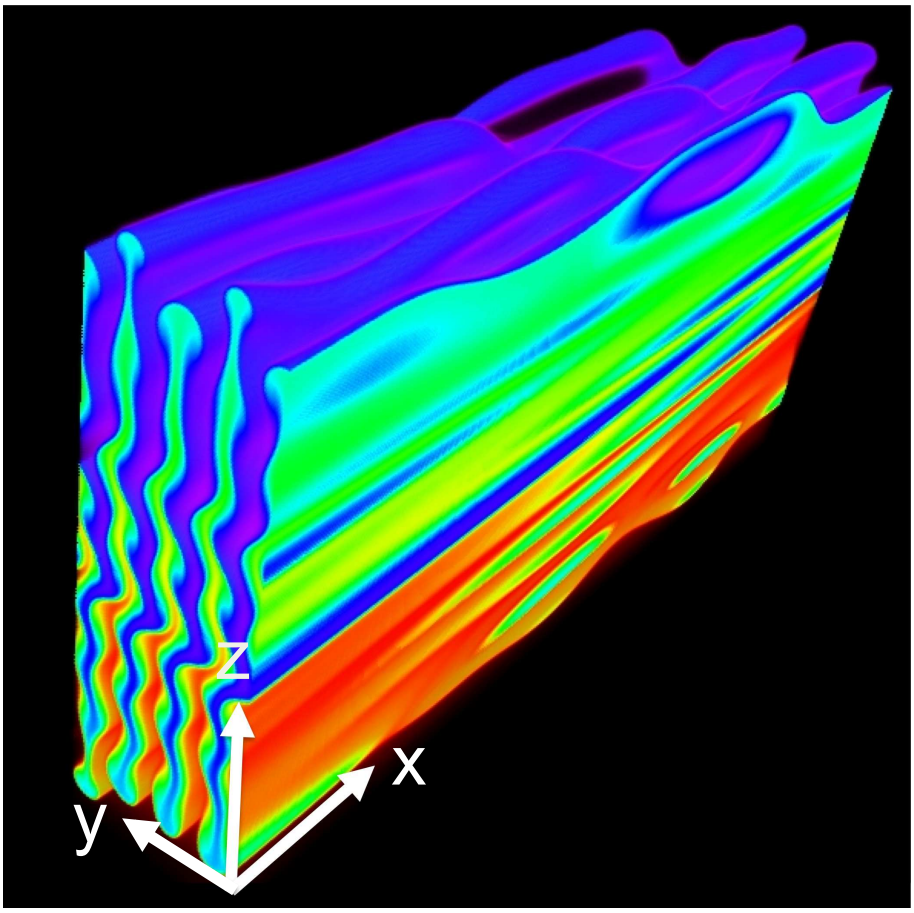

FIGURE 3.4: A snapshot of saline buoyancy field from DNS initialized with four salt sheets at $t = 5932s$. Values range from $-0.21\Delta B_S$(blue) to $+0.21\Delta B_S$(red), with values outside that range rendered transparent. The growth of salt sheets at the top edges are not uniform in y. Instead, every other salt sheets has the same height, i.e, the growth of salt sheets create the spanwise disturbance that is doubled the wavelength of single salt sheet.

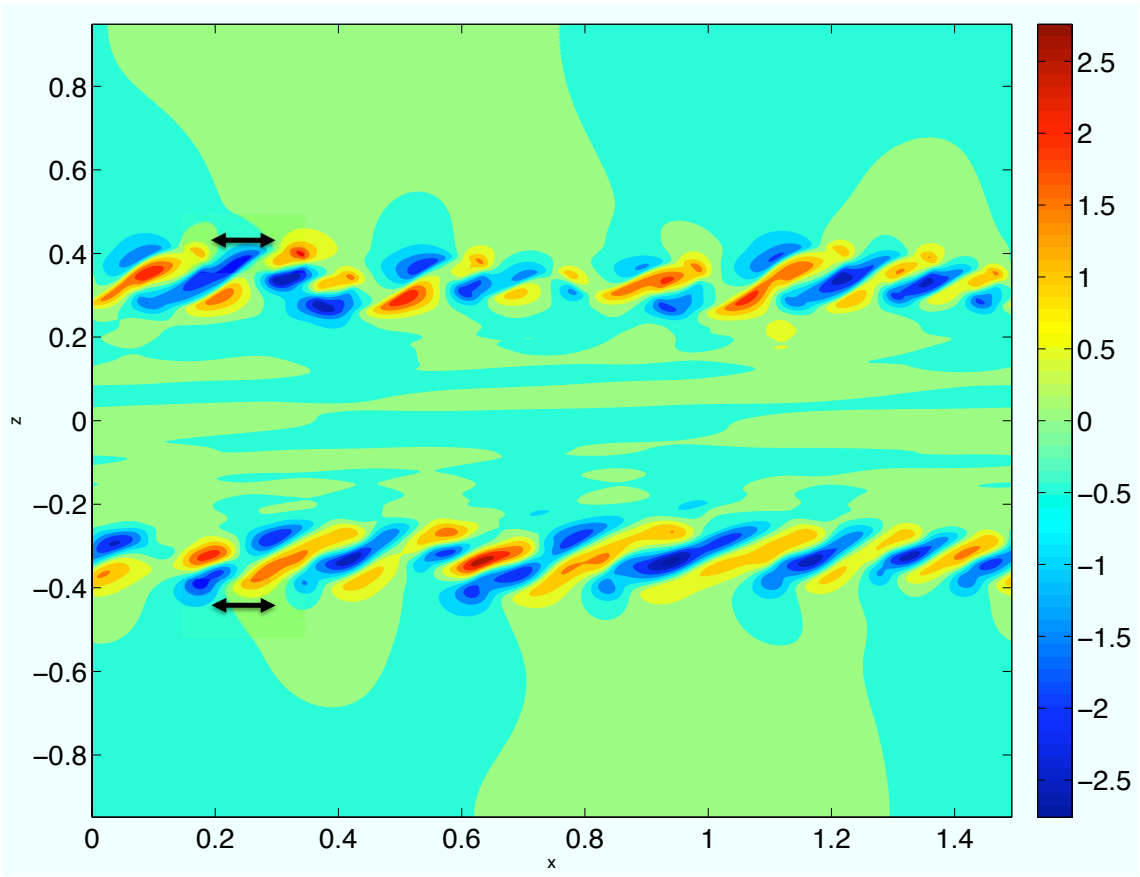

FIGURE 3.5: Streamwise velocity perturbation, $u'(x, y = 0, z, t = 5923s) \times 10^4$, in color from DNS. Arrows at the tip and bottom indicate the wavelength, $0.1m$, predicted for the tip mode.

The primary salt sheet instability squeezes the fluid at the edges of rising and sinking fluid, creating, sharp gradients of velocity and buoyancy. This localized shear layer can be susceptible to Kelvin-Helmholtz instability, which creates quasi-periodic dependence on x. Alternatively, faster diffusion of heat relative to salt creates regions of gravitationally unstable fluid at the extremities of the salt sheets. This could pinch the fluid at the edges, creating blobs of unstable fluid, which is seen in DNS of salt fingers (Shen, 1995). The lateral buoyancy gradients created by the blobs between salt sheets may support sloping convection, which creates periodic dependence on x.

The geometry of the salt sheet suggests that the disruption of the salt sheet is a shear instability driven by the y-dependence of the background vertical velocity. This supposition has underlain attempts to parameterize fluxes due to salt fingers (e.g. Kunze, 2003). Such an instability may be described approximately by a solution of Rayleigh's equation with a sinusoidal profile of background velocity $W = W_0 \sin(k_y y)$. A numerical solution for this case (Hazel, 1972) yields a fastest-growing mode with wavenumber equal to $k_y/1.8$. In other words, the z-wavelength of the shear instability is predicted to exceed the y-wavelength of the salt sheets by a factor 1.8. In the related case of two-dimensional unsheared salt fingers, the secondary instability has wavelength in the z direction $1.7-1.8$ times of the original wavelength of salt fingers over a wide range of parameter values (Stern and Simeonov, 2005). This correspondence with Hazel (1972) suggests that the undulation of salt fingers may be driven by the periodic shear of the vertical motions of salt fingers. The picture is complicated, however, by the effect of viscosity. The Reynolds number computed on the scales of the salt sheet is $O(1)$, small enough to quench shear instability.

To quantify the relative importance of buoyancy and shear forcing, we analyzed the sources of perturbation kinetic energy, defined as

$$K_e(y,z,t) = \frac{1}{2} < \vec{u'} \cdot \vec{u'} >_x . \tag{3.27}$$

The time rate of change in perturbation kinetic energy is obtained by taking the scalar product of $\vec{u'}$ with the momentum equations (3.13) - (3.15). The resulting equation is

$$\frac{\partial K_e}{\partial t} + \nabla \cdot F = Sh + B + \epsilon_d, \tag{3.28}$$

where

$$Sh = - < u'v' \frac{\partial U}{\partial y} >_x - < u'w' \frac{\partial U}{\partial z} >_x \tag{3.29}$$

$$- < v'v' \frac{\partial V}{\partial y} >_x - < v'w' \frac{\partial V}{\partial z} >_x \tag{3.30}$$

$$- < w'v' \frac{\partial W}{\partial y} >_x - < w'w' \frac{\partial W}{\partial z} >_x; \tag{3.31}$$

$$B = < w'b'_T >_x + < w'b'_S >_x; \tag{3.32}$$

$$\epsilon_d = -2\nu < e_{i,j} e_{i,j} >_x; \qquad e_{ij} = \frac{1}{2}\left(\frac{\partial u'_i}{\partial x_j} + \frac{\partial u'_j}{\partial x_i} \right). \tag{3.33}$$

The Sh, B and ϵ_d represent the shear production, buoyancy production and dissipation respectively. The second term on the left-hand side of (3.28) is the divergence of a sum of advective, pressure-driven and viscous fluxes. We will not consider this term since it vanishes when the spatial average is taken.

The evolution of perturbation kinetic energy budget over time is analyzed using an instantaneous exponential growth rate for the velocity fluctuations:

$$\sigma_{Total} = \frac{1}{2 < K_e >_{yz}} \frac{d < K_e >_{yz}}{dt}. \tag{3.34}$$

The relative importance of the physical processes described by the individual terms on the right-hand side of (3.28) is quantified using partial growth rates of the form

$$\sigma_S = \frac{< Sh >_{yz}}{2 < K_e >_{yz}} \tag{3.35}$$

and similarly for the buoyancy, σ_B and the dissipation, σ_d. The K_e budget can then be written as

$$\sigma_{Total} = \sigma_S + \sigma_B + \sigma_d. \tag{3.36}$$

Because σ_d is negative definite, the perturbation kinetic energy can only be supplied by the shear and buoyancy production terms.

Individual terms of σ_S and σ_B can be written as

$$\sigma_S = \sigma_{uv} + \sigma_{uw} + \sigma_{vv} + \sigma_{vw} + \sigma_{wv} + \sigma_{ww}, \tag{3.37}$$

$$\sigma_B = \sigma_{wt} + \sigma_{ws}. \tag{3.38}$$

These individual terms take the form of (3.35), where the numerator is replaced by the individual shear and buoyancy production terms described in (3.31) and (3.32).

3.6.1 Shear production mechanisms

The generation of perturbation kinetic energy can be accomplished by shear production which is a sum of interactions of Reynolds stresses with components of the mean shear. Since we considered the background velocity of U, V, and W with y and z dependence, there are six shear production terms described in (3.37). We will identify the dominant component of the shear production term for the tip mode.

Two dominant terms that convert the mean to perturbation kinetic energy are σ_{ww} and σ_{uw} (figure 3.6). The largest term σ_{ww} suggests that the straining of the perturbation vertical velocity by the vertical convergence $\partial W/\partial z < 0$ near the extremities of the salt sheets generates perturbation kinetic energy. The second largest term, σ_{uw} is the interaction between Reynolds stress, $< u'w' >_x$ and the ambient shear $\partial U/\partial z$ (figure 3.6). In contrast, conversion from the perturbation to mean kinetic energy is accomplished mainly by σ_{wv}. The smallest term σ_{wv} is the advection of the Reynolds stress, $< w'v' >_x$ by the spanwise gradient of the vertical velocity, $\partial W/\partial y$. The negative σ_{wv} suggests that the undulation of salt sheets is not caused by the spanwise gradient in the vertical velocity.

The spatial structures of σ_{ww}, σ_{uw}, and σ_{wv} were investigated by plotting $< -w'w'\frac{\partial W}{\partial z} >_x$, $< -u'w'\frac{\partial U}{\partial z} >_x$, and $< -w'v'\frac{\partial W}{\partial y} >_x$ (figure 3.7b, c, and d). The two dominant shear production terms have signals concentrated at the center of the bottom edge of the growing

salt sheets (figures 3.7b and c). Conversion of the turbulent to mean kinetic energy occurs at the bottom of shearing regions of salt sheets (figure 3.7d). The conjugate mode (not shown here) has signals concentrated at the top edge. None of the dominant shear production terms in the tip mode has a signal in the interior of the salt sheets.

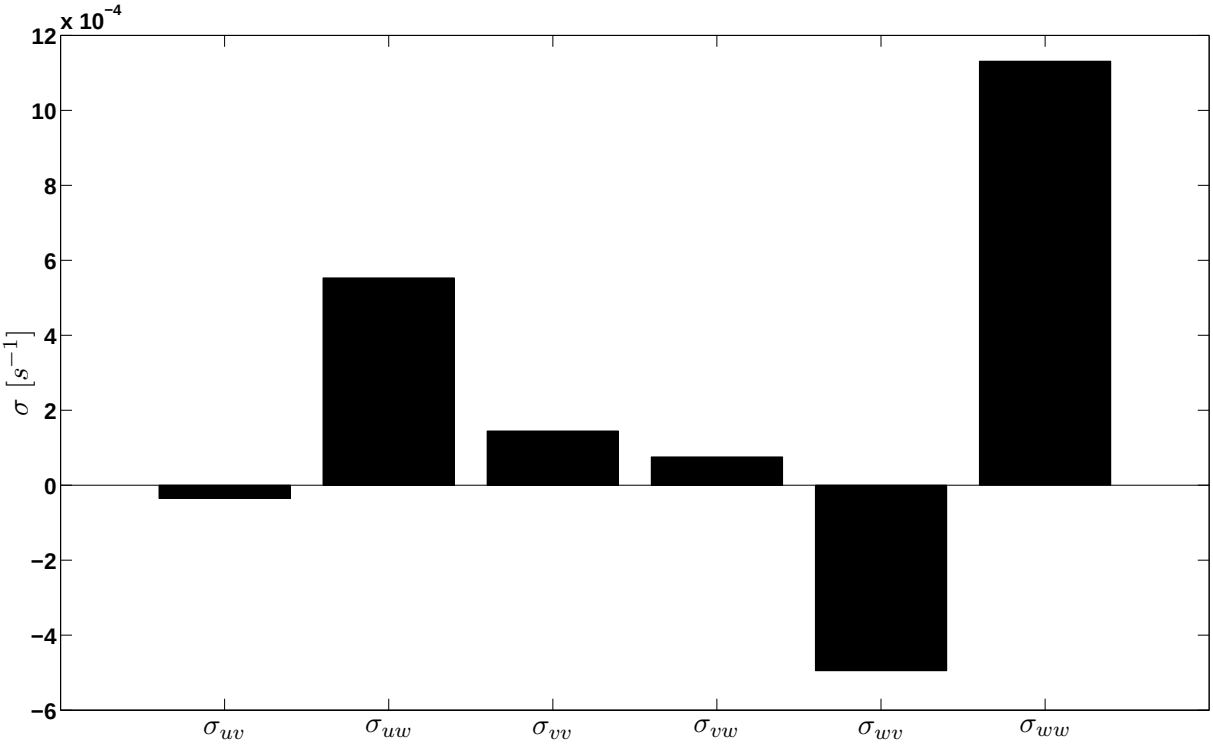

FIGURE 3.6: Partial growth rates of individual shear production terms.

3.6.2 Buoyancy production mechanisms

An alternative mechanism for instability growth is convection as quantified by the buoyancy production term $\sigma_B = \sigma_{wt} + \sigma_{ws}$. The mean buoyancy is unstably distributed at the bottom and upper edges of salt sheets (figure 3.8a). The tip mode has the strongest buoyancy production in the regions of strong vertical density gradients (figure 3.8c). Buoyancy production is an order of magnitude stronger than the shear production (figure 3.9). The thermal buoyancy production is negative $\sigma_{wt} = -0.026s^{-1}$, where the saline buoy-

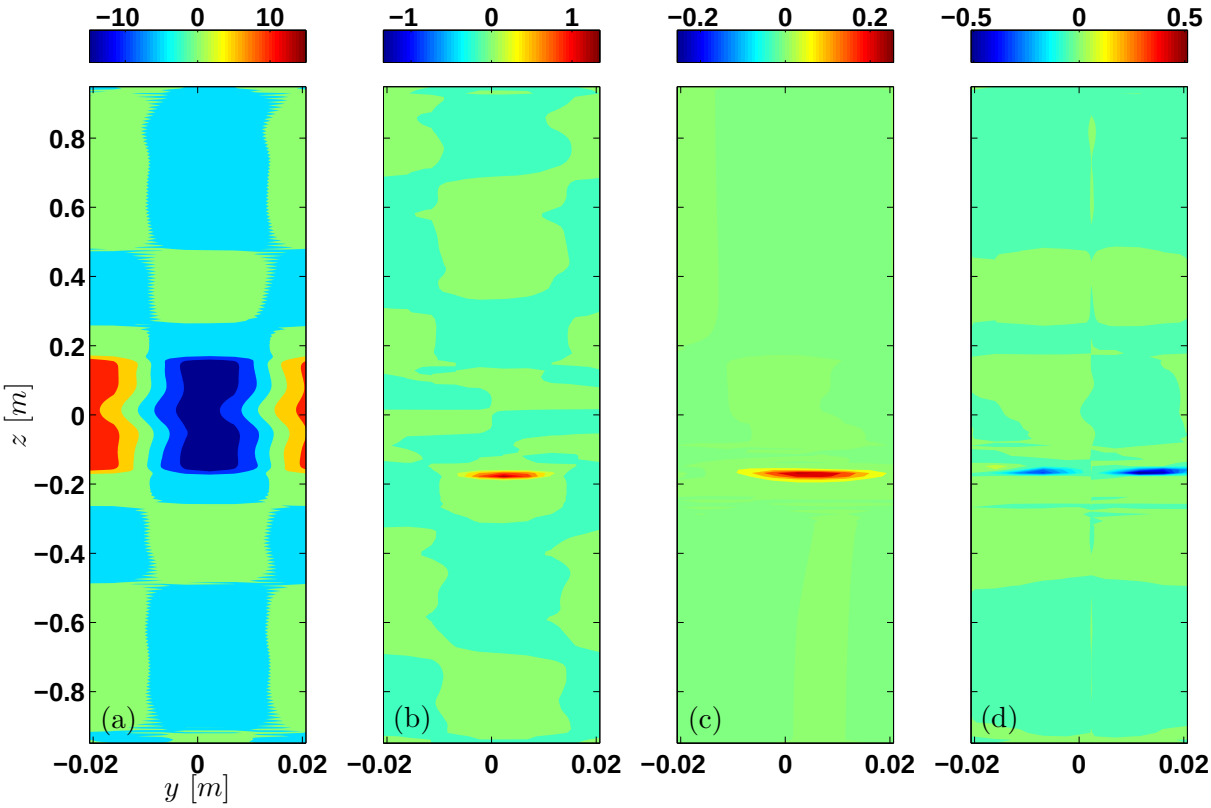

FIGURE 3.7: (a) Mean $W \times 10^5$ at DNS 4132s. (b) $< -w'w'\frac{\partial W}{\partial z} >_x$ tip mode. (c) $< -u'w'\frac{\partial U}{\partial z} >_x$ tip mode. (d) $< -w'v'\frac{\partial W}{\partial y} >_x$ tip mode.

ancy production is positive $\sigma_{ws} = 0.042s^{-1}$. Thus, the buoyancy production is driven by the release of gravitational potential energy stored in the saline buoyancy.

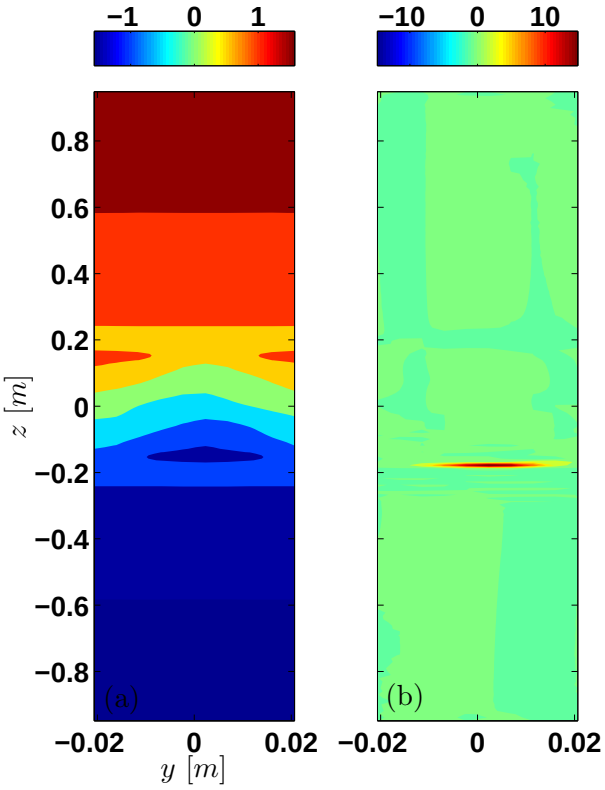

FIGURE 3.8: (a) Mean $B \times 10^5$ at DNS 4132s. Red indicates the positive buoyancy and blue is for the negative buoyancy. (b) $< w'b' >_x$ tip mode.

This is a noteworthy result, especially for the mechanism of the undulation of salt sheet, whose wavelength corresponds so well with that of shear instability. One must suspect that the dominance of buoyancy production is in some sense an artifact of the assumptions that underlie our normal mode stability analyses, i.e. that small-amplitude perturbations grow on a frozen background flow. To check this, we compute the analogous production terms in the DNS output, where the assumptions of linear normal mode theory are not made. The partial growth rates due to shear and buoyancy production for DNS are calculated using (3.37) and (3.38), as for the eigenmodes. Figure 3.10 shows that

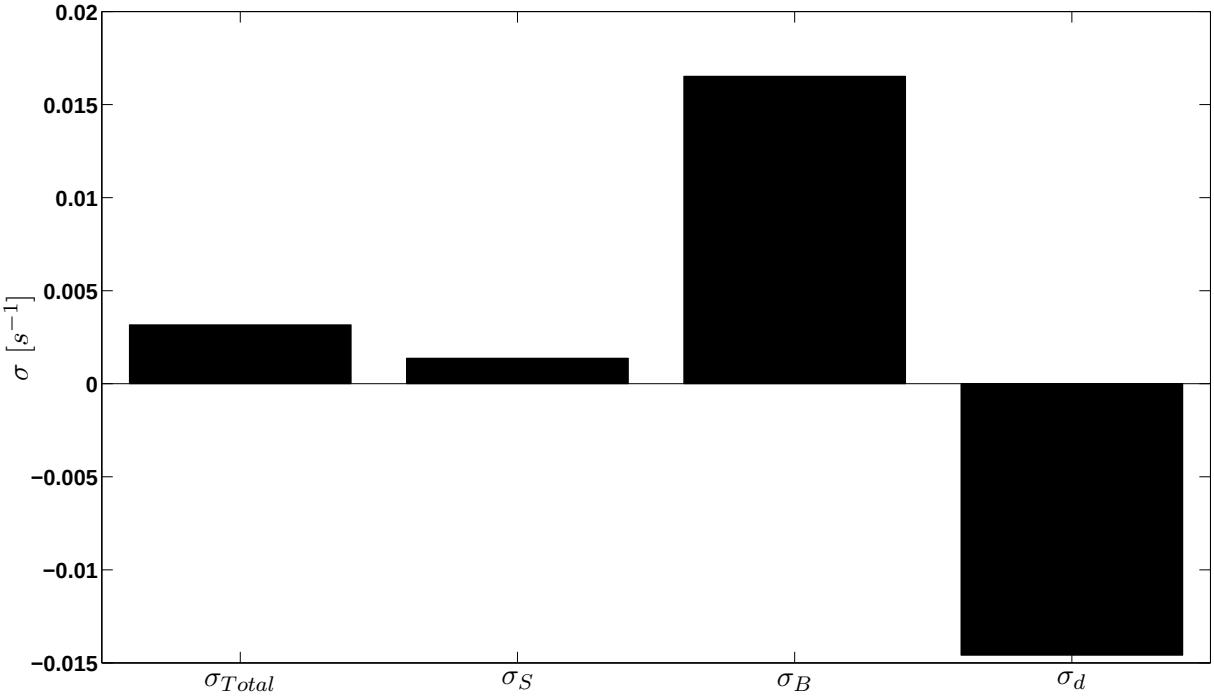

FIGURE 3.9: Partial growth rates of perturbation kinetic energy budget of the tip mode

the buoyancy production dominates over the shear productions after $t = 4132s$. The σ_B decays and reaches to a quasi-steady state: $\sigma_B \approx 10^{-3}s^{-1}$. The σ_S become negative and reaches to $\sigma_S \approx 10^{-4}s^{-1}$. We conclude that the dominance of the buoyancy production is not an artifact of either linearization or the frozen flow approximation.

3.7. Conclusions

DNS of salt sheets revealed the secondary instability, which we call the tip mode. We examined the tip mode via linear normal mode secondary stability analysis. We have also discussed mechanisms of instability as quantified by the perturbation kinetic energy budget. Our main findings are as follows:

- The tip mode can be treated approximately as linear normal mode secondary insta-

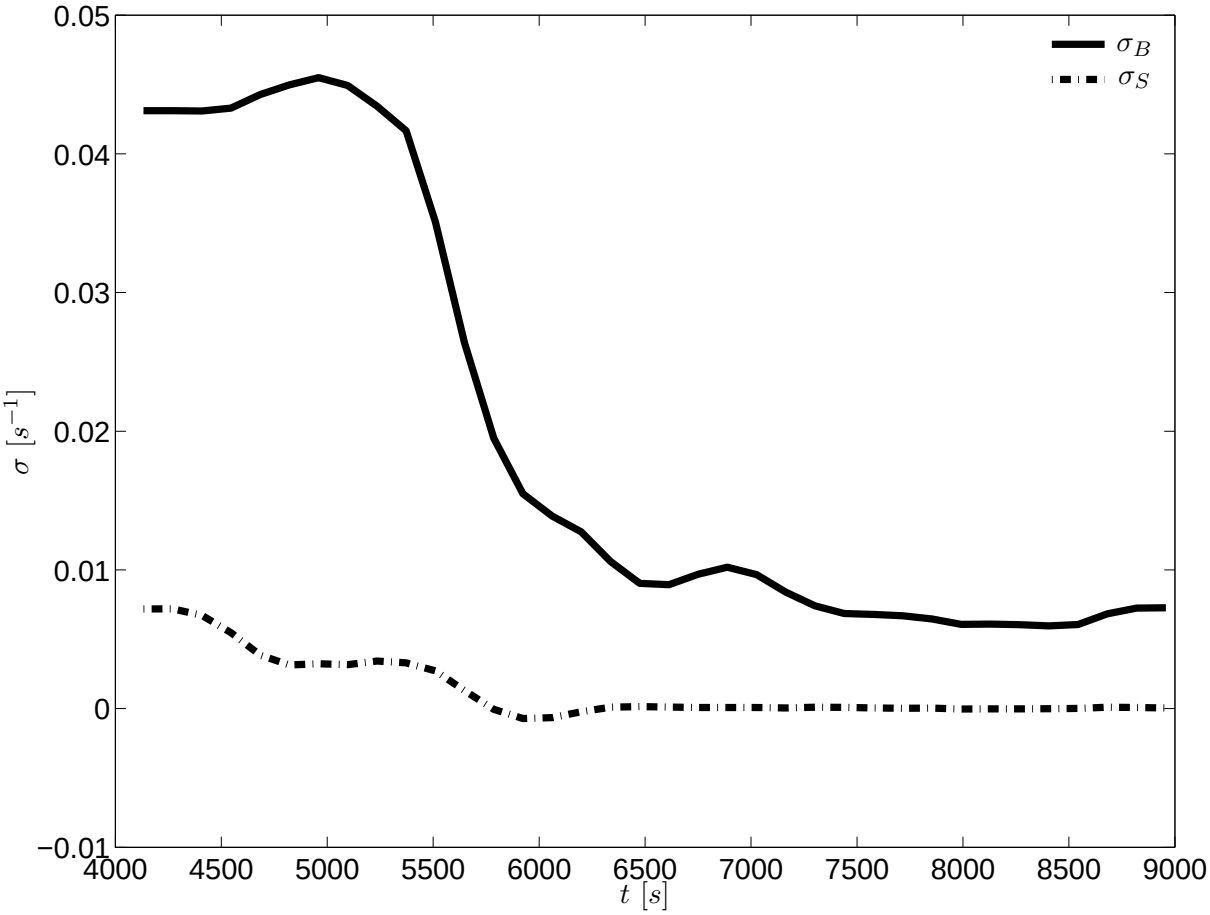

FIGURE 3.10: Evolution of partial growth rates of shear and buoyancy productions from DNS after $t = 4132s$.

bilities of the finite-amplitude salt sheets.

- The tip mode is oscillatory instability, which introduces dependence on x.

- The largest contributions to the perturbation kinetic energy of the tip mode were made by $< w'b' >_x$ and $< -w'w'\frac{\partial W}{\partial z} >_x$. The energy of both the shear and buoyancy production was concentrated at the edges of growing salt sheets where the vertical buoyancy gradient is unstable. This mode may represent the three-dimensional analogue of the pinch-off process described by Shen (1995).

- The perturbation kinetic energy growth is driven mainly by buoyancy production, i.e. σ_B is an order of magnitude larger than σ_S (figure 3.9). Dominance of buoyancy forcing has been confirmed in the DNS results, i.e. it is not an artifact of either linearization or the frozen flow approximation. This may explain why parameterizations based on the disruption of salt fingers by shear-driven instabilities have had difficulty predicting observed fluxes (e.g. Inoue et al., 2008).

Further DNS experiments are now underway to explore secondary instabilities and the development of double diffusive turbulence in different regimes of stratification and shear.

Acknowledgments. This project has benefited from discussions with Eric Kunze and Bill Merryfield. The work was supported by the National Science Foundation under Grant No. 0453140.

4. SHEARED, DOUBLE DIFFUSIVE TURBULENCE: ANISOTROPY AND EFFECTIVE DIFFUSIVITIES

4.1. Abstract

Direct numerical simulation (DNS) of sheared, double-diffusive system in a diffusively stable, localized shear layer has been performed for different Richardson number Ri and density ratio R_ρ. The result show that thermal and saline buoyancy fields become more isotropic than the velocity fields in the dissipation-range scale. When the Richardson number is infinite (unsheared case), the primary instability is salt fingering instability, cells of rising and sinking fluid. In the presence of shear, salt fingering instability is supplanted by salt sheet instability, a planar region of rising and sinking fluid, oriented parallel to the direction of the shear. After the decay of the primary instability by secondary instability, the flow become turbulent; however, the flow geometry from the primary instability bias the estimation of the turbulent kinetic energy dissipation rate ϵ even in the turbulent regime. Estimation of ϵ by assuming the isotropy in the vertical direction, a common method in the interpretations of observations, can underestimate its true value by a factor of 2 to 3. Finally, the turbulent transport associated with sheared, double-diffusive turbulence is quantified by the effective diffusivity of heat and salt. We show that the decrease in the Richardson number Ri (increase in shear) reduces the effective diffusivity of heat and salt.

4.2. Introduction

Kolmogorov (1941) proposed the idea that small-scale statistics in fully developed turbulence are universal. According to this hypothesis, anisotropy pertained in the energy-containing scale is lost in the turbulent energy cascade, so that the small scales, where

energy is finally dissipated, are statistically isotropic. The assumption of small-scale isotropy greatly simplifies both the theory of turbulence and the interpretation of microstructure measurements. Here, we will examine both mixing rates and the geometry of the dissipation range in sheared, double-diffusive turbulence by means of direct numerical simulations.

Observations of flow over a sill (Gargett et al., 1984) concluded that the isotropy assumption was accurate as long as the scale separation between Ozmidov (Ozmidov, 1965) and Kolmogorov (Kolmogorov, 1941) lengthscales was sufficiently large. Itsweire et al. (1993) tested isotropic approximations on stably stratified flows with uniform shear and stratification, using DNS, and found that dissipation rates could be underestimated by factors of 2 to 4. Smyth and Moum (2000) extended the analysis to a localized shear layer and found similar results.

In salt-fingering favorable stratification (warm, salty over cool, fresh water), the unstable vertical gradient of salinity is stabilized by temperature, but not for perturbations. The faster diffusion of heat relative to salt generates cells of sinking and rising motions, which take a variety of shapes such as squares, rectangles, and sheets (Proctor and Holyer, 1986; Schmitt, 1994b). In the presence of shear, salt-fingering instability is supplanted by salt-sheet instability. Salt-sheet instability generates alternating planar regions of rising and sinking fluid, aligned parallel to the shear (Linden, 1974). Dissipation rates in salt-fingering favorable stratification from observations are estimated by assuming isotropy (Hamilton et al., 1989; Inoue et al., 2008; St. Laurent and Schmitt, 1999). Isotropy may not be a bad assumption in the large convecting layers created by salt fingers (Hamilton et al., 1989). The assumption may not be appropriate at the interfaces where salt fingers grow and create sharp horizontal gradients in velocity, temperature, and salinity.

Estimations of these dissipation rates combined with the Osborn and Cox (1972) diffusivity model can estimate the effective diffusivities of heat, salt, and momentum.

Effective diffusivities are used to parameterize the turbulent fluxes in order to model phenomena affected by double-diffusive turbulence ranging from fine-scale thermohaline intrusions (e.g. Smyth and Ruddick, 2010; Toole and Georgi, 1981; Walsh and Ruddick, 1995) to basin scale circulations (e.g. Merryfield et al., 1999; Zhang et al., 1999).

Effective diffusivites can be directly calculated from DNS. The effective diffusivites of heat and salt for 2D salt-fingering have been computed in previous studies (Merryfield and Grinder, 2000; Stern et al., 2001; Yoshida and Nagashima, 2003). The effective diffusivities for 3D sheared, double-diffusive turbulence were first calculated by Kimura and Smyth (2007) for a single initial state.

Our objective here is twofold. First, we test the isotropy assumption for sheared, double-diffusive turbulence, using three-dimensional DNS. Second, we identify effects of anisotropy in estimating effective diffusivities. Effective diffusivities are calculated from the Osborn and Cox (1972) diffusivity model and compared to its direct calculations. Section 2 describes the DNS model, initial conditions, and the turbulent kinetic energy equations we use to diagnose the flow. Section 3 gives an overview of salt sheets. Section 4 discusses the anisotropy of the dissipation-range scale geometry in double-diffusive turbulence. Section 5 discusses the effective diffusivites of momentum, heat, and salt. The conclusions are summarized in section 6.

4.3. Methodology

We employ the three-dimensional incompressible Navier-Stokes equations with the Boussinesq approximation. The resulting velocity field, $\vec{u}(x,y,z,t) = \{u,v,w\}$, equations in a nonrotating, Cartesian coordinate system, $\{x,y,z\}$, are

$$\begin{aligned} \left[\frac{D}{Dt} - \nu\nabla^2\right]\vec{u} &= -\nabla\pi + b\hat{k} + \nu\nabla^2\vec{u} \quad \text{and} \\ \nabla\cdot\vec{u} &= 0. \end{aligned} \tag{4.1}$$

$D/Dt = \partial/\partial t + \vec{u} \cdot \vec{\nabla}$ and ν are the material derivative and kinematic viscosity, respectively. The variable π represents the pressure scaled by the uniform density ρ_0. The total buoyancy is defined as $b = -g(\rho - \rho_0)/\rho_0$, where g is the gravity. The total buoyancy, b, acts in the vertical direction, as indicated by the vertical unit vector $\hat{k}$. We assume that the total buoyancy is the sum of thermal and saline buoyancy components (b_T and b_S), and each component is governed by an advection-diffusion equation:

$$b = b_T + b_S;$$

$$\frac{Db_T}{Dt} = \kappa_T \nabla^2 b_T; \tag{4.2}$$

$$\frac{Db_S}{Dt} = \kappa_S \nabla^2 b_S. \tag{4.3}$$

Thermal and saline diffusivities are denoted by κ_T and κ_S, respectively.

Periodicity intervals in streamwise (x) and spanwise (y) directions are L_x and L_y. Upper and lower boundaries, located at $z = -L_z/2$ and $z = L_z/2$, are impermeable ($w = 0$), stress-free ($\partial u/\partial z = \partial v/\partial z = 0$), and insulating with respect to both heat and salt ($\partial b_T/\partial z = \partial b_S/\partial z = 0$). The variable, L_z represents the vertical domain length.

We initialize the model with a localized-stratified shear flow, which shear and stratification are concentrated at the center of the vertical domain with a thickness of h_0:

$$\frac{u}{\Delta u} = \frac{b_T}{\Delta B_T} = \frac{b_S}{\Delta B_S} = \frac{1}{2} \tanh\left(\frac{2z}{h_0}\right).$$

The constants Δu, ΔB_T, and ΔB_S represent the change in streamwise velocity, thermal buoyancy, and saline buoyancy across the thickness of $h_0 = 0.6\ m$. The change in the total buoyancy is $\Delta B = \Delta B_T + \Delta B_S$. In all the DNS experiments, the initial buoyancy frequency ($\sqrt{\Delta B/h_0}$) is fixed at 1.5×10^{-2} rad s^{-1}, a value typical of the thermohaline staircase east of Barbados (Kunze, 2003).

These constants can be combined with the fluid parameters ν, κ_T, and κ_S to form

non-dimensional parameters, which characterize the flow at $t = 0$:

$$\begin{aligned} Ri &= \frac{\Delta B h_0}{\Delta u^2}; \\ R_\rho &= -\frac{\Delta B_T}{\Delta B_S}; \\ Re &= \frac{\Delta u h_0}{4\nu}; \\ Pr &= \frac{\nu}{\kappa_T}; \\ \tau &= \frac{\kappa_S}{\kappa_T}. \end{aligned}$$

We have done 7 experiments with different Ri and R_ρ (table 4.1). The bulk Richardson number, Ri, measures the relative importance of stratification and shear. If $Ri < 0.25$, the initial flow is subjected to shear instabilities (Hazel, 1972; Howard, 1961; Miles, 1961). Here, we chose high enough Ri to ensure that shear instabilities do not disrupt the growth of double diffusive modes. A typical value of Ri in sheared, salt-fingering-favorable ocean is $Ri \sim 6$ (Kunze, 2003). The density ratio, R_ρ, quantifies the stabilizing effect of thermal to destabilizing effect of saline buoyancy components; salt-fingering grows more rapidly as R_ρ approaches unity. We varied R_ρ between 1.2 and 2, which covers the range of available observational data for comparison (Inoue et al., 2008; St. Laurent and Schmitt, 1999).

The variable Re represents the Reynolds number based on the half-layer thickness and the half change in streamwise velocity. Since ΔB and h_0 are kept constant, the relationship between Re and Ri is $Re = 1354 Ri^{-1/2}$ with $Re = 0$ and $Ri = \infty$ representing the unsheared case. The Prandtl number, Pr, and the diffusivity ratio, τ, describe the difference between molecular diffusivity of momentum, heat, and salt. The Prandtl number was set to 7, which is a typical value for salt water. We have compromised $h_0 = 0.6\ m$, where the observed thickness is $h_0 \sim 2\ m$.

The diffusivity ratio in the ocean is 0.01, i.e., the heat diffuses two orders of magnitude faster than salt. The vast difference in diffusivity requires DNS to resolve a wide range of spatial scales, making it computationally expensive. Accordingly, τ has been

artificially increased to reduce the required computational expenses in previous DNS of salt water (e.g. Gargett et al., 2003; Smyth et al., 2005; Stern et al., 2001). Kimura and Smyth (2007) conducted the first 3D simulation with $\tau = 0.01$ and found that the increase of τ from 0.01 to 0.04 reduced the effective diffusivities by one half. In the cases presented here, we set τ to 0.04.

The fastest-growing salt-sheet wavelength, predicted by linear stability analysis, is $\lambda_{fg} = 2\pi(\nu\kappa_T h_0/\Delta B)^{1/4}$. Our value matches the observed value, $\lambda = 0.032\ m$ (Kunze, 2003). We accommodate four wavelengths of the fastest growing primary instability in the spanwise direction, $L_y = 4\lambda_{fg}$. The vertical domain length, L_z, was chosen so that vertically propagating plumes reach steady equilibrium. We found that L_z equal to three times h_0 was sufficient. L_x was chosen large enough to accommodate subsequent secondary instabilities. After sensitivity tests, we chose $L_x = 28\lambda_{fg}$.

The primary instability was seeded by adding an initial disturbance proportional to the fastest growing mode of linear theory (Smyth and Kimura, 2007). The primary instability in the unsheared case is salt-fingering, cells of rising and sinking fluid. The cells can take a variety of shapes, such as squares, rectangles, and sheets (Proctor and Holyer, 1986; Schmitt, 1994b). We have seeded square salt-fingering for $Ri = \infty$. In the presence of shear, salt-fingering instability is supplanted by salt sheet instability. Salt sheet instability generates alternating planar regions of rising and sinking fluid, aligned parallel to the flow (Linden, 1974). The vertical displacement amplitude is set to $0.02h$, and a random noise was added to the initial velocity field with an amplitude of $1 \times 10^{-2} h\sigma_L$ to seed secondary instabilities. The variable, σ_L indicates the growth rate of the linear normal mode described by Smyth and Kimura (2007).

The numerical code used to solve (4.1) - (4.3) is described by Winters et al. (2004). The code uses Fourier pseudospectral discretization in all three directions, and time integration is done using a third-order Adams-Bashforth operator. A time step is determined

by a Courant-Friedrichs-Lewy (CFL) stability condition. The CFL number is maintained below 0.21 for DNS experiments presented here. The code was modified by Smyth et al. (2005) to accommodate a second active scalar, which is resolved on a fine grid with spacing equal to one half the spacing used to resolve the other fields. The fine grid is used to resolve salinity. The fine grid spacing is equal to $0.15\lambda_{fg}\sqrt{\tau}$ in all three directions, as suggested by Stern et al. (2001).

	DNS1	DNS2	DNS3	DNS4	DNS5	DNS6	DNS7
Ri	0.5	2	6	20	∞	6	6
R_ρ	1.6	1.6	1.6	1.6	1.6	1.2	2.0
Pr	7	7	7	7	7	7	7
Re	1914	957	553	302	0	553	553
τ	0.04	0.04	0.04	0.04	0.04	0.04	0.04
λ_{fg}[m]	0.031	0.031	0.031	0.031	0.044	0.031	0.032
L_x[m]	0.9	0.9	0.9	0.9	1.2	0.9	0.9
L_y[m]	0.12	0.12	0.12	0.12	0.18	0.12	0.12
L_z[m]	1.8	1.8	1.8	1.8	1.8	1.8	1.8
nx	1024	1024	1024	1024	1024	1024	1024
ny	144	144	144	144	144	144	144
nz	2048	2048	2048	2048	1538	2048	2048

TABLE 4.1: Relevant parameters used in our DNS experiments. The wave number of the fastest growing salt-fingering instability is determined by the magnitude of wave number, k^2+l^2, where k and l represent the streamwise and spanwise wave numbers. In the case of salt sheets (all cases except DNS5), there is not streamwise dependence (k=0), where the salt-fingering case (DNS5) has $k = l$. In our DNS experiments, $k^2 + l^2$ is kept constant.

4.3.1 Diagnostic equations

For analyzing the flow, we need statistical quantities to characterize double-diffusive turbulence. We utilize turbulent kinetic energy, thermal buoyancy variance, and saline buoyancy variance equations. The instantaneous state of the velocity fields, scaled pressure, and buoyancy components can be written as a background plus a fluctuation part:

$$\begin{aligned}
\vec{u}(x,y,z,t) &= \overline{\vec{u}}(z,t) + \vec{u'}(x,y,z,t);\\
\pi(x,y,z,t) &= \overline{\pi}(z,t) + \pi'(x,y,z,t);\\
b_T(x,y,z,t) &= \overline{b_T}(z,t) + b'_T(x,y,z,t);\\
b_S(x,y,z,t) &= \overline{b_S}(z,t) + b'_S(x,y,z,t).
\end{aligned}$$

The overbars indicate the average over horizontal directions. Turbulent kinetic energy, thermal buoyancy and saline buoyancy variances can be defined as,

$$K_e(t) = \frac{1}{2}\langle\overline{\vec{u'}\cdot\vec{u'}}\rangle_z; \quad T_e(t) = \frac{1}{2}\langle\overline{{b'_T}^2}\rangle_z;$$

$$S_e(t) = \frac{1}{2}\langle\overline{{b'_S}^2}\rangle_z.$$

Angle brackets denote an average over z, specified by the subscript. The time rate of change of turbulent kinetic energy, K_e, is obtained by taking the scalar product of $\vec{u}$ to (4.1) and collecting fluctuation terms. The resulting equation becomes

$$\frac{\partial K_e}{\partial t} = -\langle\overline{u'w'}\frac{\partial\overline{u}}{\partial z}\rangle_z + \langle\overline{w'b'}\rangle_z - \langle\overline{\epsilon}\rangle_z, \tag{4.4}$$

where

$$\epsilon = 2\nu e_{ij}e_{ij}; \quad e_{ij} = \frac{1}{2}\left(\frac{\partial u'_i}{\partial x_j} + \frac{\partial u'_j}{\partial x_i}\right).$$

The right hand side of the (4.4) represents the shear production, buoyancy production, and turbulent kinetic energy dissipation rate, respectively. A sum of advective, pressure-driven, and viscous fluxes vanish after the spatial average is taken.

The time rate of change of thermal buoyancy variance, T_e, and saline buoyancy variance, S_e, are obtained by taking the scalar product of b_T and b_S to equation (4.2) and (4.3) and collecting the fluctuation parts. The resulting equations become

$$\frac{\partial T_e}{\partial t} = -\langle \overline{w' b'_T} \frac{\partial \overline{b_T}}{\partial z} \rangle_z - \frac{1}{2} \langle \overline{\chi_T} \rangle_z \tag{4.5}$$

and

$$\frac{\partial S_e}{\partial t} = -\langle \overline{w' b'_S} \frac{\partial \overline{b_S}}{\partial z} \rangle_z - \frac{1}{2} \langle \overline{\chi_S} \rangle_z. \tag{4.6}$$

Here, χ_T and χ_S represent the dissipation rates of thermal and saline buoyancy variances, $\chi_T = 2\kappa_T |\nabla b'_T|^2$ and $\chi_S = 2\kappa_S |\nabla b'_S|^2$. In the steady limit, (4.4) and (4.5) are equivalent to the production-dissipation balances model for turbulent kinetic energy (Osborn, 1980) and thermal variance (Osborn and Cox, 1972).

4.4. Flow overview

Figure 4.1 shows the salinity buoyancy field of $Ri = 6, R_\rho = 1.6$ at selected times. Figure 4.1a shows the salt sheet instability; the planar regions of vertical motions are oriented parallel to the background shear. Rising and sinking fluid are shown in green and blue, respectively. The computational domain accommodates four salt sheets.

When the salts sheets reach the edges of the transition layer (indicated by purple and red), the salt sheets start to undulate in the spanwise direction (figure 4.1b). At the same time, the salt sheets develop streamwise dependence at the edges and the center of the transitional layer. At the edges of the transitional layer, the streamwise dependence appears as ripples. At the center of the transitional layer, the streamwise dependence is tilted laminae, which resembles shadowgraph images of optical microstructure presented in Kunze (1990) and St. Laurent and Schmitt (1999). After the salt sheets have disrupted, the flow evolves into double-diffusive turbulence (figure 4.1c).

(a) $\sigma_L t = 3.1$ **(b)** $\sigma_L t = 5$ **(c)** $\sigma_L t = 8.7$

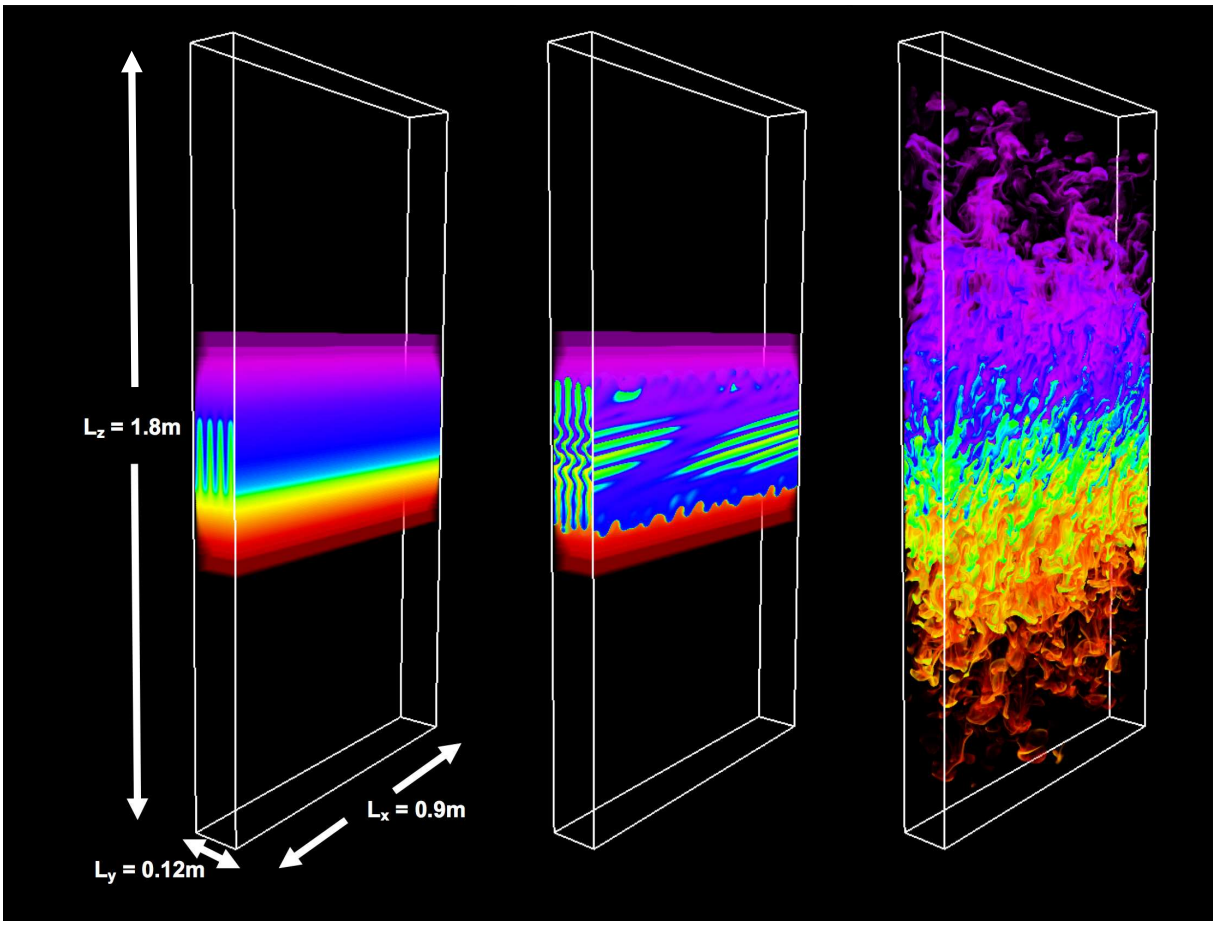

FIGURE 4.1: Evolution of salinity buoyancy field for $Ri = 6, R_\rho = 1.6$ at the transitional layer with respect to the scaled time $\sigma_L t$. The variable, σ_L indicates the growth rate of the linear normal mode described by Smyth and Kimura (2007). The transitional layer occupies one third of the domain height. Homogenous regions above and below the transitional layer are rendered transparent. Inside the transitional layer, the lowest ($-7.15 \times 10^{-5} m^2 s^{-1}$) and highest ($7.15 \times 10^{-5} m^2 s^{-1}$) salinity buoyancy are indicated by purple and red, respectively.

Flow can be characterized by the instantaneous exponential growth rate for the velocity perturbations, $\vec{u'}$. Each component of the instantaneous exponential growth rate is defined as

$$\sigma_u = \frac{1}{2}\frac{d}{dt}\ln\left(\langle\overline{u'^2}\rangle_z\right); \tag{4.7}$$

$$\sigma_v = \frac{1}{2}\frac{d}{dt}\ln\left(\langle\overline{v'^2}\rangle_z\right); \tag{4.8}$$

$$\sigma_w = \frac{1}{2}\frac{d}{dt}\ln\left(\langle\overline{w'^2}\rangle_z\right). \tag{4.9}$$

Figure 4.2 shows the evolution of the instantaneous exponential growth rates with respect to physical time and the scaled time. At the beginning, the partial growth rates experience the initial adjustment from the random noise seeded on the velocity field. Subsequently, all three components of the partial growth rate adjust to the same rate and grow in accordance with the linear normal mode of primary instability (figure 4.2a, 4.2b, and 4.2c). The primary instability for figure 4.2a and 4.2c is salt sheets instability described by Linden (1974) and Smyth and Kimura (2007). The primary instability for figure 4.2b is salt fingering instability.

As the salt sheet grows, the faster diffusion of heat relative to salt create blobs of fluid at the edges of salt sheets (figure 4.1a and 4.1b). In salt sheets, the vertical motions of these blobs displace the fluid in spanwise direction first, indicated by the increase of σ_v followed by the increase in σ_u (figure 4.2a and 4.2c). In the case of salt fingering (figure 4.2b), these blobs displace the fluid in spanwise and streamwise directions, indicated by the simultaneous increase in σ_v and σ_u. The exponential increase of σ_v and σ_u shows the super exponential growth of the secondary instability of salt fingers described by Stern and Simeonov (2005).

By $\sigma_L t = 6$, the secondary instability settles down in all the cases. The fluctuation of the instantaneous exponential growth rates become within $\pm 10^{-3} s^{-1}$ after $\sigma_L t = 8$; the flow has reached a quasi-steady state.

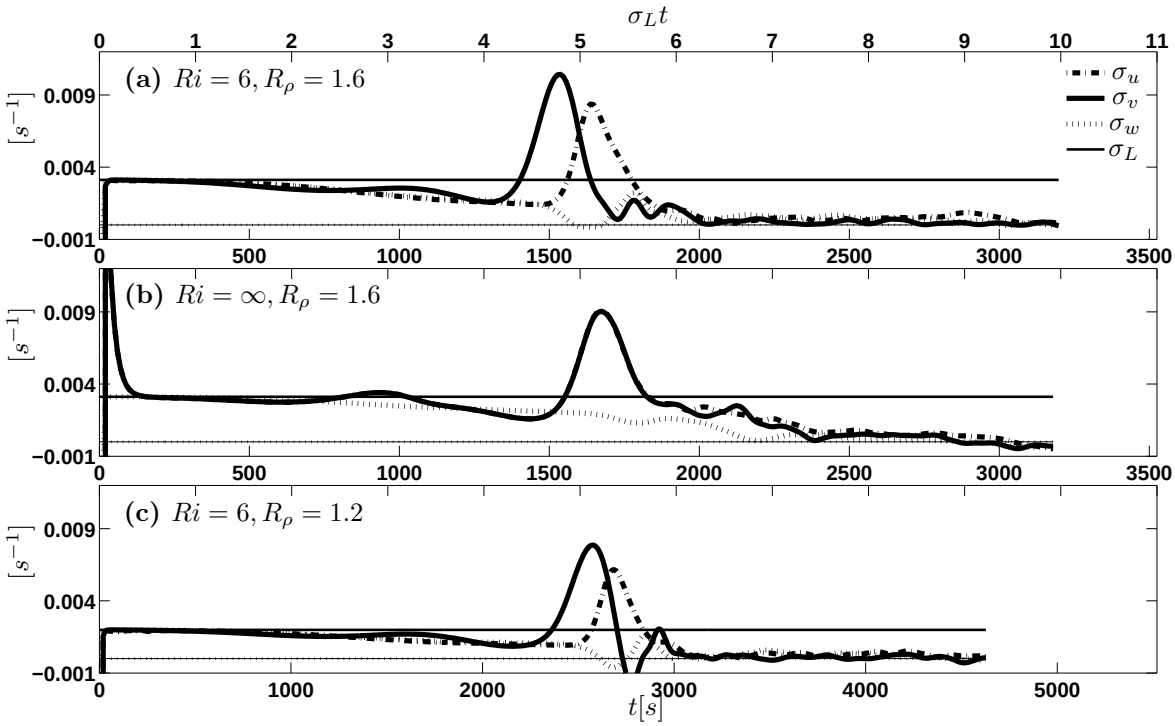

FIGURE 4.2: Evolution of partial growth rates for selected cases. (a) our base case. (b) the highest Ri, which initialized by salt-fingering instability. (c) the lowest R_ρ. The upper axes indicate the time, scaled by the linear growth rate, where the bottom axes show the time in dimensional unit. A thin dashed line indicates a steady limit of the zero growth rate.

4.4.1 Evolution of the turbulent kinetic energy dissipation rate

The evolution of the turbulent kinetic energy dissipation rate can be characterized from the probability density function (pdf). The $log(\epsilon)$ ranged from -23 to -7; the data was divided into 161 bins with an increment of $log(\epsilon) = 0.1$.

The evolution of the pdf shows two distinct peaks (figure 4.3). When the salt sheets dominate the flow ($\sigma_L t = 3.1$), the pdf peaks at $\epsilon = 10^{-17} W kg^{-1}$. Figure 4.4a shows that the region of $\epsilon < 10^{-15} W kg^{-1}$ is located at the outside of the transitional layer and occupies 84% of the total volume. In the transitional layer, the shearing of planar regions of the vertical motions generates ϵ near $10^{-9} W kg^{-1}$, which corresponds to the jagged distribution seen near $\epsilon = 10^{-9} W kg^{-1}$ in figure 4.3a. These high values dominate the volume average.

At $\sigma_L t = 5$, regions of shearing between adjacent salt sheets have increased, spreading the regions with ϵ near $10^{-9} W kg^{-1}$ (figure 4.4b), and the peak of the pdf has started to shift to the higher values (figure 4.3b). Finally, the filaments of $\epsilon \approx 10^{-9} W kg^{-1}$ occupies the domain (figure 4.4c). The shape of the pdf becomes approximately a log-normal distribution (figure 4.3c). Figure 4.3c corresponds well with histograms of $log(\epsilon)$ from observations in NATRE site (figure 7a of St. Laurent and Schmitt (1999)).

In the next section, we identify the dissipation-range scale geometry of double-diffusive turbulence by approximations of dissipation rates, assuming isotropy.

4.5. Isotropy and dissipation rates

The validity of isotropy can be diagnosed by buoyancy Reynolds number, $Re_b = \langle \overline{\epsilon} \rangle_z / \nu N^2$. Re_b can be thought as a ratio of lengthscales $Re_b = (L_o/L_k)^{4/3}$. L_o and L_k represent Ozmidov (Ozmidov, 1965) and Kolmogorov (Kolmogorov, 1941) lengthscales,

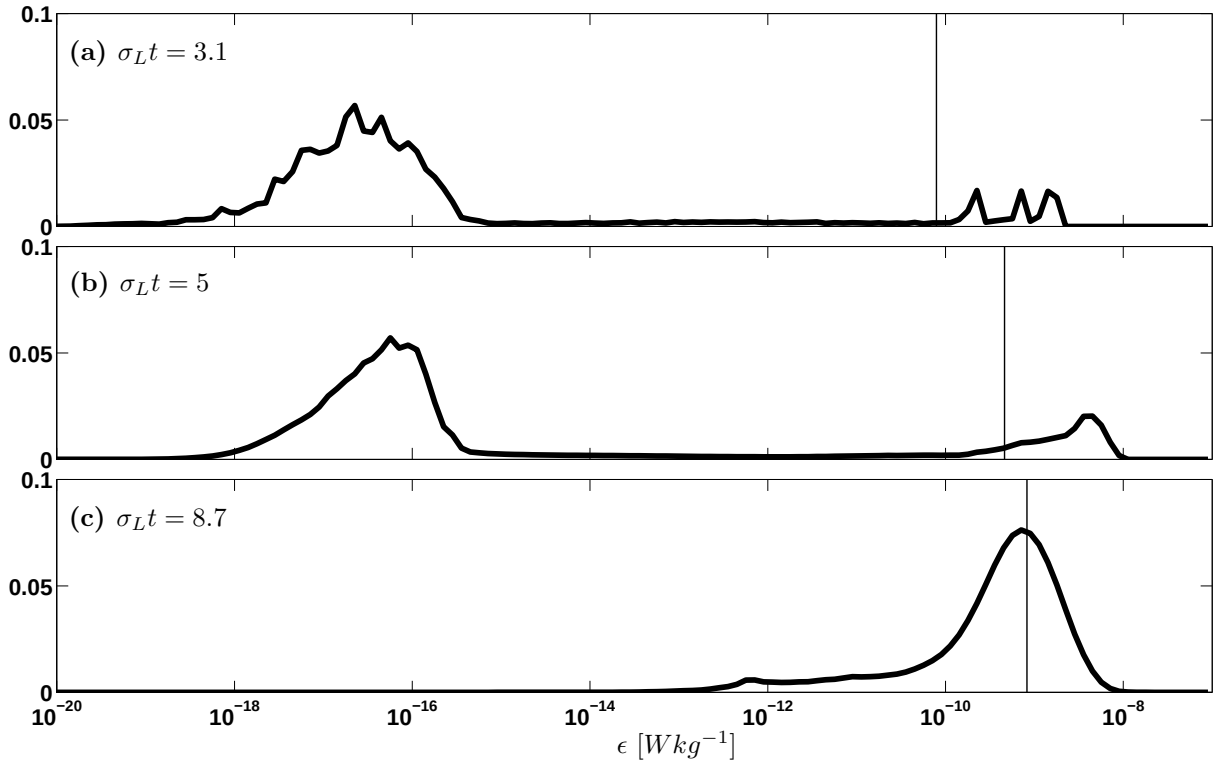

FIGURE 4.3: Temporal evolution of the distribution of the turbulent kinetic energy dissipation for DNS3. A solid line on each panel indicates the volume averaged turbulent kinetic energy dissipation.

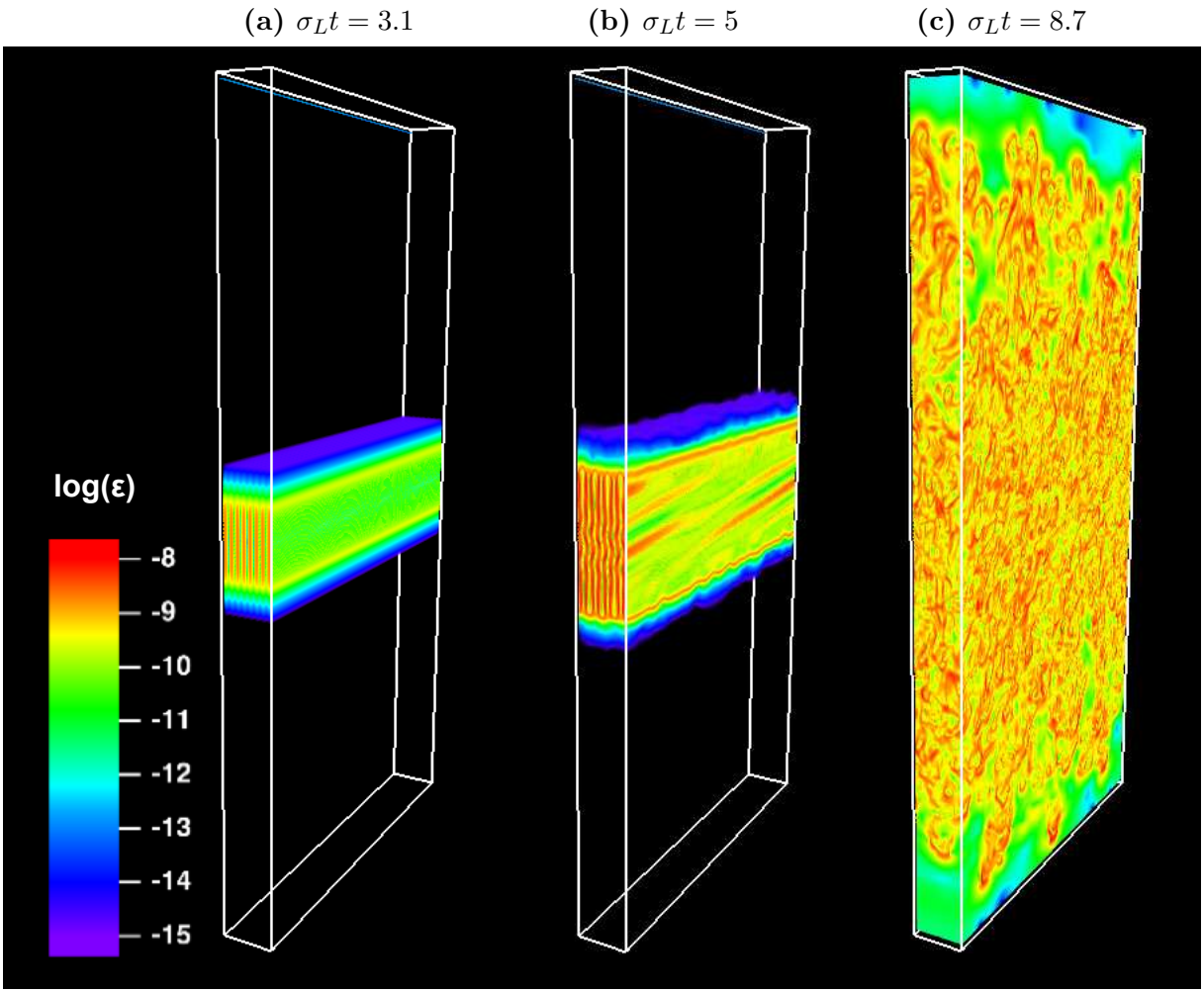

FIGURE 4.4: Temporal evolution of ϵ in logarithmic scale for$Ri = 6, R_\rho = 1.6$.

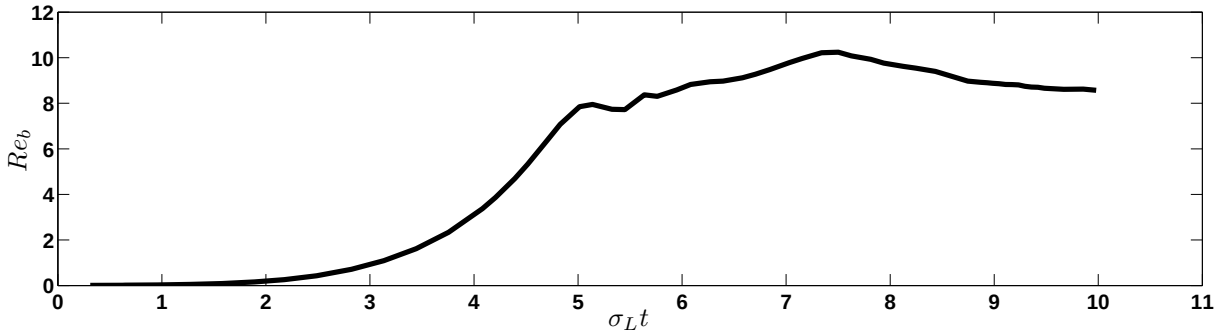

FIGURE 4.5: Evolution of volumed averaged Re_b for $Ri = 6, R_\rho = 1.6$.

respectively:

$$L_o = \left(\langle\overline{\epsilon}\rangle_z / N^3\right)^{1/2}; \quad L_k = (\nu^3/\langle\overline{\epsilon}\rangle_z)^{1/4}.$$

L_o represents the length of the largest possible overturns, where L_k is the smallest length-scale in which viscosity does not deform eddies.

As Re_b increases, the dissipation-range scale becomes separated apart from the energy-containing scale. Gargett et al. (1984) concluded from observations that $\overline{\epsilon}$ can be accurately estimated from a single term when $Re_b > 200$. Itsweire et al. (1993) found that isotropic assumption is not accurate for $Re_b < 10^2$ using DNS with uniform stratified-shear layer. In a localized shear layer, Smyth and Moum (2000) showed that the isotropy assumption can be accurate for $Re_b > 10^2$, using DNS.

In salt-fingering system, laboratory experiments showed that the finger structures can exist for $Re_b \sim O(10)$ with $R_\rho < 2$ (McDougall and Taylor, 1984). Oceanic observations of salt-fingering system suggest that Re_b is $O(10)$ (Inoue et al., 2008; St. Laurent and Schmitt, 1999). Figure 4.5 shows that Re_b from our simulation rapidly increases until salt sheets start to break up ($\sigma_L t \approx 5$) and reaches a maximum value of $Re_b = 10.8$ at $\sigma_L t = 8$. After $\sigma_L t > 8$, Re_b becomes quasi-steady $Re_b \approx 10$. To represent R_ρ dependence, we average Re_b over $\sigma_L t > 8$. Figure 4.6 shows that Re_b from our simulation is in the same range as observed Re_b. Inoue et al. (2008) sorted buoyancy Reynolds number with respect to Ri and R_ρ. Their R_ρ-binned mean Ri lies between 3 and 7 with larger values for $R_\rho > 1.4$, while Ri-binned mean R_ρ is nearly constant around 1.65.

Because Re_b in salt-fingering system is lower than known thresholds for the isotropy assumption to be valid, it is plausible that the isotropy assumption may affect the estimation of dissipation rates. The Re_b from DNS is comparable to the observed Re_b; therefore, we may extrapolate our results to quantify the bias in estimating dissipation rates in the interpretation of observations.

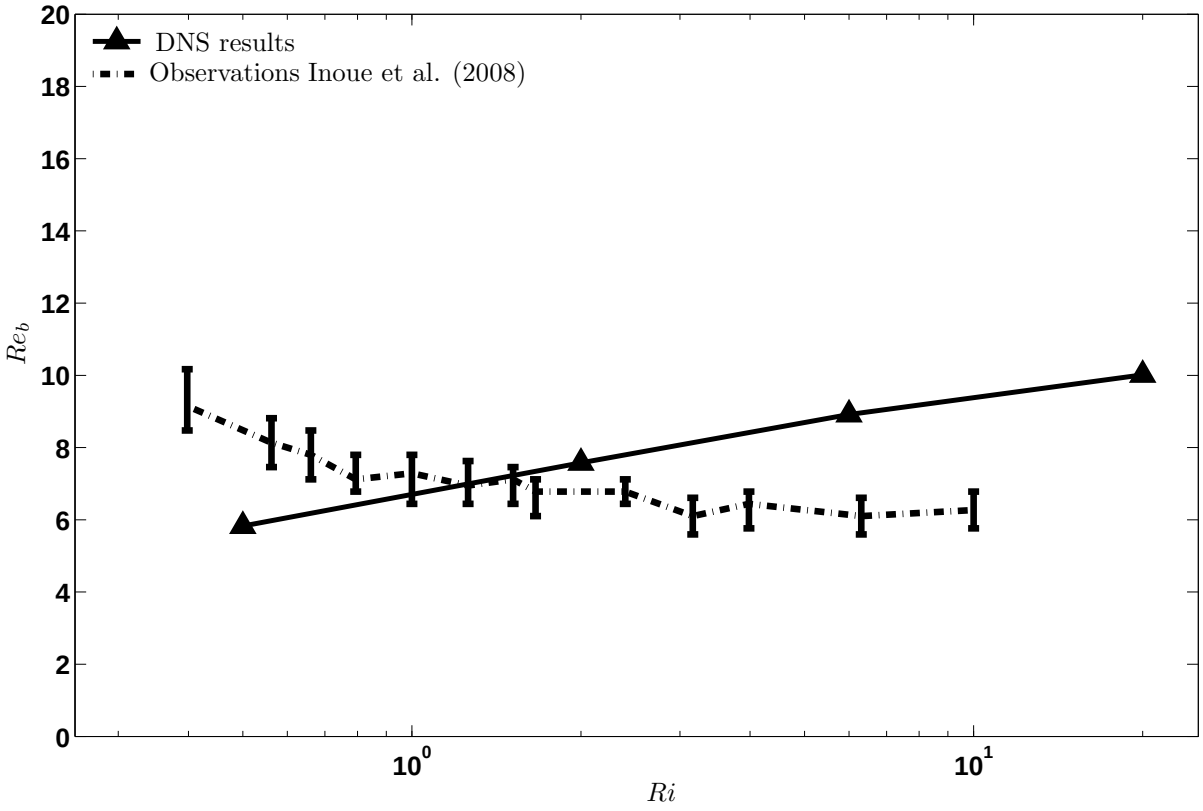

FIGURE 4.6: Re_b with respect to Ri for $R_\rho = 1.6$ from our DNS experiments with observations from Inoue et al. (2008). Mean R_ρ is nearly constant around 1.65 for Inoue et al. (2008). The Re_b from our DNS reaches to $Re_b = 16.8$ at $Ri = \infty$.

4.5.1 Components of χ_S and χ_T

In isotropic turbulence, the saline and thermal variance dissipation rates can be expressed in three different forms as

$$\overline{\chi_S} = 6\kappa_S \overline{\left(\frac{\partial b'_S}{\partial x_i}\right)^2} \quad \text{and} \tag{4.10}$$

$$\overline{\chi_T} = 6\kappa_T \overline{\left(\frac{\partial b'_T}{\partial x_i}\right)^2} \tag{4.11}$$

with no summation over i. Each of three different forms takes exactly the same value in isotropic turbulence.

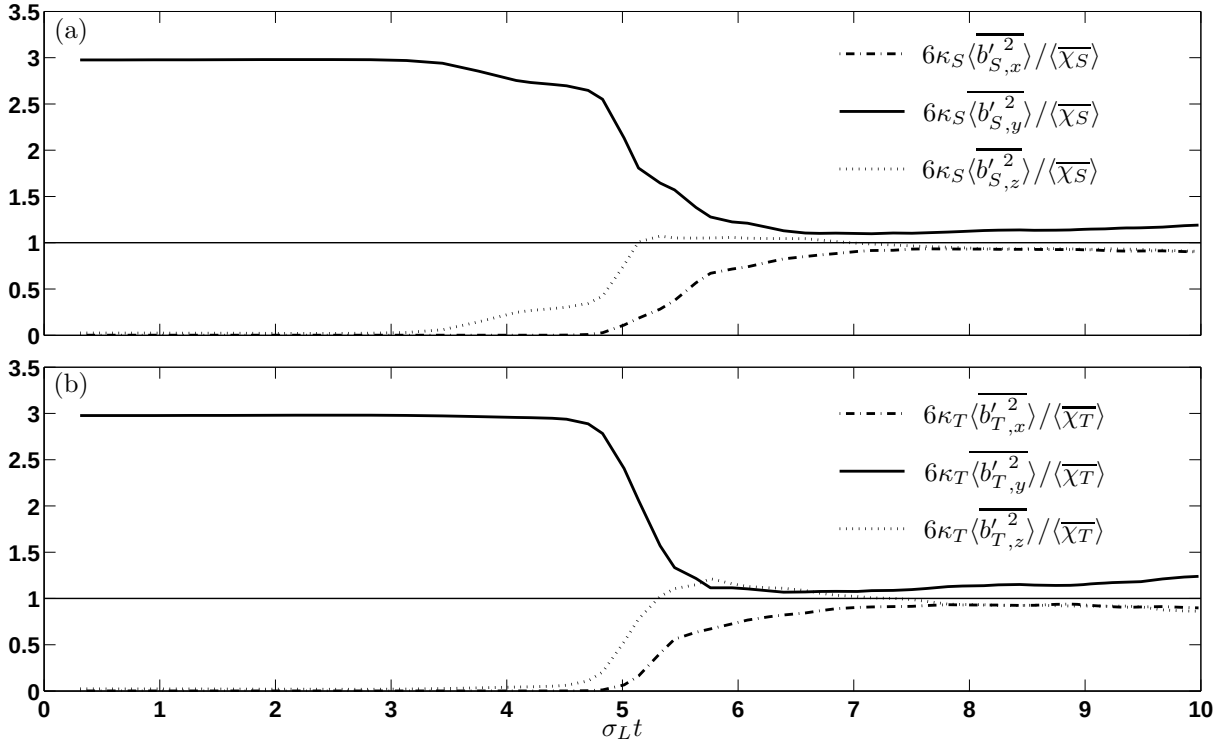

FIGURE 4.7: (a) Evolution of saline variance dissipation rates from derivatives of squared perturbations averaged over $-h_0 < z < h_0$ as a fraction of its true value. (b) Evolution of thermal variance dissipation rates from derivatives of squared perturbations averaged over $-h_0 < z < h_0$ as a fraction of its true value.

Salt-fingering system having $Re_b \sim O(10)$, observations and numerical simulations support the thermal buoyancy field being nearly isotropic. Two-dimensional numerical

simulations of Shen (1995) showed that the thermal spectral variance is distributed approximately equally in both vertical and horizontal wavenumbers. Lueck (1987) found that the magnitude of the vertical thermal buoyancy gradient was similar to the horizontal gradient in a thermocline staircase east of Barbados. Since the measurements were taken at the sites with $Ri \sim 10$ and never less than unity, Lueck (1987) argued that the isotropic structure is not likely the result of shear-driven turbulence. Shadowgraph images of salt-fingering showed coherent tilted laminae (Kunze, 1990; Schmitt et al., 1987; St. Laurent and Schmitt, 1999). Shadowgraph images tend to emphasize the smallest scales that are mainly influenced by salinity (Kunze, 1990). St. Laurent and Schmitt (1999) aruged that the shadowgraph images were biased by anisotropic salinity structures.

Figure 4.7 shows that saline and thermal buoyancy fields are anisotropic at the beginning but becomes nearly isotropic as the flow evolves into turbulent regime ($\sigma_L t > 8$). Each of three different forms in (4.10) and (4.11) is normalized by its true values $\langle\overline{\chi_S}\rangle$ and $\langle\overline{\chi_T}\rangle$ to characterize isotropy characteristics. The angle brackets indicate the average over the transitional layer $-h_0 < z < h_0$. Figure 4.7a and 4.7b show that signatures of salt sheets decreases on both saline and thermal buoyancy fields. In the linear regime ($0 < \sigma_L t < 4$), all the salinity and thermal variance dissipation rates comes from the spanwise derivatives (indicated by solid lines in figure 4.7a and 4.7b), which is consistent with the motion of salt sheets.

With the onset of secondary instability, the contribution from the spanwise contribution decreases while contributions from streamwise and vertical derivatives increase. These ratios become quasi-steady in the turbulent regime ($\sigma_L t > 8$), by which time the field is nearly isotropic.

Figure 4.8 shows the average of these ratios in the thermal buoyancy field over $\sigma_L t > 8$ to represent Ri and R_ρ dependence of the flow geometry of double-diffusive turbulence. Figure 4.8a shows that salt-fingering from the linear regime is present in the

estimation of $\langle\overline{\chi_T}\rangle$. In the case of $Ri = \infty$, the contribution from horizontal derivatives are approximately in balance $\left(\langle\overline{b'^2_{T,x}}\rangle \approx \langle\overline{b'^2_{T,y}}\rangle\right)$, indicating that the thermal buoyancy gradient is statistically axisymmetric about the vertical. As Ri decreases, the signature of salt sheets instability gets stronger; the contribution from $b'^2_{T,y}$ increases, while the contribution from $b'^2_{T,x}$ decreases with decreasing Ri. The contribution from $b'^2_{T,z}$ to $\langle\overline{\chi_T}\rangle$ increases with decreasing Ri, resembling the characteristics of shear-driven turbulence described by Smyth and Moum (2000).

As R_ρ increases, the characteristics of salt sheets dominate (figure 4.8b), i.e., the contribution from $b'^2_{T,y}$ increases with increasing R_ρ, while the contribution from $b'^2_{T,x}$ decreases. In the case of $R_\rho = 1.2$, the approximations associated with horizontal derivatives almost resembles the salt-fingering case $\left(\langle\overline{b'^2_{T,x}}\rangle \approx \langle\overline{b'^2_{T,y}}\rangle\right)$. As R_ρ decreases, the thermal buoyancy fields become more isotropic. The same trend has been observed in laboratory experiments of Taylor (1992).

4.5.2 Geometry of the small-scale velocity field

An alternative approach to understand the dissipation-range scale geometry is via enstrophy budget. Enstrophy is defined as

$$Z = \frac{\langle\overline{\vec{\omega}\cdot\vec{\omega}}\rangle}{2}$$

where $\vec{\omega} = \{w'_y - v'_z, u'_z - w'_x, v'_x - u'_y\}$ are the vorticity vector. In the isotropic turbulence, each of three vorticity components has the same magnitude; therefore, Z can be expressed by one of its magnitudes as

$$\eta = 3Z^{(x)} = 3Z^{(y)} = 3Z^{(z)},$$

where $Z^x = \langle\overline{(w'_y - v'_z)^2}\rangle/2$, $Z^y = \langle\overline{(u'_z - w'_x)^2}\rangle/2$, and $Z^z = \langle\overline{(v'_x - u'_y)^2}\rangle/2$.

Figure 4.9 shows that the velocity gradients do not become isotropic. The enstrophy budget is dominated by $Z^{(x)}$ in the linear regime ($0 < \sigma_L t < 5$). The increase in the

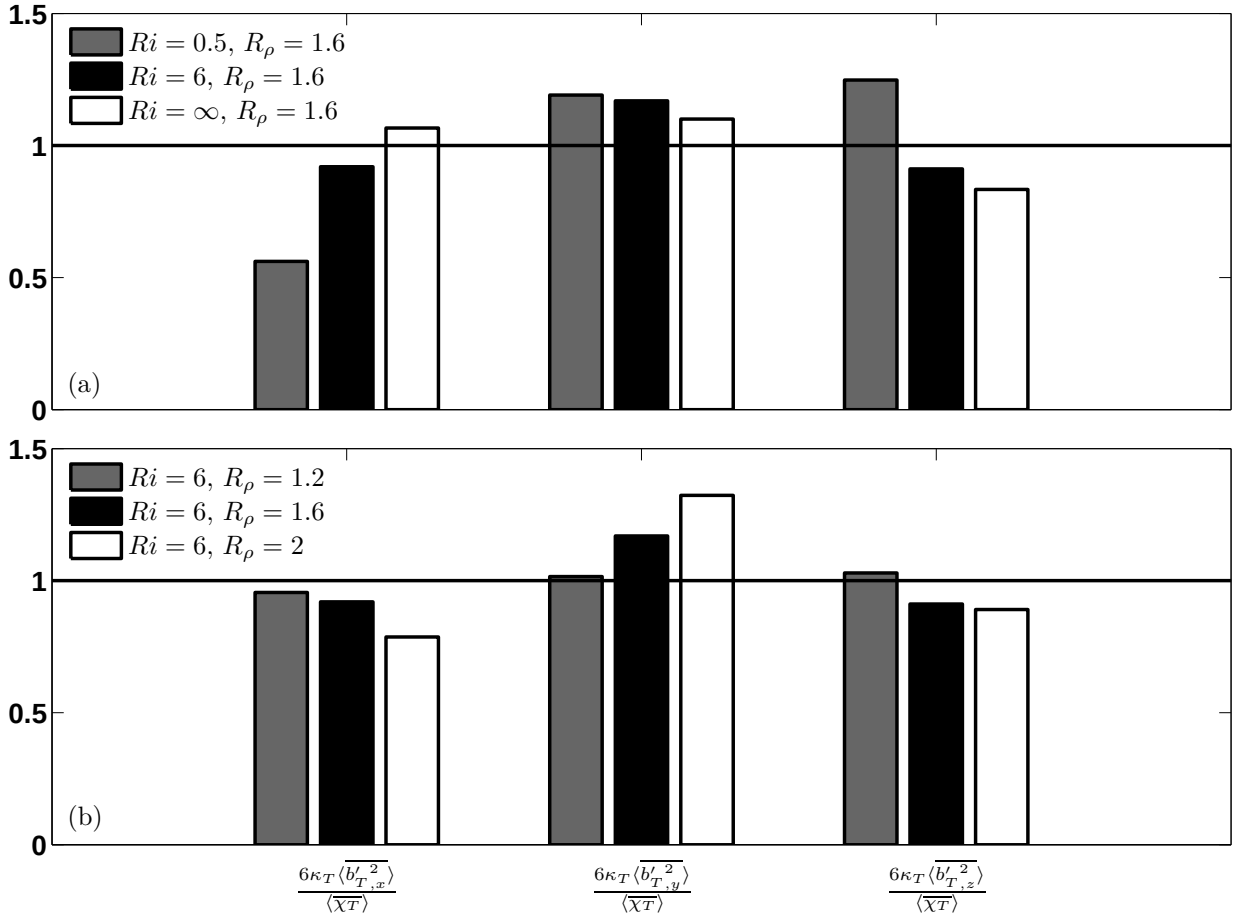

FIGURE 4.8: Approximations of the thermal variances dissipation from derivatives of squared perturbations as a fraction of its true values for (a) different Ri and (b) different R_ρ. Each ratio is averaged for $\sigma_L t > 8$ to represent the geometry in the turbulent state. A solid line indicates the ratio for isotropic flow.

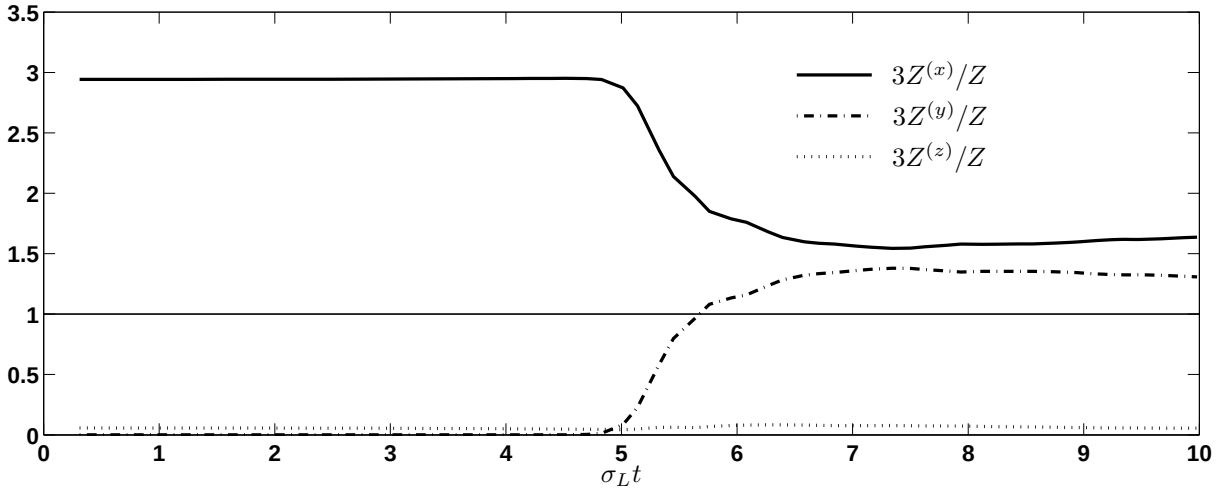

FIGURE 4.9: These ratios are unity for the isotropic turbulence indicated by the solid lines.

contribution from $Z^{(y)}$ ($\sigma_L t \approx 5.5$) disrupts the salt sheets as the flow become three-dimensional. At $\sigma_L t \approx 7$, the ratios of the horizontal vorticities become quasi-steady with values $3Z^{(x)}/Z \approx 1.6$ and $3Z^{(y)}/Z \approx 1.4$, while $3Z^{(x)}/Z$ is nearly zero. The steady value for $3Z^{(x)}/Z$ is slightly larger than that of $3Z^{(y)}/Z$, reflecting the geometry of salt sheets.

In summary, the perturbation velocity gradients does not become isotropic in the turbulent regime, in contrast to the thermal and saline buoyancy gradients. This will affect the estimation of ϵ in the double diffusive turbulence, as we discuss in the next section.

4.5.3 Components of ϵ

In the isotropic turbulence, $\langle\overline{\epsilon}\rangle$ can take any one of the following nine expressions:

$$\langle\overline{\epsilon}\rangle = \frac{15\nu}{2-\delta_{i,j}}\left\langle\overline{\left(\frac{\partial u_i'}{\partial x_j}\right)^2}\right\rangle, \tag{4.12}$$

with no summation over i and j (Taylor, 1935). The variable, $\delta_{i,j}$, represents the Kronecker delta function. In general, these expressions are unequal, and their differences reflect the degree of anisotropy in the dissipation-range scale geometry.

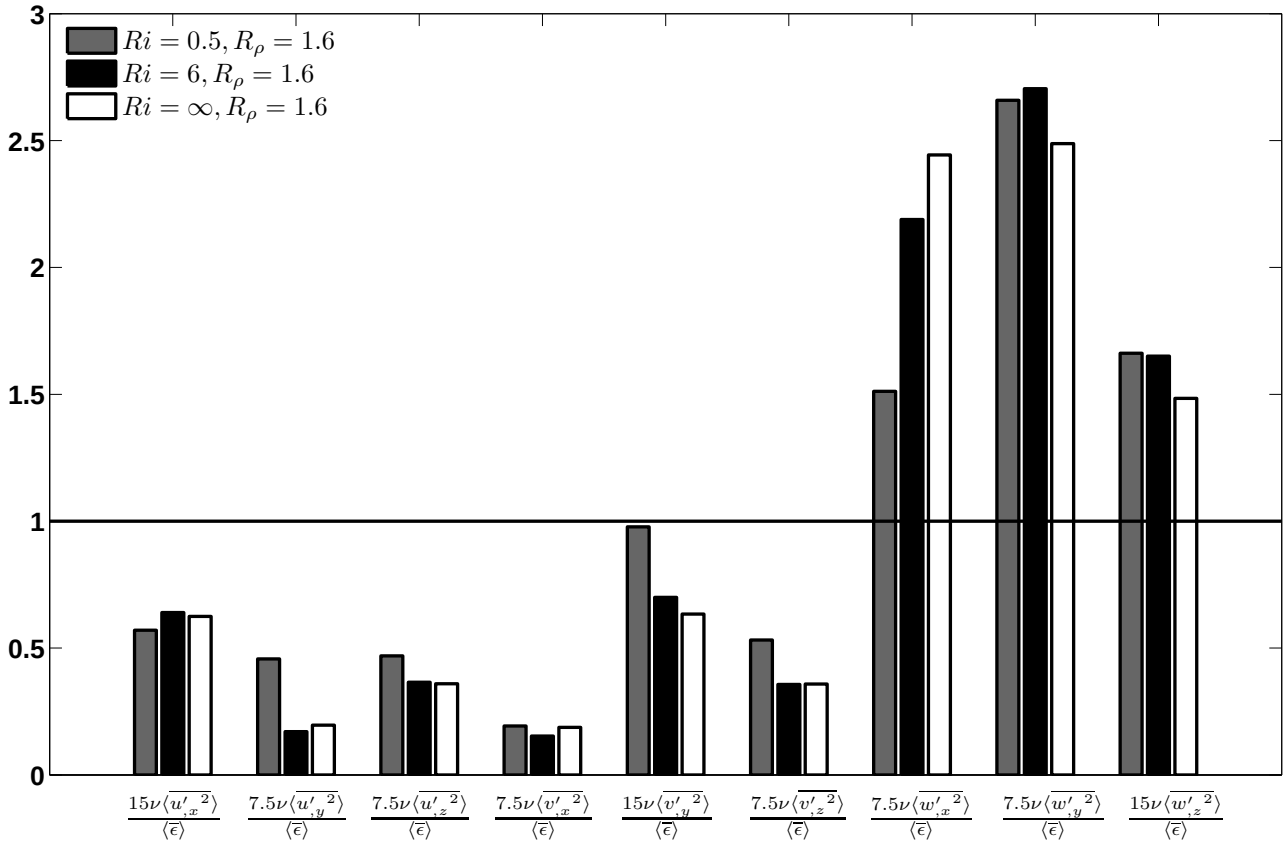

FIGURE 4.10: Approximations of $\langle\overline{\epsilon}\rangle$ from each of the squared perturbation velocity derivatives as a fraction of its value, $\langle\overline{\epsilon}\rangle$ for different Ri. Each ratio is averaged for $\sigma_L t > 8$ to represent the geometry in the turbulent state. The solid line indicates the ratio for isotropic flow.

Nine components of the approximations in (4.12) were averaged over $\sigma_L t > 8$ and normalized by its true value to quantify Ri and R_ρ dependence. As shown in figure 4.10, the approximations involving the vertical velocity overestimate $\langle\overline{\epsilon}\rangle$, whereas those involving horizontal velocities underestimate $\langle\overline{\epsilon}\rangle$. This is consistent with the dominance of vertical motions in double-diffusive turbulence. In the absence of shear (white bars on figure 4.10), the contribution from ${w'_{,x}}^2$ and ${w'_{,y}}^2$ are the largest, which is consistent with the axisymmetry of salt-fingering about the vertical. In the sheared cases (black and grey bars), the contribution from ${w'_{,y}}^2$ is the largest, consistent with the geometry of salt sheets (figure 4.10).

In both sheared and unsheared cases, the second largest contribution comes from ${w'_{,z}}^2$. This is the normal strain rate in the vertical direction, which acts to squeeze the fluid vertically at the tips of rising and sinking plumes. The vertically squeezed fluid at the tips is balanced by the normal strains in horizontal directions $\left(\langle\overline{{w'_{,z}}^2}\rangle \approx \langle\overline{{u'_{,x}}^2}\rangle + \langle\overline{{v'_{,y}}^2}\rangle\right)$. Because of the difference in geometry between sheared and unsheared cases, the contributions from ${u'_{,x}}^2$ and ${v'_{,y}}^2$ to balance ${w'_{,z}}^2$ are different. In the unsheared case, the vertically squeezed fluid at the edges of plumes is displaced equally in the streamwise and spanwise directions $\left(\langle\overline{{u'_{,x}}^2}\rangle \approx \langle\overline{{v'_{,y}}^2}\rangle\right)$, resembling salt-fingering. In contrast, the geometry of the sheared case displaces more fluid in spanwise direction $\left(\langle\overline{{u'_{,x}}^2}\rangle < \langle\overline{{v'_{,y}}^2}\rangle\right)$.

The approximations using horizontal shear strain rates also show the influence of the linear instabilities. The balances shown in the unsheard case, $\langle\overline{{u'_{,y}}^2}\rangle \approx \langle\overline{{v'_{,x}}^2}\rangle$, $\langle\overline{{u'_{,z}}^2}\rangle \approx \langle\overline{{v'_{,z}}^2}\rangle$, and $\langle\overline{{u'_{,x}}^2}\rangle \approx \langle\overline{{v'_{,y}}^2}\rangle$, indicate axisymmetry about the vertical. As Ri decreases, contributions from ${u'_{,z}}^2$ and ${v'_{,z}}^2$ increase. This indicates that the flow is approaching shear-driven turbulence described by Itsweire et al. (1993) and Smyth and Moum (2000). Flow geometry in the linear regime dictates the velocity gradients in dissipation-range scale.

4.5.4 Estimations of ϵ and χ_T from vertical profilers

Observational estimates of dissipation rates are often based on data from vertical profilers, which measure the vertical change of velocities, temperature, and salinity. The oceanic values of $\langle\overline{\epsilon}\rangle$ and $\langle\overline{\chi_T}\rangle$ can be estimated by $\langle\overline{\epsilon^z}\rangle$ and $\langle\overline{\chi_T^z}\rangle$:

$$\langle\overline{\epsilon^z}\rangle = \frac{15\nu}{4}\left(\left\langle\overline{\left(\frac{\partial u'}{\partial z}\right)^2}\right\rangle + \left\langle\overline{\left(\frac{\partial v'}{\partial z}\right)^2}\right\rangle\right); \tag{4.13}$$

$$\langle\overline{\chi_T^z}\rangle = 6\kappa_T\left\langle\overline{\left(\frac{\partial b_T'}{\partial z}\right)^2}\right\rangle. \tag{4.14}$$

For isotropic flows, these approximations are exact, i.e. $\langle\overline{\epsilon}\rangle = \langle\overline{\epsilon^z}\rangle$ and $\langle\overline{\chi_T}\rangle = \langle\overline{\chi_T^z}\rangle$.

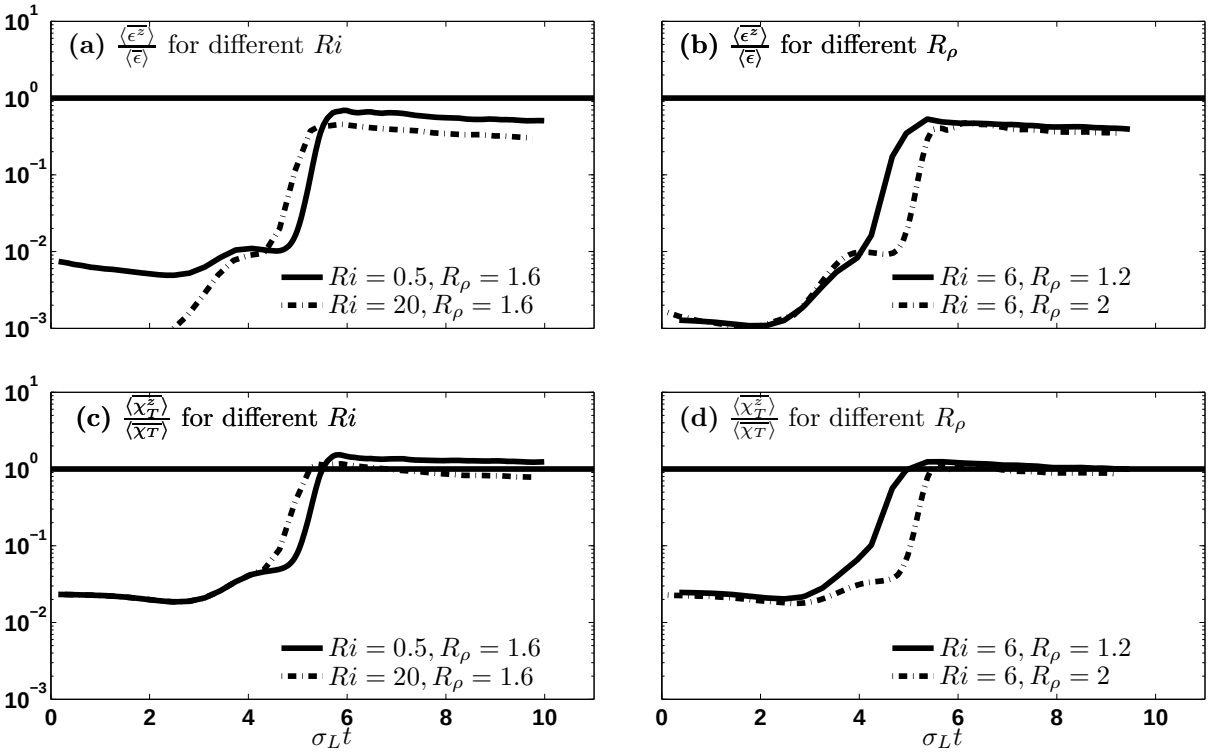

FIGURE 4.11: Approximations of $\langle\overline{\epsilon}\rangle$ as a fraction of its true value with respect to $\sigma_L t$ for (a) different Richardson number Ri and (b) different density ratio R_ρ. Approximations of $\langle\overline{\chi_T}\rangle$ as a fraction of its true value with respect to $\sigma_L t$ for (c) different Richardson number Ri and (d) different density ratio R_ρ. A solid line on each panel indicates the ratio for isotropic turbulence.

These approximations can be justified by observations (Lueck, 1987) and numeri-

cal simulation (Shen, 1995) both showing nearly isotropic thermal buoyancy field in the turbulent regime. This justification may not be consistent for the early stage of the flow when salt sheets or salt fingers are active. The geometry of salt fingers and salt sheets led theoretical models to utilize the "tall fingers" (TF) approximation in an unbounded salt fingers and salt sheets (Kunze, 1987; Smyth and Kimura, 2007; Stern, 1975). Since salt fingers and salt sheets are tall and narrow, the TF approximation assumes that the vertical derivative is negligible relative to horizontal derivatives ($\langle\overline{\epsilon^z}\rangle = \langle\overline{\chi_T^z}\rangle = 0$).

Figures 4.11a and 4.11b show that $\langle\overline{\epsilon^z}\rangle$ gives a poor estimate of $\langle\overline{\epsilon}\rangle$ due to the influence of salt sheets. As the flow evolves, $\langle\overline{\epsilon^z}\rangle/\langle\overline{\epsilon}\rangle$ increases, but the ratio does not converge to unity. Instead, each of the ratio becomes quasi-steady, ranging between 0.3 and 0.5 for $\sigma_L t > 8$ (figure 4.11a and 4.11b). Figure 4.11c and 4.11c show that the value of $\langle\overline{\chi_T^z}\rangle/\langle\overline{\chi_T}\rangle$ becomes quasi-steady between 0.8 and 1.2. $\langle\overline{\chi_T}\rangle$ is more isotropic than $\langle\overline{\epsilon}\rangle$ in the quasi-steady limit.

In the presence of double-diffusive turbulence, $\langle\overline{\chi_T^z}\rangle$ is an appropriate approximation, but $\langle\overline{\epsilon^z}\rangle$ underestimates $\langle\overline{\epsilon}\rangle$ by a factor of 2 to 3.

4.6. Turbulent fluxes in sheared, double-diffusive turbulence

Of primary interest of oceanographic community is to understand the turbulent fluxes associated with double diffusive turbulence. Measurements of $\langle\overline{\epsilon}\rangle$ and $\langle\overline{\chi_T}\rangle$ allow the indirect estimates of turbulent fluxes via Γ:

$$\Gamma = \frac{\langle\overline{b_{,z}}\rangle\langle\overline{\chi_T}\rangle}{2\langle\overline{\epsilon}\rangle\left\langle\overline{b_{T,z}}^2\right\rangle}.$$

In turbulent mixing, the mechanical energy that goes into mixing can be expended in raising the mass of fluid and the dissipation by molecular viscosity. Γ approximates the fraction of the turbulent kinetic energy that is irreversibly converted to potential energy due to mixing. In shear-driven turbulence, Γ can be used to estimate the effective

diffusivity of heat and salt as $K_T = K_S = \Gamma \frac{\langle \overline{\epsilon} \rangle}{\langle B_{,z} \rangle}$ (Osborn, 1980).

The effective diffusivity of heat and salt are different in sheared, double-diffusive turbulence. Effective diffusivities of heat and saline buoyancy are defined via standard flux-gradient parameterization:

$$K_T = -\frac{\langle \overline{w' b'_T} \rangle}{\left\langle \overline{\frac{\partial b_T}{\partial z}} \right\rangle}; \quad K_S = -\frac{\langle \overline{w' b'_S} \rangle}{\left\langle \overline{\frac{\partial b_S}{\partial z}} \right\rangle}.$$

The turbulent heat, salt, and momentum fluxes can also be parameterized using nondimensional parameters such as heat-salt flux ratio and Schmidt number, defined as,

$$\gamma_s = -\frac{\langle \overline{w' b'_T} \rangle}{\langle \overline{w' b'_S} \rangle}, \quad Sc = \frac{K_U}{K_S},$$

where K_U is the effective diffusivity of momentum, $K_U = -\langle \overline{u'w'} \rangle / \left\langle \overline{\frac{\partial u}{\partial z}} \right\rangle$. The γ_s quantifies the thermal buoyancy flux relative to saline buoyancy flux. In the salt-fingering and salt sheets instabilities, unstable distribution of mean saline buoyancy drives salt and heat fluxes downward. This implies that thermal buoyancy flux is working against the gravity, $\overline{w' b'_T} < 0$. Schmidt number quantifies the relative importance of effective diffusivity of momentum to that of salt. We will quantify the Ri and R_ρ dependence of effective diffusivities.

4.6.1 Estimation of Γ

In the isotropic turbulence, Γ can take the form:

$$\Gamma^z = \frac{\langle \overline{b_{,z}} \rangle \langle \overline{\chi_T^z} \rangle}{2 \langle \overline{\epsilon^z} \rangle \left\langle \overline{b_{T,z}}^2 \right\rangle}.$$

In shear-driven turbulence, measurements indicate $\Gamma^z \approx 0.2$ in the ocean (Moum, 1996; Oakey, 1982; Osborn, 1980). These measurements are accurate for $Re_b > 200$ (Gargett et al., 1984). In salt-fingering system, measurements suggest that Γ can take higher values: $0.4 < \Gamma^z < 2$ (Inoue et al., 2008; St. Laurent and Schmitt, 1999). At the

steady state, balances of turbulent kinetic energy and scalar variance imply

$$\Gamma = \frac{R_\rho - 1}{R_\rho} \frac{\gamma_s}{1 - \gamma_s}$$

in the absence of shear (Hamilton et al., 1989; McDougall and Ruddick, 1992). Γ for the fastest growing salt-fingering is a function of R_ρ by substituting $\gamma_s = (R_\rho)^{1/2}[(R_\rho)^{1/2} - (R_\rho - 1)^{1/2}]$ (Kunze, 1987; Stern, 1975).

In the presence of shear, Γ becomes

$$\Gamma = \frac{R_f}{R_f - 1} \frac{R_\rho - 1}{R_\rho} \frac{\gamma_s}{1 - \gamma_s},$$

where $R_f = -\langle \overline{w'b'} \rangle / \langle \overline{u'w'} \overline{\frac{\partial u}{\partial z}} \rangle$ is the flux Richardson number (St. Laurent and Schmitt, 1999). Smyth and Kimura (2007) showed that Γ for the fastest growing salt sheet becomes

$$\Gamma = \frac{R_\rho - 1}{R_\rho} \frac{PrRi}{PrRi + 1}. \tag{4.15}$$

Γ fluctuates below 0.6 in all cases, as illustrated by the examples in figure 4.12. Salt sheets quickly adjust $\Gamma \sim 0.5 - 0.6$ to its linear values, and maintain this value during the linear regime. The Γ decays slowly as the flow becomes unstable to secondary instability ($\sigma_L t \sim 3$) and becomes quasi-steady between 0.3 and 0.4 in the turbulent regime.

Figure 4.12b shows that Γ^z is generally larger than Γ. In the cases of $Ri > 6$, Γ_z can be 30 times larger than Γ during the linear regime ($0 < \sigma_L t < 3$). A local peak of Γ^z/Γ is formed during the secondary instability ($\sigma_L t \sim 5$). As the flow becomes turbulent, the ratio decreases and approaches a quasi-steady value ~ 2, i.e., Γ_z overestimates Γ by a factor of 2 in the turbulent regime. Since both Γ and Γ^z become quasi-steady after $\sigma_L t > 8$, each of Γ and Γ^z is averaged over $\sigma_L t > 8$ to quantify Ri and R_ρ dependence in turbulent regime.

Figure 4.13 shows that Γ^z is in the range of observed Γ^z. Both observed Γ^z and Γ^z increase with increasing Ri. Similarly, Γ increases with increasing Ri; however, the values of Γ are below Γ^z for all Ri. Γ^z overestimates Γ at least by a factor of 2. Figure 4.14

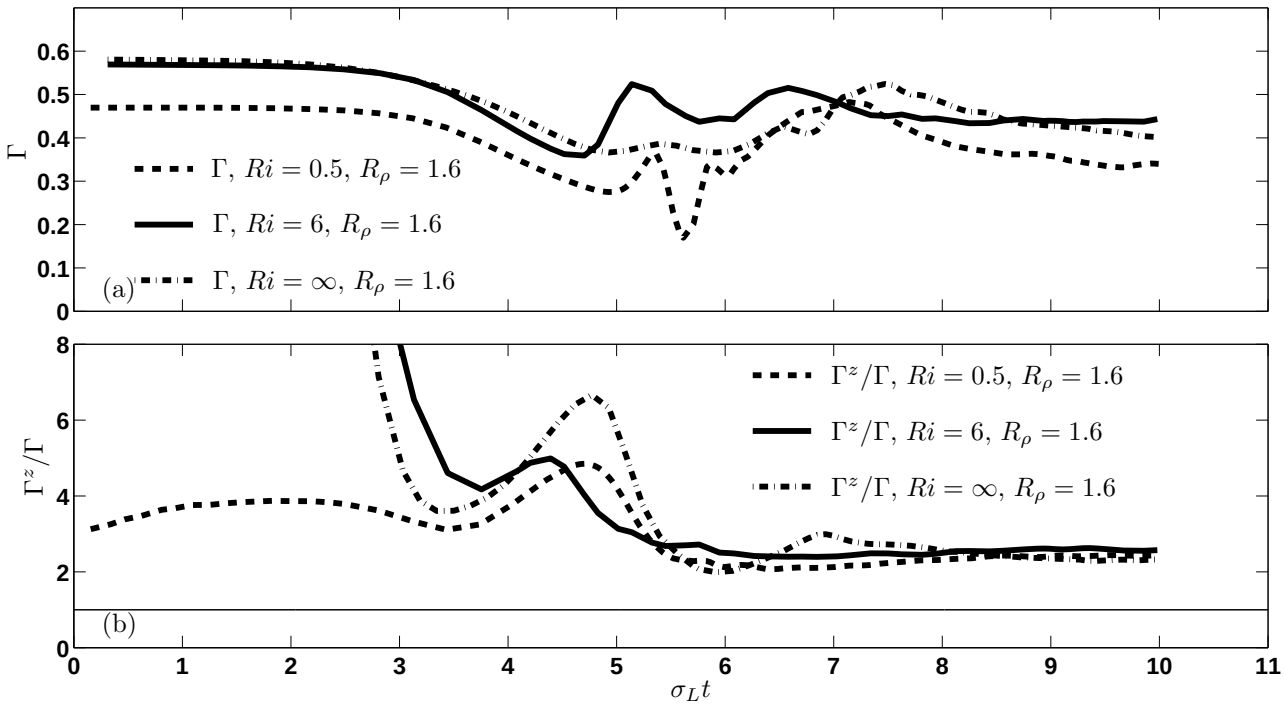

FIGURE 4.12: Evolution of (a) Γ and (b) Γ_z normalized by its true value Γ for different Ri. These ratios are unity for isotropic turbulence indicated by a thin solid line.

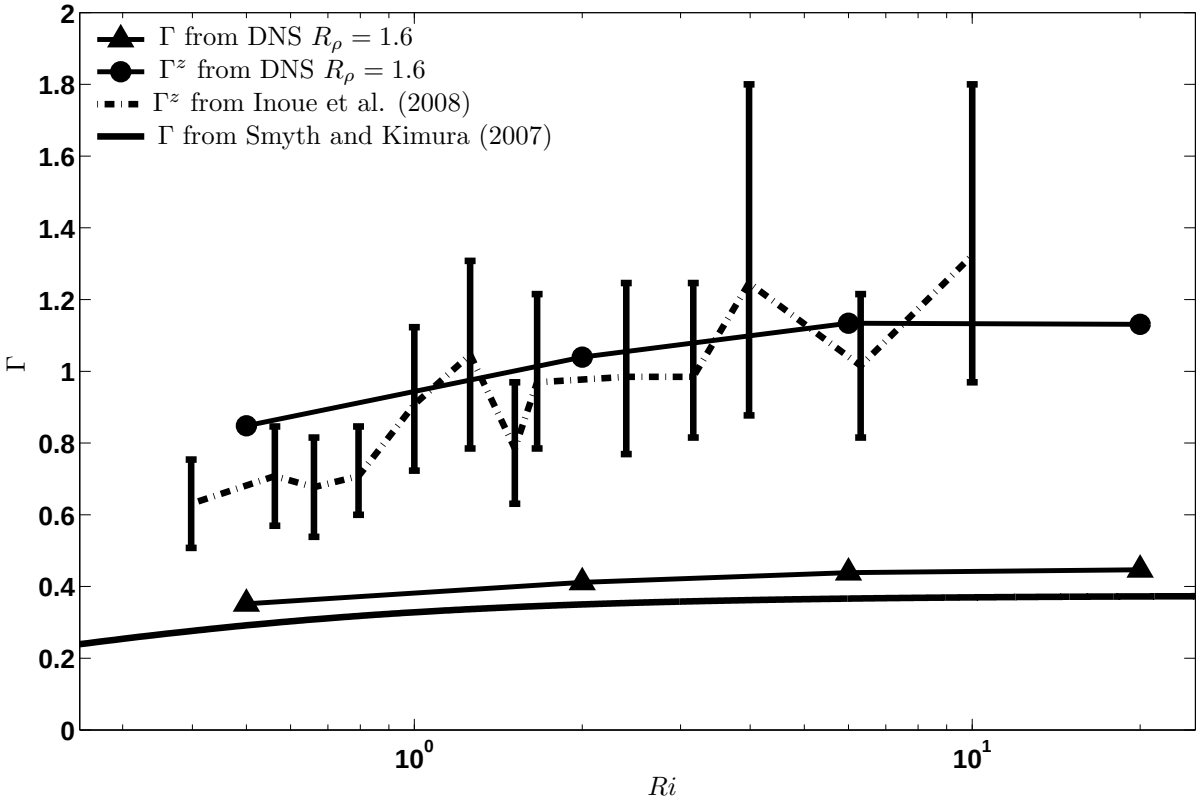

FIGURE 4.13: Γ and Γ^z for different Ri compared to observations from Inoue et al (2008). Vertical bars denote 95% confidence limits (Inoue et al., 2008). Mean R_ρ is nearly constant around 1.65 in Inoue et al. (2008). Smyth and Kimura (2007) calcualted Γ using linear stability analysis. Here we showed their Γ for $R_\rho = 1.6$.

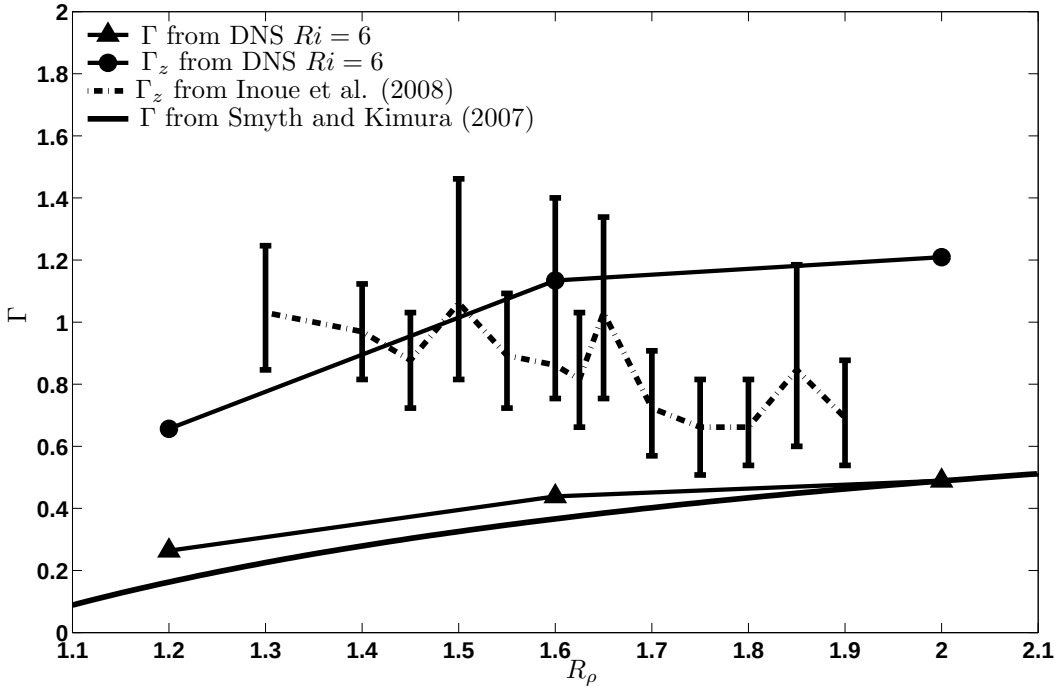

FIGURE 4.14: Γ and Γ^z for different R_ρ compared to observations from Inoue et al. (2008). Vertical bars denote 95% confidence limits (Inoue et al., 2008). Mean Ri ranges between 3 and 7 for Inoue et al. (2008). Smyth and Kimura (2007) calcualted Γ using linear stability analysis. Here we plotted their Γ for $R_\rho = 1.6$.

shows that R_ρ dependence of the observed Γ^z and the DNS result have different trends. Observed Γ^z decreases with increasing R_ρ, while both Γ^z and Γ from DNS increase with increasing R_ρ. Γ^z from DNS is within the error bound of observed Γ^z for $1.4 < R_\rho < 1.9$. Γ^z overestimates Γ by a factor of 2 to 3 in the turbulent regime.

Both figures 4.13 and 4.14 show that the approximation based on the linear result by Smyth and Kimura (2007) matches Γ from DNS; however, this result needs to be interpreted with caution. Their result (4.15) is an approximation for Γ in the linear regime. It is fallacious to conclude that this approximation predicts Γ in the turbulent state.

The Γ^z has been used to verify $k - \epsilon$ model of double-diffusive turbulence against observations of St. Laurent and Schmitt (1999) (Canuto et al., 2008). Canuto et al. (2008) derived Γ^z from a second-order closure model for double-diffusive turbulence and predicted observed Γ^z by St. Laurent and Schmitt (1999) well. In their closure model, the ratios of correlation time scales to the dissipation time scales depends on Ri and R_ρ where traditional models assumed these ratios to be constants (e.g. Mellor and Yamada, 1982). Our result shows that Γ^z overestimates Γ because of the isotropy. This will impact the estimates of correlation time scales in the $k - \epsilon$ model of Canuto et al. (2008).

4.6.2 Effective diffusivity

Effective diffusivity is widely used in large scale models in order to represent small-scale physics (Bryan, 1987; Gargett and Holloway, 1992; Walsh and Ruddick, 1995). Gargett and Holloway (1992) found that the steady state model solutions of low-resolution general circulation models (GCMs) were sensitive to the ratio of K_T to K_S. They used a ratio of K_S/K_T between 0.5 and 2. Merryfield et al. (1999) used R_ρ dependent K_T and K_S to examine the role of double-diffusive mixing in a global ocean model. They found that the regional circulation is significantly influenced by double-diffusive mixing; however, a large-scale circulation is slightly modified. Zhang et al. (1999) also parame-

terized K_T and K_S as a function of R_ρ and found that double diffusion was stronger in the western boundary current region than the interior, implying a close relation between vertical shear and the intensity of double diffusion. Effective diffusivity from DNS can be used in large-scale models to improve the representations of small-scale physics.

Figures 4.15 shows that K_S increases exponentially until the disruption of the primary instability ($\sigma_L t \approx 5$). After a period of slow decline, K_S approaches a quasi-steady state at $\sigma_L t \approx 8$. The reduction of K_S by the presence of the shear is evident in the figures 4.15a. In the case of $Ri = 0.5$, K_S are smaller by a factor of 4 relative to $Ri = \infty$ case. Figures 4.15b show that the K_S increases with decreasing R_ρ. This R_ρ dependence had been reported by the previous DNS of two-dimensional salt-fingering (Merryfield and Grinder, 2000; Stern et al., 2001).

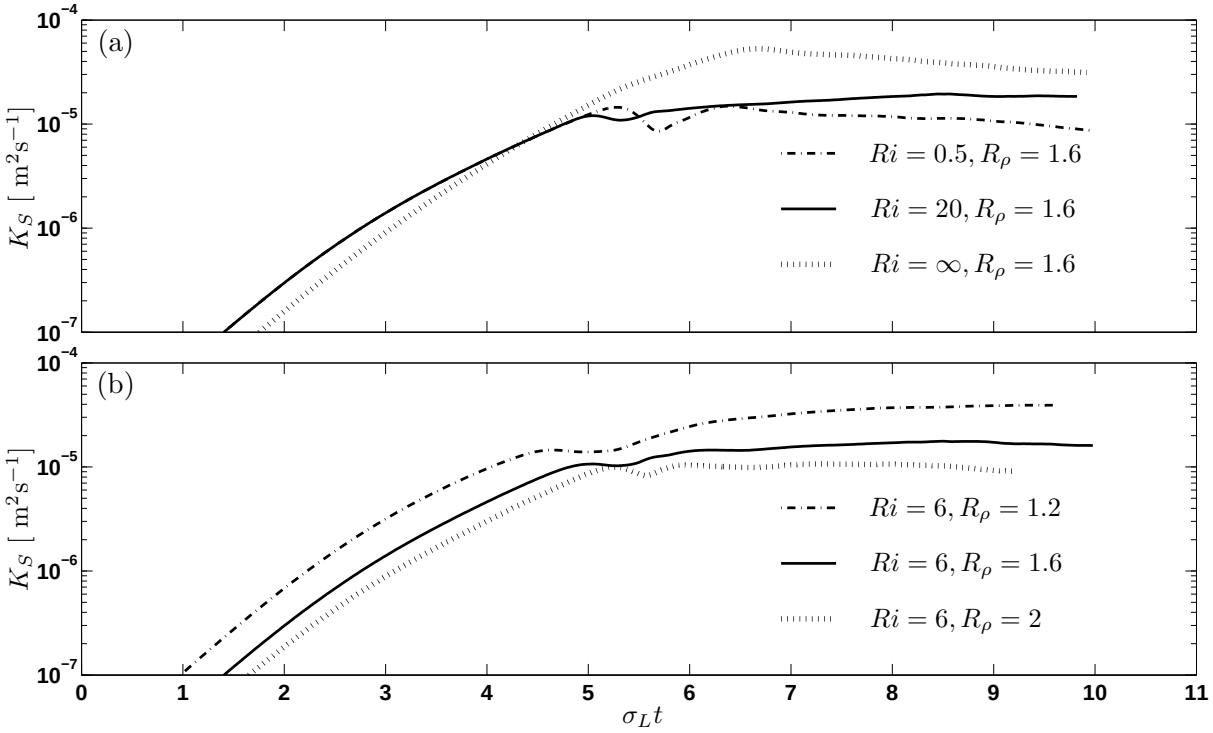

FIGURE 4.15: Effective diffusivity of salt, K_S with respect to scaled time for (a) different Ri with keeping $R_\rho = 1.6$ and (b) different R_ρ with keeping $Ri = 6$.

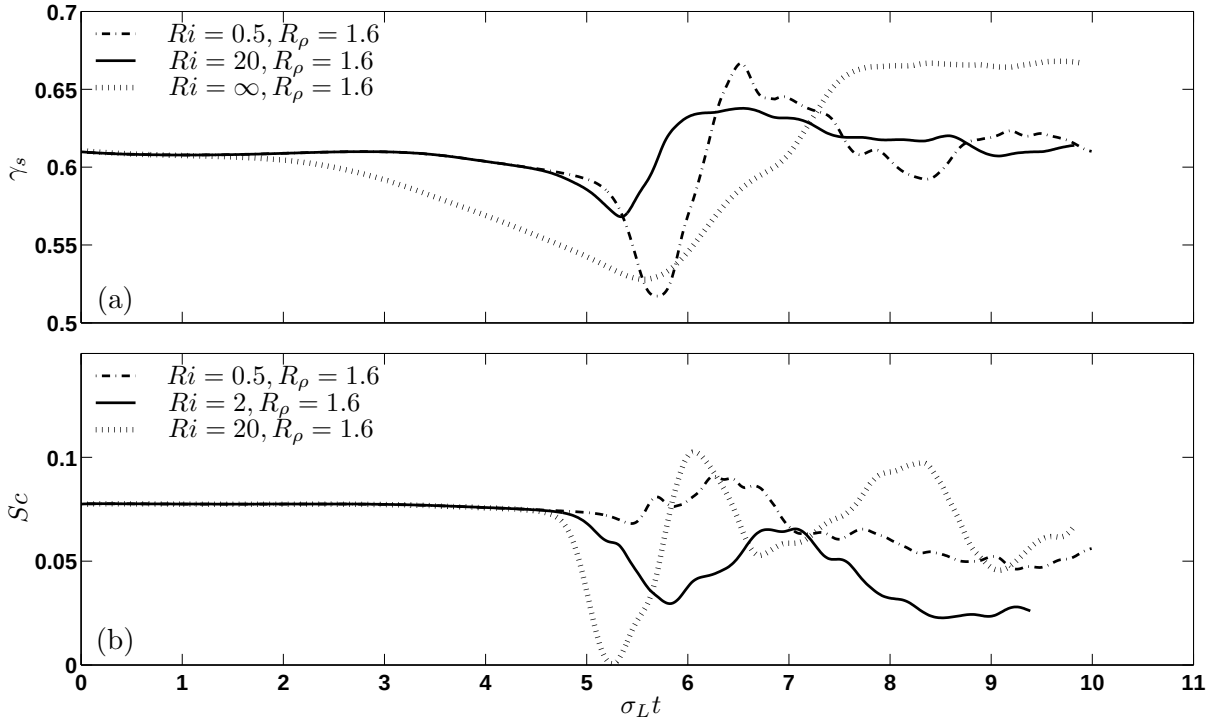

FIGURE 4.16: Evolution of (a) flux ratio, γ_s, and Schmidt number, Sc, with respect to scaled time for different Ri with keeping $R_\rho = 1.6$.

Figure 4.16a shows that γ_s evolves with the constant value of ≈ 0.6, which agrees with its linear value. After a slowly decaying period, γ_s reaches quasi-steady limit, which is larger than its linear value in $Ri = \infty$ case. In contrast, γ_s fluctuates within 3% of its linear value in sheared cases. Approximations made in the linear regime still holds well in the finite Ri cases, where it does not for $Ri = \infty$ case.

Ruddick (1985) suggested that individual salt sheets rapidly lose their momentum via lateral diffusion and offered a dimensional argument, which suggested $Sc \leq 1$. A laboratory experiment to confirm this hypothesis is a challenge, since it is difficult to accurately measure interfacial stress changes associated with convective velocity (Ruddick et al., 1989). Linear stability analysis of salt sheet (Smyth and Kimura, 2007), and subsequent DNS simulation (Kimura and Smyth, 2007) for a single initial case suggested $Sc \leq 1$. Figure 4.16b shows that $Sc \leq 1$ holds in Ri ranging from 0.5 to 20. Effective

diffusivity of the momentum is an order of magnitude smaller than that of salt. We have confirmed that salt sheets are inefficient in transporting momentum.

The parametrizations of these diffusivities are essential in modeling large-scale flows that double- diffusive turbulence controls the small-scale fluxes of heat and salt, such as thermohaline interleaving. Walsh and Ruddick (2000) employed a parameterization of K_S for pure salt-fingering: $K_S = K_{S0} R_\rho^{-n}$. Smyth (2007) fitted this simple model to DNS results from Stern et al. (2001) and obtained $n = 2$ and $K_{S0} = 10^{-4}$. Here, we add dependence on Ri:

$$\begin{aligned} K_T(R_\rho, Ri) &= K_{T0} R_\rho^{-n_T} Ri^{m_T}; \\ K_S(R_\rho, Ri) &= K_{S0} R_\rho^{-n_S} Ri^{m_S}. \end{aligned}$$

We computed the least square fit of the above equations to the averaged K_T and K_S over $\sigma_L t > 8$. The resulting empirical models are

$$\begin{aligned} K_T(R_\rho, Ri) &= 3.07 \times 10^{-5} R_\rho^{-3.99} Ri^{0.172} \quad \text{and} \\ K_S(R_\rho, Ri) &= 4.38 \times 10^{-5} R_\rho^{-2.68} Ri^{0.17}. \end{aligned}$$

Figure 4.17a and 4.17c show that both K_T and K_S increase with increasing Ri. In 2D unsheared, double-diffusive turbulence, Stern et al. (2001) showed that decrease in τ from 0.04 to 0.01 increased the heat flux by 15%. In 3D sheared, double-diffusive turbulence, Kimura and Smyth (2007) found that the decrease in τ from 0.04 to 0.01 increases the K_T and K_S by a factor of 2. The effective diffusivities of heat and salt for the oceanic water may be 2 times larger than our DNS results presented here.

Figure 4.17b and 4.17d show the both K_T and K_S decrease with increasing R_ρ. The R_ρ trend from our result corresponds well with DNS results from Merryfield and Grinder (2000), despite the difference in Ri, τ, and dimensions. Estimates of Stern et al. (2001) are twice as large; this could be due the presence of the shear and the difference in τ.

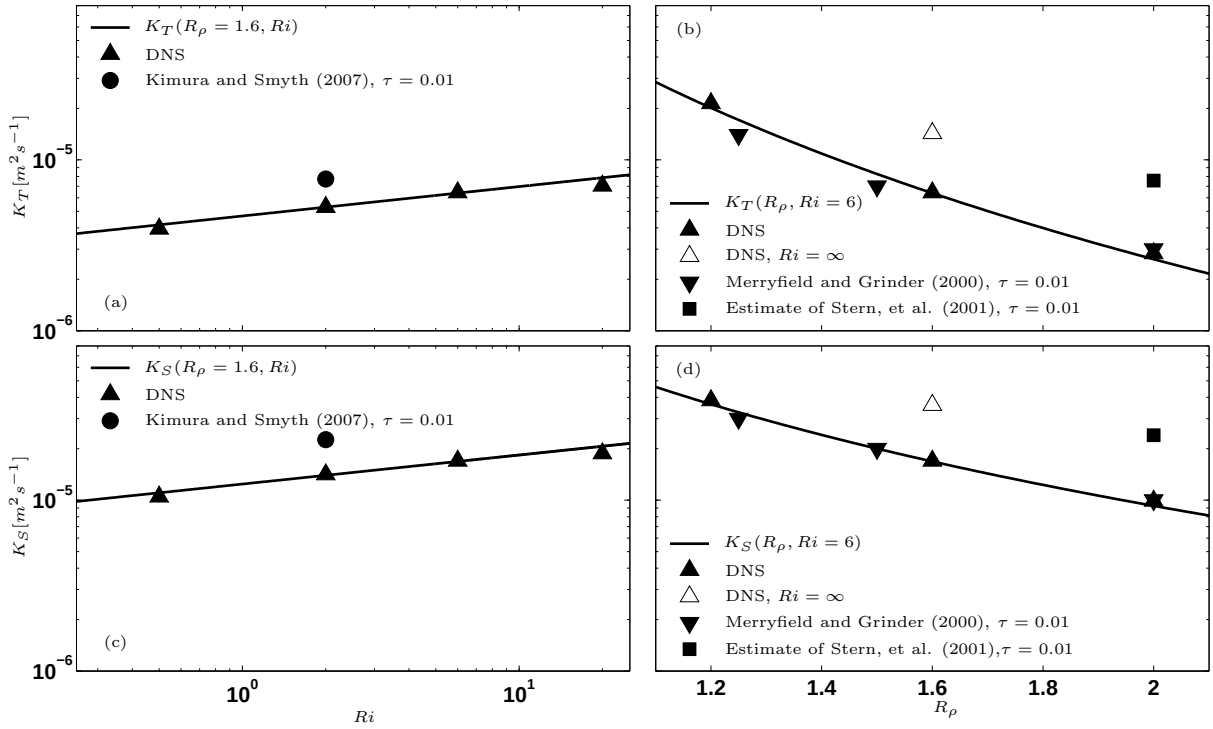

FIGURE 4.17: (a) Effective diffusivity of heat with respect to Ri. (b) Effective diffusivity of heat with respect to R_ρ. (c) Effective diffusivity of salt with respect to Ri. (d) Effective diffusivity of salt with respect to R_ρ. Circles in (a) and (b) indicate the effective diffusivity of heat and salt of three-dimensional DNS from Kimura and Smyth (2009) with $\tau = 0.01$, where DNS results presented here is $\tau = 0.04$. Downward triangles in (b) and (d) indicate the two-dimensional DNS results of Merryfield and Grinder (2000) with $Ri = \infty$ and $\tau = 0.01$. Squares in (b) and (d) indicate the estimate of three-dimensional effective diffusivities by Stern, et al. (2001). Stern et al. estimated the effective diffusivities of heat and salt for $Ri = \infty$ case by calculating the ratio of 2D to 3D fluxes using accessible values of τ, then multiply the ratio onto the directly computed fluxes for 2D with $\tau = 0.01$.

To compare results to observations, we estimate effective diffusivities by the Osborn and Cox (1972) diffusivity model in the next section.

4.6.3 Estimation of effective diffusivity

In interpretations of observational data, the Osborn and Cox (1972) diffusivity model in conjunction with the isotropy assumption is used as

$$K_T^{\chi^z} = \frac{\langle \overline{\chi_T^z} \rangle}{2\left\langle \left(\overline{\frac{\partial b_T}{\partial z}} \right)^2 \right\rangle}; \quad K_S^{\chi^z} = \frac{\langle \overline{\chi_S^z} \rangle}{2\left\langle \left(\overline{\frac{\partial b_S}{\partial z}} \right)^2 \right\rangle},$$

where $\langle\overline{\chi_S^z}\rangle = 6\kappa_S \left\langle \overline{\left(\frac{\partial b_S'}{\partial z}\right)^2} \right\rangle$. These estimates are exact for stationary, homogeneous turbulence.

The Osborn-Cox model captures the R_ρ dependence of K_T and K_S (figure 4.18a and 4.18b). Both $K_T^{\chi^z}$ and $K_S^{\chi^z}$ decrease with increasing R_ρ consistent with trend of its true values and observations by St. Laurent and Schmitt (1999). However, the magnitude of $K_T^{\chi^z}$ and $K_S^{\chi^z}$ are different from K_T and K_S. Both K_T and K_S are more diffusive than $K_T^{\chi^z}$ and $K_S^{\chi^z}$ for the range of R_ρ. The Osborn-Cox model diffusivity model (1972) can underestimate K_T and K_S up to a factor of 3 in double-diffusive turbulence.

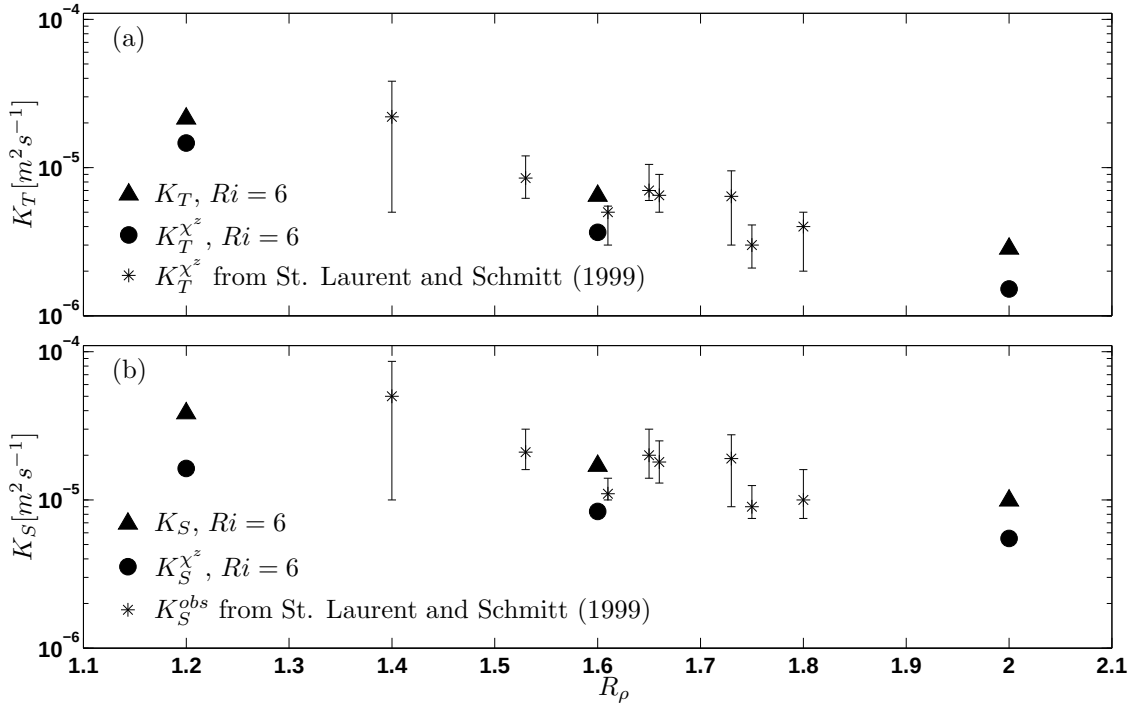

FIGURE 4.18: (a) Comparisons of effective diffusivites of heat and its estimates from DNS and observation by St. Laurent and Schmitt (1999) with respect to R_ρ. (b) Comparisons of effective diffusivites of salt and its estimates from DNS and observation by St. Laurent and Schmitt (1999) with respect to R_ρ. Because of small scale structures pertained in salinity, estimation of χ_S from observations is difficult. Thus, K_S is estimated as $K_S^{obs} = \frac{R_\rho}{\gamma_s} K_T^{\chi^z}$ in the interpretations of observations.

4.7. Conclusions

We have simulated sheared, double-diffusive turbulence using DNS with the following assumptions:

1. the ratio of molecular diffusivity of salt to heat is 4 times larger than the real ocean;
2. the layer thickness of the transitional layer is at least 3 times smaller than observed thickness of thermohaline staircases;
3. the equation of state is linear.

Our main findings are follows:

1. Velocity gradients are not isotropic, but the scalar gradients are nearly isotropic. The approximations of $\overline{\epsilon}$ based on vertical shears, which are often used in the interpretations of microstructure data, underestimate its value by a factor of 2 to 3. This suggests that the rate of dissipation by sheared, double-diffusive turbulence can be 2 to 3 times larger than previous measurements.
2. The isotropy assumption can lead to overestimation of Γ by a factor of 2 to 3. This will impact the estimates of correlation time scales in the $k-\epsilon$ model of double-diffusive turbulence (e.g. Canuto et al., 2008).
3. Decrease in Ri or an increase in R_ρ reduces the effective diffusivities of heat and salt. Our empirical models give: $K_T(R_\rho, Ri) = 3.07\times10^{-5} R_\rho^{-3.99} Ri^{0.172}$ and $K_S(R_\rho, Ri) = 4.38\times10^{-5} R_\rho^{-2.68} Ri^{0.17}$. Kimura and Smyth (2007) showed that decrease in τ from 0.04 to 0.01 increase K_T and K_S by a factor of 2; however, the effects of the layer thickness is currently not known and left for the future investigation.
4. Effective diffusivities estimated by the Osborn-Cox diffusivity model (1972) produced consistent R_ρ dependence; however, the magnitude of diffusivities can be up

to 3 times smaller than its true diffusivities.

Acknowledgments. This project has benefited from discussions with Timour Radko and Bill Merryfield. Computer time was provided by the National Center for Atmospheric Research (NCAR). The graphics are produced using VAPOR with help from VisLab at NCAR. The work was supported by the National Science Foundation under Grant No. 0453140.

5. CONCLUSIONS

The goal of this dissertation has been to capture instability and turbulence that occurs in a single transition layer of a thermohaline staircases using 3D DNS. The transition layer, separating two homogeneous layers above and below, is modeled as a double-diffusive shear layer of hyperbolic tangent form.

Simulations shows that the primary instability is salt sheets, planar regions of rising and sinking fluid, aligned parallel to the direction of the horizontal current, in accordance with Linden (1974) and Smyth and Kimura (2007). When the salt sheet reaches finite-amplitude, the tip mode appeared at the edges of salt sheets introducing quasi-periodic dependence on x. This mode is an oscillatory instability and its turbulent kinetic energy is mainly driven by buoyancy production. The dominance of buoyancy production may explain why parameterizations based on the disruption of salt fingers by shear-driven instabilities have had difficulty predicting observed fluxes (e.g. Inoue et al., 2008). The tip mode disrupts the salt sheets and lead the flow into double-diffusive turbulence.

Dependence on strength of shear and salt-fingering of double-diffusive turbulence is investigated by varying initial Ri and R_ρ. Isotropy hypothesis is tested on velocity and scalar gradient fields. Velocity gradient fields are not isotropic, while the scalar gradient fields become nearly isotropic. Because the velocity gradient fields are not isotropic, approximation of the turbulent kinetic energy dissipation rate based on vertical shears, which are often used in the interpretations of microstructure data, underestimates its true value by a factor of 2 to 3. This will impact estimates of correlation time scales in the $k-\epsilon$ model of double-diffusive turbulence (e.g. Canuto et al., 2008) because such estimates are accomplished by taking microstructure data as the ground truth.

The Ri and R_ρ dependence of the effective diffusivities are investigated. The increase in mechanical energy reduces the thermal and saline effective diffusivities in double-

diffusive turbulence in dramatic contrast to the effect of mechanically-driven turbulence. The empirical models give: $K_T(R_\rho, Ri) = 3.07 \times 10^{-5} R_\rho^{-3.99} Ri^{0.172}$ and $K_S(R_\rho, Ri) = 4.38 \times 10^{-5} R_\rho^{-2.68} Ri^{0.17}$.

The transfer of momentum is much less efficient than is often assumed, i.e., the Schmidt number is much less than order one. This confirms scaling analysis of Ruddick (1985) and Ruddick et al. (1989), suggesting that transfer of momentum by salt sheet is negligible relative to transport of heat and salt. The result raises a question on a layer thickness of thermohaline interleaving layers; the Schmidt number is often chosen to be greater than one in order to obtain interleaving layers of realistic thickness (Walsh and Ruddick, 1995, 2000).

Simulations for quantifying the Ri and R_ρ dependence are accomplished by

- artificially raising the ratio of molecular diffusivity of salt to heat;
- reducing the layer thickness of the transition layer.

Both compromises are necessary to meet the available computational resource. The ratio of molecular diffusivity of salt to heat is 4 times larger than the real ocean, and the layer thickness of the transition layer is at least 3 times smaller than observed thickness. It is shown that the increase in the ratio reduces the effective diffusivities by a factor of 2; however, the effects of reducing the thickness of transition layer is unknown and left for the future investigation.

BIBLIOGRAPHY

Bryan, F., 1987: On the parameter sensitivity of primitive equation ocean general circulation. *J. Phys. Oceanogr.*, **17**, 970–985.

Canuto, V., Y. Cheng, and A. Howard, 2008: A new model for double diffusion + turbulence using a reynolds stress model. *Geophys. Res. Lett.*, **35**, L02 613.

D.Mueller, R., W. Smyth, and . B.R. Ruddick, 2007: Shear and convective turbulence in a model of thermohaline intrusions. *J. Phys. Oceanogr.*, **37**, 2534–2549.

Fleury, M. and R. Lueck, 1991: Fluxes across a thermohaline interface. *Deep-Sea Research*, **38(7)**, 745–769.

Gargett, A., T. Osborn, and P. Nasmyth, 1984: Local isotropy and the decay of turbulence in a stratified fluid. *J. Fluid Mech.*, **144**, 231–280.

Gargett, A. E. and G. Holloway, 1992: Sensitivity of the gfdl ocean model to different diffusivities of heat and salt. *J. Phys. Oceanogr.*, **22**, 1158–1177.

Gargett, A. E., W. Merryfield, and G. Holloway, 2003: Direct numerical simulation of differential scalar diffusion in three-dimensional stratified turbulence. *jpo*, **33**, 1758–1782.

Gregg, M. and T. Sanford, 1987: Shear and turbulence in thermohaline staircases. *Deep Sea Res.*, **34**, 1689–1696.

Hamilton, J., M. Lewis, and B. Ruddick, 1989: Vertical fluxes of nitrate associated with salt fingers in the world's oceans. *J. Geophys. Res.*, **94**, 2137–2145.

Hazel, P., 1972: Numerical studies of the stability of inviscid parallel shear flows. *J. Fluid Mech.*, **51**, 39–62.

Holyer, J., 1984: The stability of long steady, two dimensional salt fingers. *J. Fluid Mech.*, **147**, 169–185.

Howard, L., 1961: Note on a paper of john w. miles. j. *J. Fluid Mech.*, **10**, 509–512.

Inoue, R., E. Kunze, L. S. Laurent, R. Schmitt, and J. Toole, 2008: Evaluating salt-fingering theories. *J. Mar. Res.*, **66**, 413–440.

Itsweire, E., J. Kosefe, D. Briggs, and J. Ferziger, 1993: Turbulence in stratified shear flows: implications for interpreting shear-induced mixing in the ocean. *J. Phys. Oceanogr.*, **23**, 1508–1522.

Kimura, S. and W. Smyth, 2007: Direct numerical simulation of salt sheets and turbulence in a double-diffusive shear layer. *Geophys. Res. Lett.*, **34**, L21 610.

Kolmogorov, A., 1941: The local structure of turbulence in incompressible viscous fluid for very large reynolds number. *Dokl. Akad. Nauk SSSR*, **30 (4)**, 301–305.

Kunze, E., 1987: Limits on growing finite-length salt fingers: A richardson number constraint. *J Mar. Res.*, **45**, 533–556.

Kunze, E., 1990: The evolution of salt fingers in inertial wave shear. *J Mar. Res.*, **48**, 471–504.

Kunze, E., 1994: A proposed flux constraint for salt fingers in shear. *J Mar. Res.*, **52**, 999–1016.

Kunze, E., 2003: A review of oceanic salt fingering theory. *Prog. Oceanogr.*, **56**, 399–417.

Kunze, E., A. Williams, and R. Schmitt, 1987: Optical microstructure in the thermohaline staircase east of barbados. *Deep Sea Res.*, **34**, 1697–1704.

Lambert, R. B. and W. Sturges, 1977: A thermohaline staircase and vertical mixing in the thermocline. *Deep-Sea Res.*, **24**, 211–222.

Linden, P., 1974: Salt fingers in a steady shear flow. *Geophys. Fluid Dyn.*, **6**, 1–27.

Lueck, R., 1987: Microstructure measurements in a thermohaline staircase. *Deep-Sea Res.*, **34**, 1677–1688.

McDougall, T. J. and B. R. Ruddick, 1992: The use of ocean microstructure to quantify both turbulent mixing and salt fingering. *Deep-Sea Res.*, **39**, 1931–1952.

McDougall, T. J. and J. R. Taylor, 1984: Flux measurements across a finger interface at low values of the stability ratio. *J. Mar. Res.*, **42**, 1–14.

Mellor, G. L. and T. Yamada, 1982: Development of a turbulence closure model of geophysical fluid problems. *Rev. Geophys.*, **20**, 851–875.

Merryfield, W., 1999: Origin of thermohaline staricases. *J. Phys. Oceanogr.*, **30**, 1046–1068.

Merryfield, W. J. and M. Grinder, 2000: Salt fingering fluxes from numerical simulations. *unpublished*.

Merryfield, W. J., G. Holloway, and A. E. Gargett, 1999: A global ocean model with double-diffusive mixing. *J. Phys. Oceanogr.*, **29**, 1124–1142.

Miles, J., 1961: On the stability of heterogeneous shear ows. *J. Fluid Mech.*, **10**, 496–508.

Moum, J. N., 1996: Efficiency of mixing in the main thermocline. *J. Geophys. Res.*, **11 (C5)**, 12 057–12 069.

Oakey, N. S., 1982: Determination of the rate of dissipation of turbulent energy from simultaneous temperature and velocity shear microstructure measurements. *J. Phys. Oceanogr.*, **12**, 256–271.

Osborn, T. R., 1980: Estimates of the local rate of vertical diffusion from dissipation measurements. *J. Phys. Oceanogr.*, **10**, 83–89.

Osborn, T. R. and C. S. Cox, 1972: Oceanic fine structure. *Geophys. Fluid Dyn.*, **3**, 321–345.

Ozmidov, R. V., 1965: On the turbulent exchange in a stably stratified ocean. *Izv. Atmos. Oceanic Phys.*, **8**, 853–860.

Piacsek, S. and J. Toomre, 1980: Nonlinear evolution and structure of salt fingers. *In Marine Turbulence, ed. J.C.J. Nihoul, Elsevier Oceanography*, **(28)**, 193–219.

Proctor, M. R. E. and J. Y. Holyer, 1986: Planform selection in salt fingers. *J. Fluid Mech.*, **168 (-1)**, 241–253.

Radko, T., 2003: A mechanism for layer formation in a double diffusive fluid. *J. Fluid Mech.*, **497**, 365–380.

Ruddick, B. R., 1985: Momentum transport in thermohaline staircases. *J. Geopys. Res.*, **90**, 895–902.

Ruddick, B. R., R. W. Griffiths, and G. Symonds, 1989: Frictional stress at a sheared double-diffusive interface. *J. Geopys. Res.*, **94**, 18 161–18 173.

Schmitt, R. W., 1994a: Double diffusion in oceanography. *Ann. Rev Fluid Mech.*, **26**, 255–285.

Schmitt, R. W., 1994b: Triangular and asymmetric salt fingers. *J. Phys. Oceanogr*, **24**, 855–860.

Schmitt, R. W., 2003: Observational and laboratory insights into salt finger convection. *Prog. Oceanogr.*, **56**, 419–433.

Schmitt, R. W., H. Perkins, J. Boyd, and M. Stalcup, 1987: C-salt: An investigation of the thermohaline staircase in the western tropical north atlantic. *Deep-Sea Res.*, **34**, 1655–1665.

Shen, C., 1989: The evolution of the double-diffusive instability: Salt fingers. *Physics of Fluids*, **A1(5)**, 829–844.

Shen, C., 1995: Equilibrium salt-fingering convection. *Physics of Fluids*, **7(4)**, 706–717.

Smyth, W. D., 2007: Instabilities of a baroclinic, double diffusive frontal zone. *J. Phys. Oceanogr.*, **38 ((4))**, 840–861.

Smyth, W. D. and S. Kimura, 2007: Instability and diapycnal momentum transport in a double-diffusive stratified shear layer. *J. Phys. Oceanogr.*, **37**, 1551–1565.

Smyth, W. D. and J. N. Moum, 2000: Anisotropy of turbulence in stably stratified mixing layers. *Phys. Fluids*, **12**, 1327–1342.

Smyth, W. D., J. Nash, and J. Moum, 2005: Differential diffusion in breaking Kelvin-Helmholtz billows. *J. Phys. Oceanogr.*, **35**, 1044–1022.

Smyth, W. D. and B. Ruddick, 2010: Effects of ambient turbulence on interleaving at a baroclinic front. *J. Phys. Oceanogr.*, 685–712.

St. Laurent, L. and R. Schmitt, 1999: The contribution of salt fingers to vertical mixing in the north atlantic tracer-release experiment. *J. Phys. Oceanogr.*, **29**, 1404–1424.

Stern, M., 1960: The 'salt fountain' and thermohaline convection. *Tellus*, **12**, 172–175.

Stern, M., 1969: Collective instability of salt fingers. *J. Fluid Mech.*, **35**, 209–218.

Stern, M., 1975: *Ocean Circulation*. Physics. Academic Press, 246 pp.

Stern, M., T. Radko, and J. Simeonov, 2001: Salt fingers in an unbounded thermocline. *J. Mar. Res.*, **59**, 355–390.

Stern, M. and J. Simeonov, 2005: The secondary instability of salt fingers. *J. Fluid Mech.*, **533**, 361–380.

Tait, R. I. and M. R. Howe, 1968: Some observations of thermohaline stratification in the deep ocean. *Deep-Sea Res.*, **15**, 275–280.

Taylor, G. I., 1935: Statistical theory of turbulence. ii. *Proceedings of the Royal Society of London. Series A, Mathematical and Physical Sciences*, **151**, No. 873, 444–454.

Taylor, J. R., 1992: Anisotropy of salt fingers. *J. Phys. Oceanogr.*, **23**, 554–565.

Toole, J. and D. Georgi, 1981: On the dynamics of double diffusively driven intrusions. *Prog. Oceanogr.*, **10**, 123–145.

Walsh, D. and B. Ruddick, 1995: Double diffusive interleaving: the effect of nonconstant diffusivities. *J. Phys. Oceanogr.*, **25**, 348–358.

Walsh, D. and B. Ruddick, 2000: Double-diffusive interleaving in the presence of turbulencethe effect of a nonconstant flux ratio. *J. Phys. Oceanogr.*, **30**, 2231–2245.

Williams, A., 1974: Salt fingers observed in the mediterranean outflow. *Science*, **185**, 941–943.

Winters, K., J. MacKinnon, and B. Mills, 2004: A spectral model for process studies of rotating, density-stratifed flows. *J. Atmos. Oceanic Technol.*, **21**, (1)69–94.

Yoshida, J. and H. Nagashima, 2003: Numerical experiments on salt-finger convection. *Prog. Oceanogr.*, **56**, 435–459.

Zhang, J., R. Schmitt, and R. Huang, 1999: Sensitivity of the gfdl modular ocean model to parameterization of double-diffusive processes. *J. Phys. Oceanogr*, **28**, 589–605.